

Dupe N70-25491



GE-SSO-70SD4225
MARCH 13, 1970

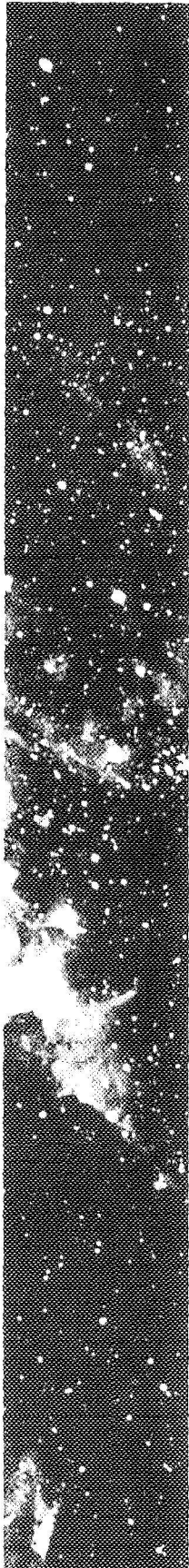
CASE FILE COPY

QUARTERLY REPORT NO. 4 ROLLUP SUBSOLAR ARRAY

Prepared for: Jet Propulsion Laboratory

Prepared Under: Contract 952314

FACILITY FORM 802	N70-25491 (ACCESSION NUMBER)	_____ (THRU)
	_____ (PAGES)	_____ (CODE)
	_____ (NASA CR OR TMX OR AD NUMBER)	_____ (CATEGORY)



DOCUMENT NO. 70SD4225
MARCH 13, 1970

ROLLUP SUBSOLAR ARRAY
QUARTERLY TECHNICAL REPORT NO.4
1 DECEMBER 1969 TO 28 FEBRUARY 1970

PREPARED FOR:
JET PROPULSION LABORATORY
CALIFORNIA INSTITUTE OF TECHNOLOGY
PASADENA, CALIFORNIA

PREPARED UNDER: CONTRACT 952314
CONTRACTING OFFICER: E.C. FLARITY
PROJECT MANAGER: W.A. HASBACH

PREPARED BY: N.F. SHEPARD, JR.
R.A. LOHNES
S.M. KAPLAN

P. PEREZ
M.J. GAITENS

APPROVED BY: K.L. Hanson
K.L. HANSON
PROJECT MANAGER

THIS WORK WAS PERFORMED FOR THE JET
PROPULSION LABORATORY, CALIFORNIA
INSTITUTE OF TECHNOLOGY, AS SPONSORED
BY THE NATIONAL AERONAUTICS AND SPACE
ADMINISTRATION UNDER CONTRACT NAS 7-100

GENERAL  ELECTRIC

SPACE SYSTEMS ORGANIZATION
Valley Forge Space Center

P. O. Box 8555 • Philadelphia, Penna. 19101

"This report contains information prepared by the General Electric Company, Space Systems Organization, under JPL Subcontract. Its content is not necessarily endorsed by the Jet Propulsion Laboratory, California Institute of Technology, or the National Aeronautics and Space Administration.

ABSTRACT

Results of the activities performed during the fourth quarter of the project to design and develop the technology of a 30-watt per pound rollup solar array are reported. During this quarter, the mechanical assembly of the prototype test model was completed with the exception of the installation of the blanket substrates on the storage drums. The assembly of these blankets was completed. The detailed planning associated with system testing proceeded along with the fabrication and assembly of associated support and test equipment.

TABLE OF CONTENTS

<u>Section</u>	<u>Page</u>
1 INTRODUCTION AND SUMMARY	1-1
2 TECHNICAL DISCUSSION	2-1
2.1 Design and Analysis	2-1
2.1.1 Prototype Array Blankets	2-1
2.1.2 Weight Summary	2-9
2.1.3 Deployed Dynamics Analysis	2-9
2.2 Fabrication and Procurement	2-22
2.2.1 General	2-22
2.2.2 Solar Panel Actuator	2-22
2.2.3 Leading Edge Member	2-24
2.2.4 Center Support	2-25
2.2.5 Storage Drums	2-25
2.2.6 Outboard End Supports	2-29
2.2.7 Slip Ring Assembly	2-30
2.2.8 Array Blanket	2-31
2.3 Development Testing	2-37
2.3.1 Bi-Stem Thermal Bending Test	2-37
2.3.2 Module Thermal Cycling Test	2-46
2.3.3 Array Structure Load Deflection Test	2-47
2.3.4 Bi-Stem Component Vibration Test	2-65
2.3.5 Airesearch Motor/Gearhead Test	2-66
2.4 System Test Planning	2-72
2.4.1 Deployed Modal Test	2-72
2.4.2 Stowed Modal Test	2-74
2.5 GSE and Test Equipment Design	2-88
2.5.1 Performance Test Rack	2-88
2.5.2 Module Illuminator	2-89
2.5.3 Holding Fixture	2-89
2.5.4 Deployment Aids	2-90
2.5.5 Deployed Modal Test Equipment	2-91
3 CONCLUSIONS	3-1
4 RECOMMENDATIONS	4-1
5 NEW TECHNOLOGY	5-1
6 REFERENCES	6-1

TABLE OF CONTENTS (Cont'd)

<u>Section</u>	<u>Page</u>
APPENDIX A. DERIVATION OF FLEXIBILITY INFLUENCE COEFFICIENTS FROM LOAD DEFLECTION TEST DATA	A-1
APPENDIX B. CALCULATION OF FLEXIBILITY INFLUENCE COEFFICIENTS FROM LOAD DEFLECTION TEST DATA	B-1
APPENDIX C. SYMMETRIC MODE SHAPES - 26 FT LENGTH	C-1
APPENDIX D. ANTISYMMETRIC MODE SHAPES - 26 FT LENGTH	D-1
APPENDIX E. SYMMETRIC MODE SHAPES - 13 FT LENGTH	E-1
APPENDIX F. ANTISYMMETRIC MODE SHAPES - 13 FT LENGTH	F-1
APPENDIX G. IN-PLANE MODE SHAPE PLOTS - 13 AND 26 FT DEPLOYED LENGTHS	G-1

LIST OF ILLUSTRATIONS

<u>Figure</u>		<u>Page</u>
1-1	Master Schedule	1-3
2.1-1	Module Details.	2-3
2.1-2	I-V Curve - GE No. 1 Module (19p x 20s).	2-5
2.1-3	I-V Curve - GE No. 2 Module (19p x 20s).	2-5
2.1-4	I-V Curve - GE No. 3 Module (19p x 20s).	2-6
2.1-5	I-V Curve - GE No. 4 Centralab Module No. 1 (19p x 20s)	2-6
2.1-6	I-V Curve - EOS Module (18p x 20s)	2-7
2.1-7	I-V Curve - Heliotek Module (19p x 20s)	2-7
2.1-8	I-V Curve - Boeing Module (18p x 20s).	2-8
2.1-9	I-V Curve - Spectrolab Module (12p x 20s)	2-8
2.1-10	Active Module Locations on Prototype Blankets	2-10
2.1-11	In-plane Configuration	2-15
2.1-12	Target Numbering System	2-17
2.2-1	RA250 Mechanical Assembly (Less Solar Array Blankets)	2-22
2.2-2	Solar Panel Actuator	2-23
2.2-3	Leading Edge Member	2-25
2.2-4	Center Support	2-26
2.2-5	Shear Diagrams for the RA250 Dynamic Model	2-28
2.2-6	Inboard End Cap Assembly	2-29
2.2-7	Outboard End Support	2-30
2.2-8	Slip Ring Assembly	2-31
2.2-9	Substrate Stretching Setup	2-32
2.2-10	Installation of Active Solar Array Modules	2-33
2.2-11	Array Blankets	2-34
2.2-12	EOS Module Mounted on G1 Blanket Assembly	2-34
2.2-13	Heliotek (near), GE No. 2 (middle), and Boeing (far) Modules Mounted on G1 Blanket Assembly	2-35
2.2-14	Spectrolab Module Mounted on G1 Blanket Assembly	2-35
2.2-15	GE No. 1 (left) and Centralab No. 1 (right) Modules Mounted on G1 Blanket Assembly	2-36
2.2-16	GE No. 3 Module Mounted on G2 Blanket Assembly	2-36
2.3-1	Thermal Bending Test Setup (NASA G-69-4536).	2-37
2.3-2	Idealized Tip Deflection Patterns	2-39
2.3-3	Extrapolated Absolute Zero-g Thermal Bending at 33.5 Ft	2-40
2.3-4	Extrapolated Absolute Zero-g Thermal Bending at 33.5 Ft	2-44
2.3-5	Thermal Cycling Module Test Setup	2-46
2.3-6	Typical Active Module Temperature Profile	2-47
2.3-7	Examples of Deformed Expanded Metal Interconnect Loop	2-48
2.3-8	Load Deflection Tests	2-49
2.3-9	Test Arrangements	2-51
2.3-10	Effects of Free-Play on Load-Deflection Curves	2-55

LIST OF ILLUSTRATIONS (Cont'd)

<u>Figure</u>	<u>Page</u>
2.3-11 Results of Test 1A, Symmetric Loading in X-Direction	2-57
2.3-12 Results of Test 2A, Antisymmetric Loading in X-Direction.	2-57
2.3-13 Results of Test 3A, Symmetric Loading in Z-Direction	2-58
2.3-14 Results of Test 4A, Antisymmetric Loading in Z-Direction.	2-58
2.3-15 Comparison of Bearing Flexibility Coefficient with Alley-Leadbetter Joint Flexibility Curves.	2-61
2.3-16 Extrapolated Temperature Rise for the Airesearch P/N 36790-1-1 Gearhead dc Motor	2-68
2.4-1 Array Optical Target and Tracker Distribution	2-73
2.4-2 Deployed Modal Test Exciter Control and Data Handling Block Diagram.	2-75
2.4-3 Schematic Stowed Configuration Modal Test Arrangements	2-77
2.4-4 RA258 Rollup Solar Array Stowed Model Test Accelerometer Locations	2-82
2.5-1 Performance Test Rack.	2-88
2.5-2 Module Illuminator	2-89
2.5-3 Upward Deployment Aid	2-90
2.5-4 Deployed Modal Test Equipment Installation	2-93
2.5-5 Modal Support Structure	2-95
2.5-6 Deployed Modal Test Support Fixture	2-95

SECTION 1

INTRODUCTION AND SUMMARY

A program to generate a detailed design, fabricate, assemble and test a 250-square foot rollup subsolar array capable of providing a minimum of 30 watts of electrical power per pound of subsolar array weight was initiated on March 5, 1969. The term subsolar array is used to indicate the item being developed is one unit of a solar array system that typically would utilize four identical units to provide the electrical power requirements for an interplanetary spacecraft design concept. Each subsolar array is a complete subsystem with respect to a spacecraft application, and the design requirements are intended to provide a technology base that applies to other mission applications. An extensive environmental test program is planned to establish the integrity of the design for spacecraft applications, to provide performance data, and to verify analysis techniques that will have application to large-area lightweight solar array designs based on the rollup concept.

The design of the rollup subsolar array is based on the concepts and technology developed in the Feasibility Study for a 30 Watts per Pound Rollup Solar Array (JPL Contract 951970) and was documented in the References 1 and 2. For convenience, the 250-square foot rollup subsolar array unit will be referred to as the RA250.

This fourth quarterly report describes the technical results achieved from December 1, 1969 to February 28, 1970. During this period, the program emphasis has been focused on the completion of the RA250 mechanical assembly and on the completion of the array blanket fabrication including the installation of active solar cell modules.

The final assembly of the structural components was accomplished without major problems. The bonding of the storage drum shells resulted in lower lap shear strength than anticipated. A stress review of these joints has shown that the achieved shear strength is adequate for this application. The Bi-Stem solar panel actuator satisfactorily passed a component vibration test and subsequent ambient performance test. The unit was delivered and mounted

on the center support structure. The leading edge member was received from the vendor and installed at the final mechanical assembly. The two slip-ring assemblies were received and installed in the inboard end caps.

The two solar array blankets needed for the prototype test model have been fabricated. Six different types of active solar cell modules have been installed on these blankets. All active modules were tested prior to installation. The remainder of the blanket area is covered with glass platelets which simulate the mass and stiffness of the solar cell modules. Both blankets have been rolled on 8-inch cylinders during the fabrication process.

The actual weight of the RA250 prototype test model is 82.5 lb. The resulting power-to-weight ratio is $2500/82.5 = 30.3$ watt/lb.

The fabrication and assembly of all ground handling equipment is complete. Special test equipment fabrication is proceeding satisfactorily. The modal test equipment is in the process of final assembly with checkout scheduled for mid-March.

The system test activity has been concentrated on the detailed planning for the deployed modal test and with the instrumentation of the test specimen for subsequent stowed dynamics tests and thermal vacuum tests. Internally mounted strain gages, thermocouples, and accelerometers were installed during the final assembly sequence. Additional external accelerometers, strain gages and thermocouples will be added prior to the tests requiring them.

The master program schedule is shown in Figure 1-1. Analyses activities were extended to support test planning activities. The fabrication cycle was extended to account for the delay in delivery of the solar panel actuator and to allow incorporation of the solar cell module samples. During January, activity on environmental test planning and test equipment was suspended to allow a review of the plan for the remainder of the program. Work was resumed in early February and the completion dates for these activities was rescheduled.

EVENTS	1969												1970			
	M	A	M	J	J	A	S	O	N	D	J	F	M	A	M	J
	1	2	3	4	5	6	7	8	9	10	11	12	13	14	15	16
PROGRAM PLAN	◇	▽														
ANALYSIS	◇	▲					◇			◇					▽	
DETAIL ARRAY DESIGN	◇	▲			▼											
JPL DESIGN REVIEWS	◇	▽			▼											
FABRICATION CYCLE					△	▲				◇					▽	
SUPPORT EQUIPMENT DESIGN					▲					◇					▽	
SUPPORT EQUIPMENT FABRICATION					▲					▼				◇	▽	
DETAILED TEST PLAN										PARTIAL ▼				▽		
DEVELOPMENT TESTS					▲					◇				▲		
ARRAY TEST SEQUENCE										◇				▲		▽

Figure 1-1. Master Program Schedule

SECTION 2

TECHNICAL DISCUSSION

2.1 DESIGN AND ANALYSIS

2.1.1 PROTOTYPE ARRAY BLANKETS

A total of 11 active solar cell modules are planned for the prototype array blankets. In order to incorporate a representative sampling of various interconnection approaches, several recognized solar array fabricators were invited to supply sample modules fabricated with established production techniques. Table 2.1-1 lists each of these modules along with the overall dimensions in the series and parallel direction. The weight of each module reflects the basic difference in the interconnect design. The last column represents the total weight differential if that particular module configuration were used for a flight array (based on a nominal 19 p x 20s module weight of 111 grams). The photoetched interconnect designs would add significant weight to a flight array. The Kovar expanded metal (Centralab) interconnect is slightly heavier due to the 3 mil basic metal thickness as opposed to 2 mils for the silver expanded metal. The solderless interconnect approach furnished by Boeing is slightly lighter than the baseline GE module. Figure 2.1-1 shows a close-up photograph of the front and rear sides of a typical solar cell within each of the module configurations described in Table 2.1-1.

An I-V curve was obtained on each of these modules prior to bonding on the substrate. Figures 2.1-2 through 2.1-9 show these curves for each module received to date. The module temperatures indicated on each curve were obtained from thermocouples which were bonded to the rear side of the two cells within each module. These thermocouples remain attached to each module when bonded to the substrate. These I-V curves were obtained with a tungsten illuminator. Equivalent 1 AU, air mass zero intensity was established through the use of a JPL supplied standard cell (BFS 307).

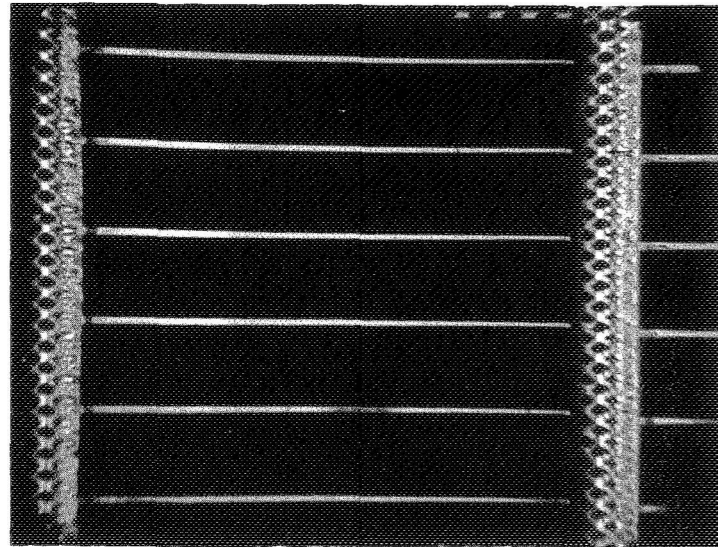
A similar I-V curve will be obtained on each module at specified points in the test cycle to determine possible degradation due to environmental testing.

Table 2.1-1. Solar Cell Module Summary

Module Designation	Size	Dimension Series Direction (in.)	Dimension Parallel Direction (in.)	Weight (gm)	Weight per Cell (gm)	Interconnect Configuration	Total* Weight Differential (lb)
GE No. 1	19p x 20s	16.28	15.17	112.5	0.2961	Ag expanded metal, zone solder plated	+0.49
GE No. 2	19p x 20s	16.30	15.17	108.5	0.2855	Ag expanded metal, zone solder plated	-0.80
GE No. 3	19p x 20s	16.25	15.22	113.5	0.2987	Ag expanded metal, zone solder plated	+0.80
Boeing	18p x 20s	16.14	14.56	99.5	0.2764	Ag expanded metal, no solder	-1.91
EOS	18p x 20s	16.34	14.55	122.8	0.3411	Photoetched, Ag plated Kovar	+5.96
Spectrolab	12p x 20s	16.31	9.63	81.0	0.3375	Photoetched, Ag plated Be Cu	+5.52
Heliotek	19p x 20s	16.33	15.24	135.5	0.3566	Photoetched, Ag plated Be Cu, Wrap-around Configuration	+7.85
Centralab No. 1	19p x 20s	16.56	15.25	121.0	0.3184	Koval expanded metal, Ag plated	+3.20
Centralab No. 2	} To Be Received						
Centralab No. 3							
Centralab No. 4							

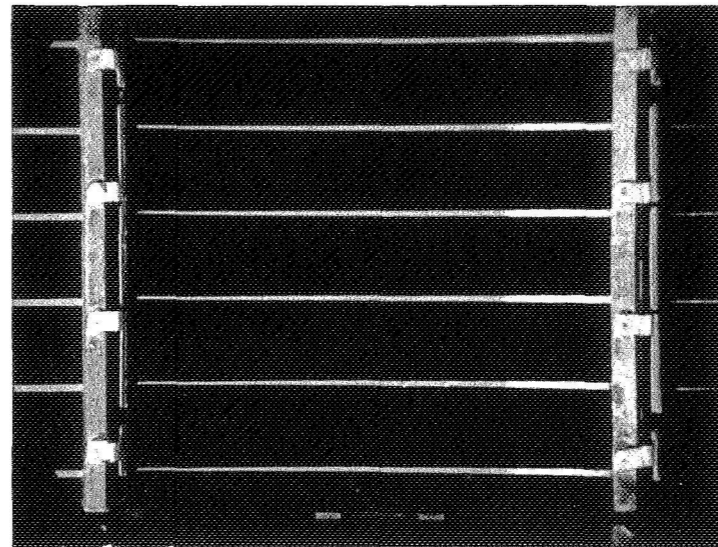
*Total array weight increase (or decrease) if this module configuration is used on the flight array (based on nominal 19p x 20s module weight of 111 gm).

Centralab Module (19p x 20s)



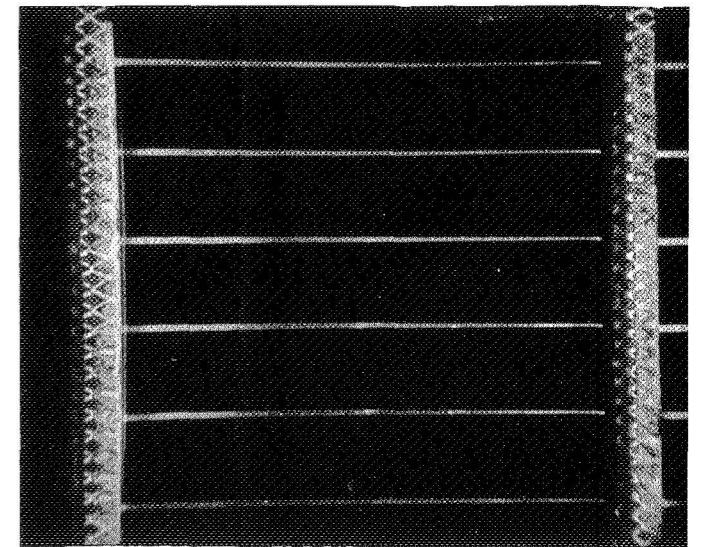
(a) Front Side

Spectrolab Module (12p x 20s)

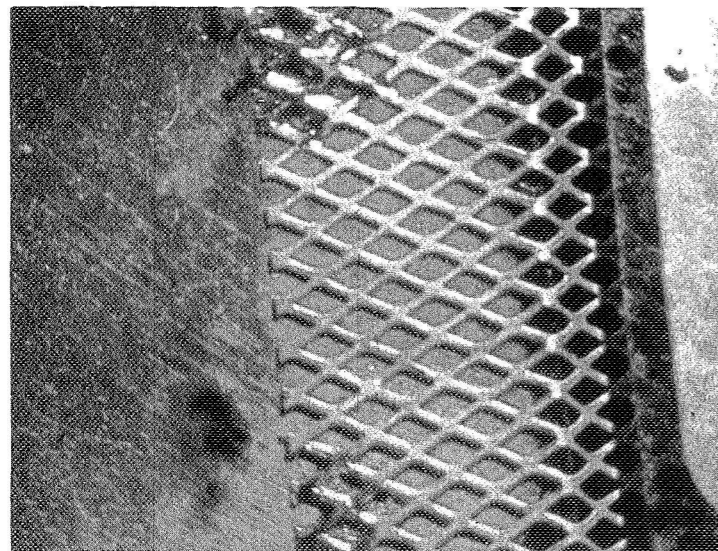


(a) Front Side

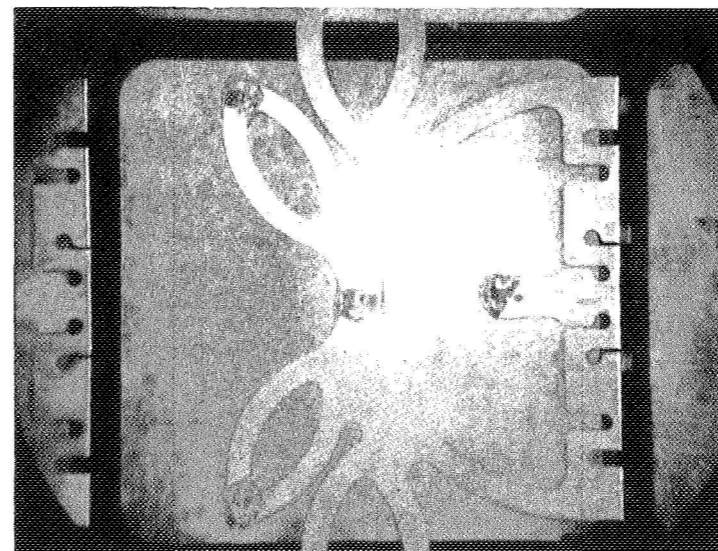
GE Module (19p x 20s)



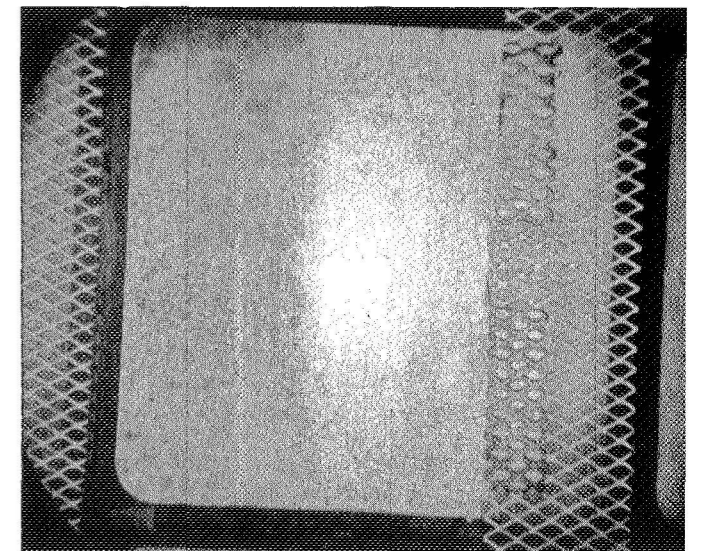
(a) Front Side



(b) Rear Side

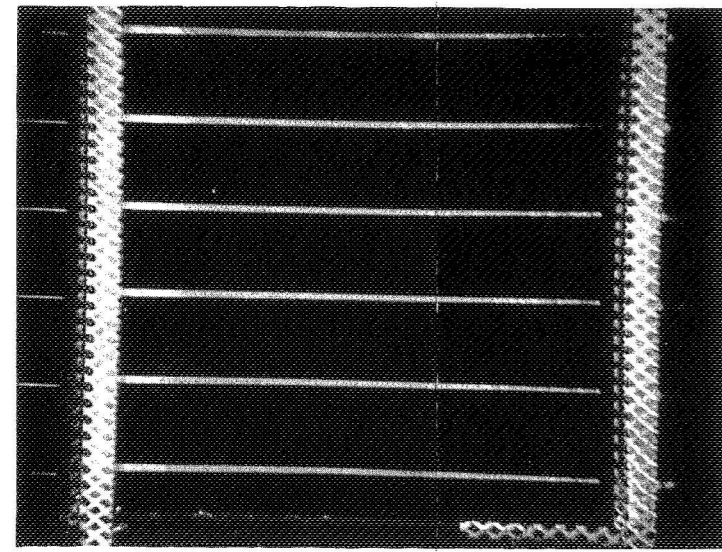


(b) Rear Side



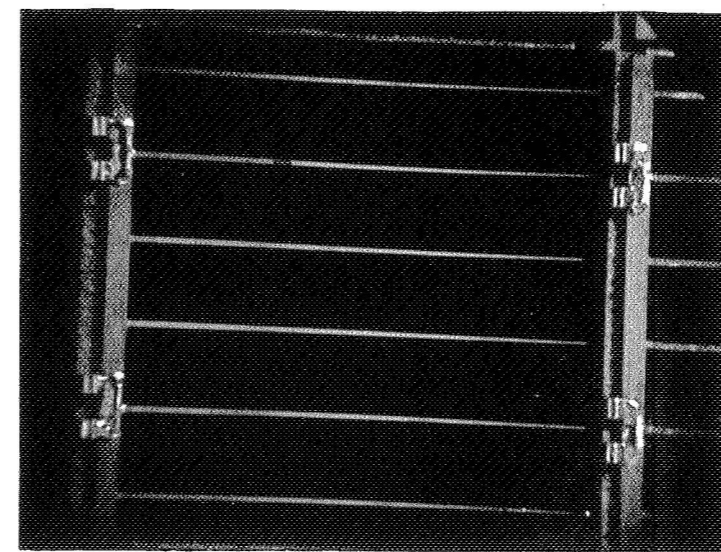
(b) Rear Side

Boeing Module (18p x 20s)



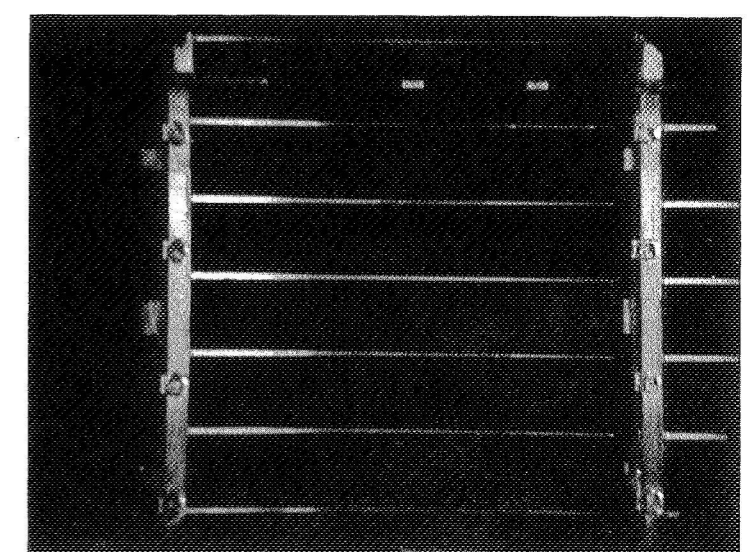
(a) Front Side

EOS Module (18p x 20s)

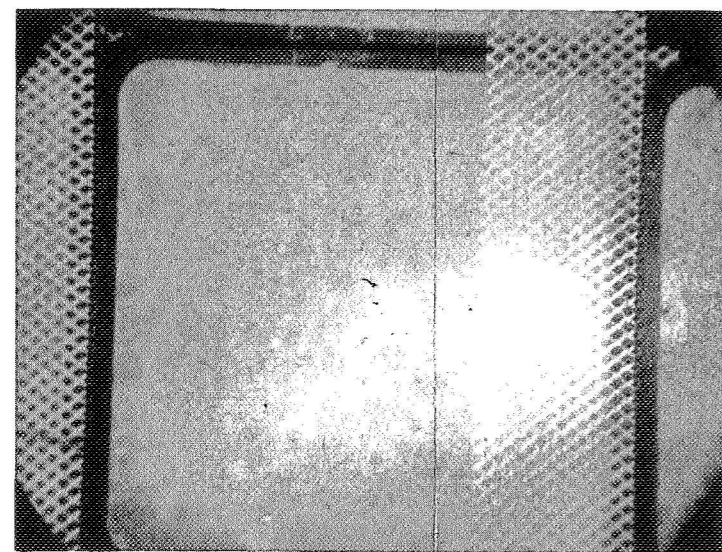


(a) Front Side

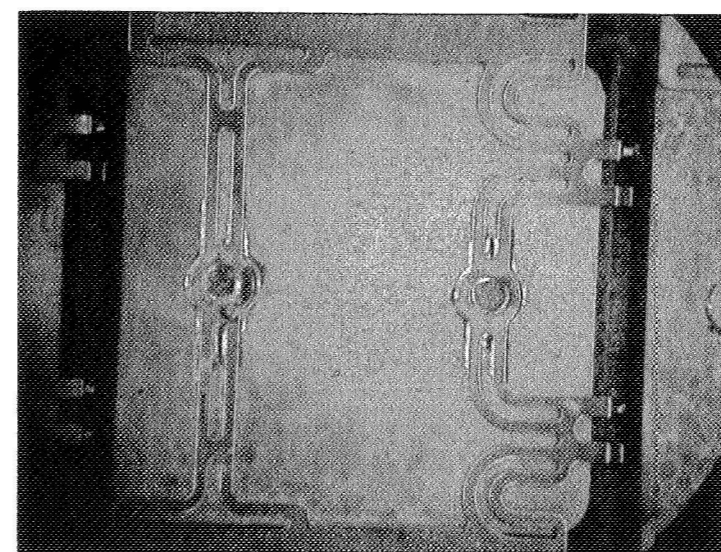
Heliotek Module (19p x 20s)



(a) Front Side



(b) Rear Side



(b) Rear Side



(b) Rear Side

Figure 2.1-1. Module Details

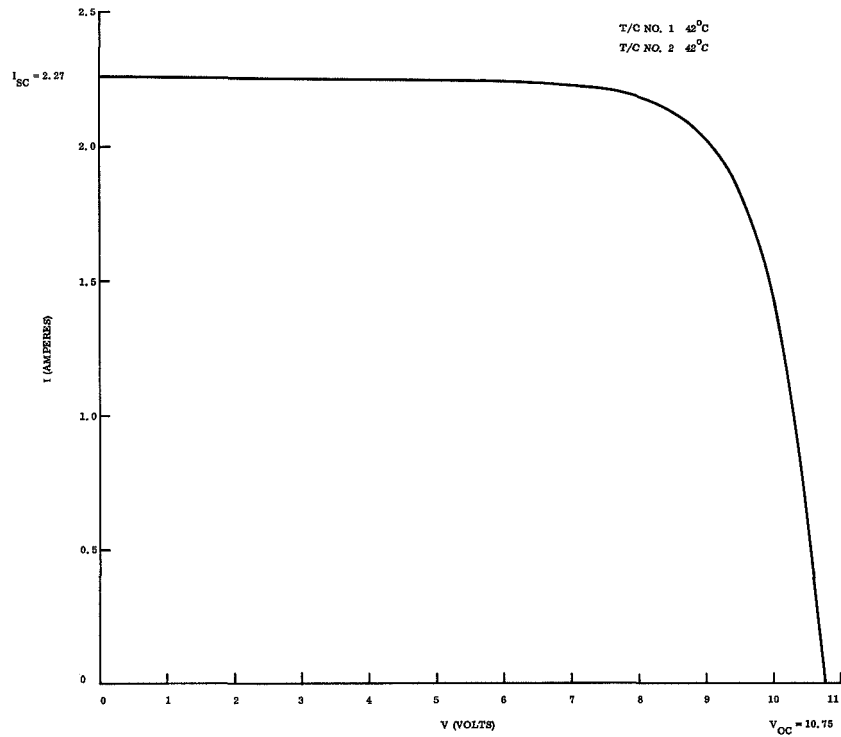


Figure 2.1-2. I-V Curve - GE No. 1 Module (19p x 20s)

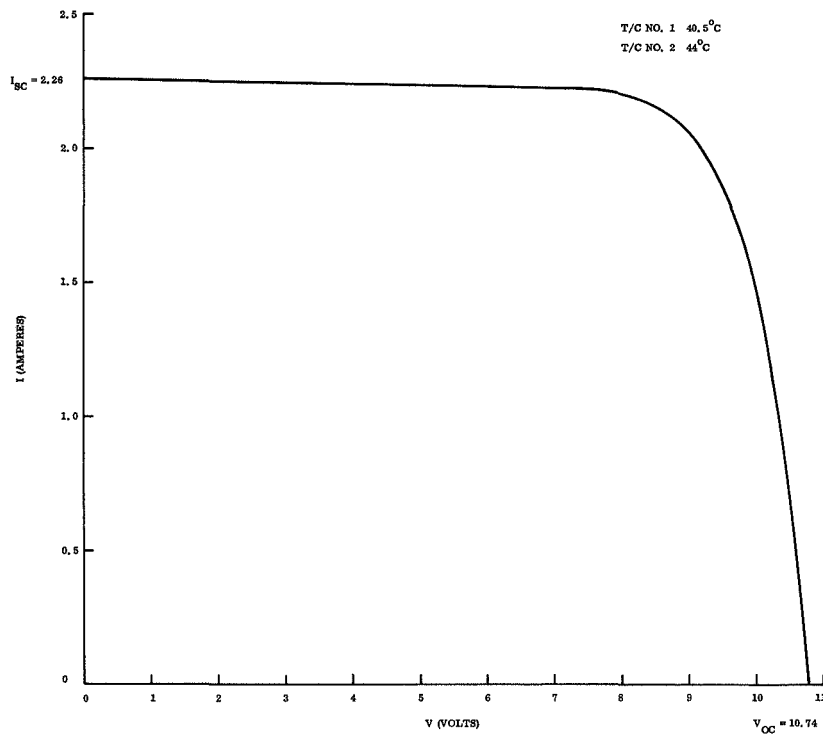


Figure 2.1-3. I-V Curve - GE No. 2 Module (19p x 20s)

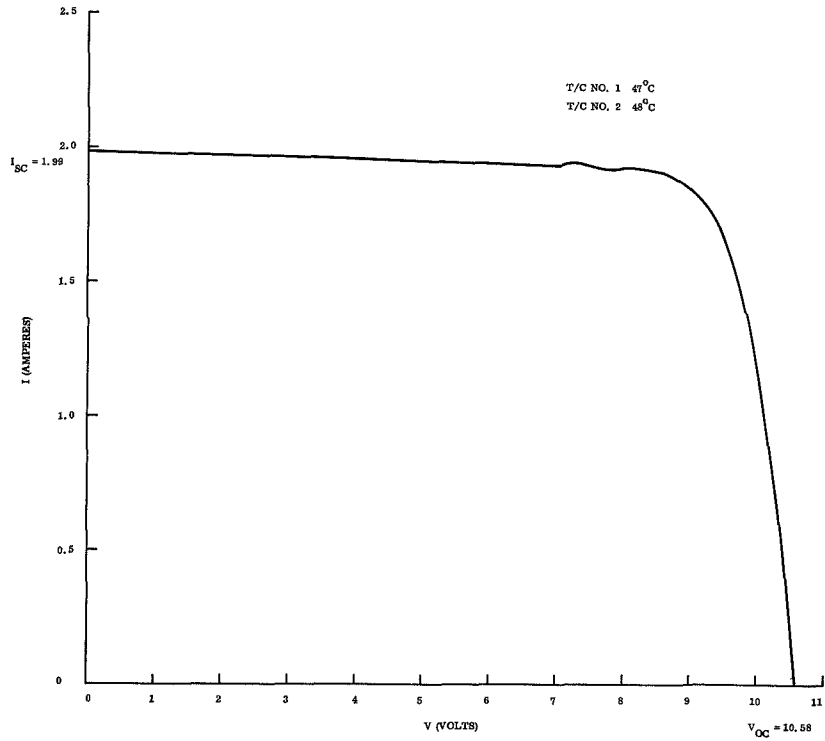


Figure 2.1-4. I-V Curve ~ GE No. 3 Module (19p x 20s)

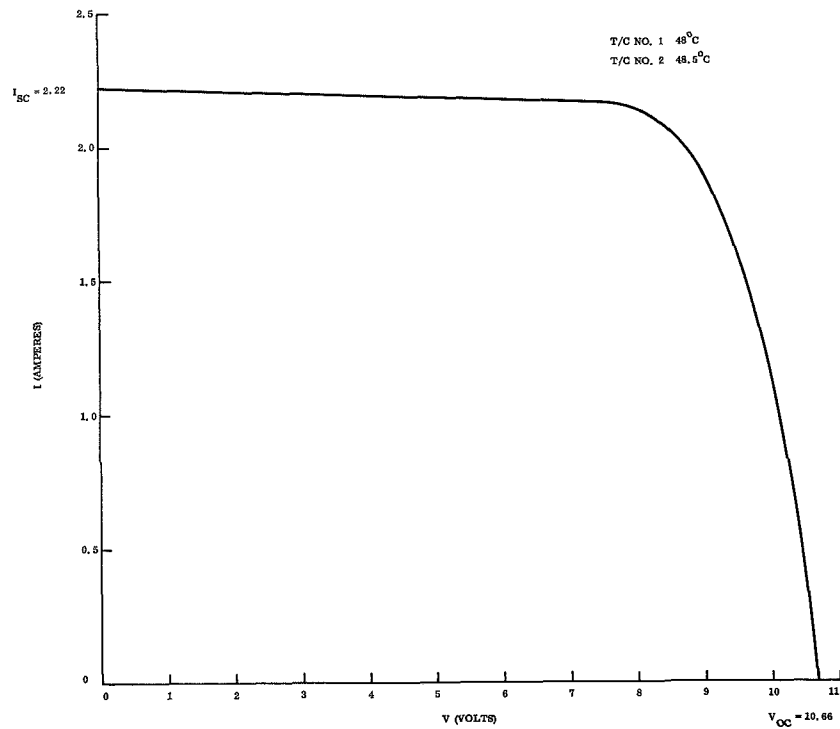


Figure 2.1 5. I-V Curve - Centralab No. 1 Module (19p x 20s)

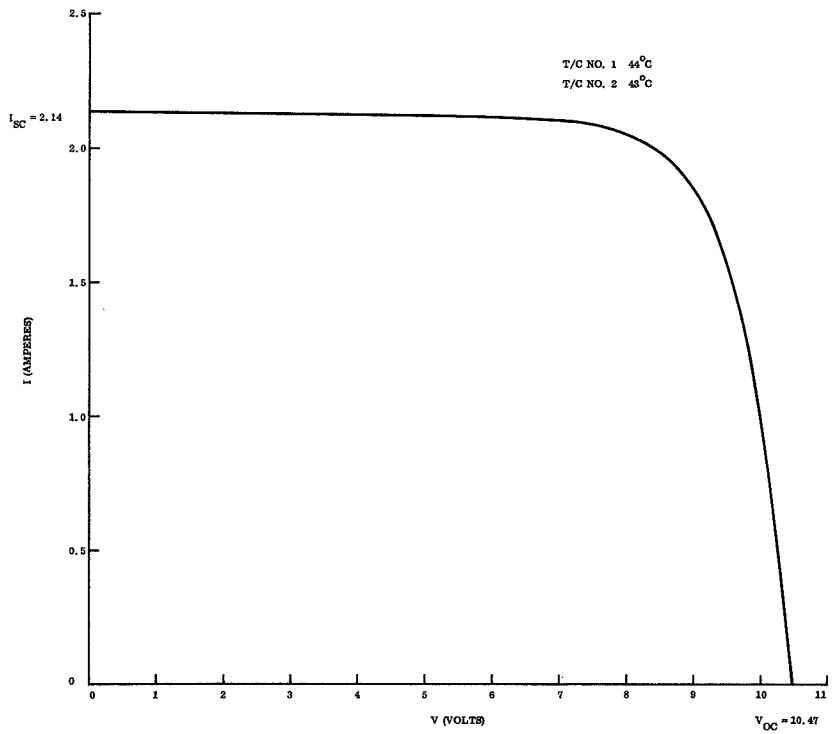


Figure 2.1-6. I-V Curve - EOS Module (18p x 20s)

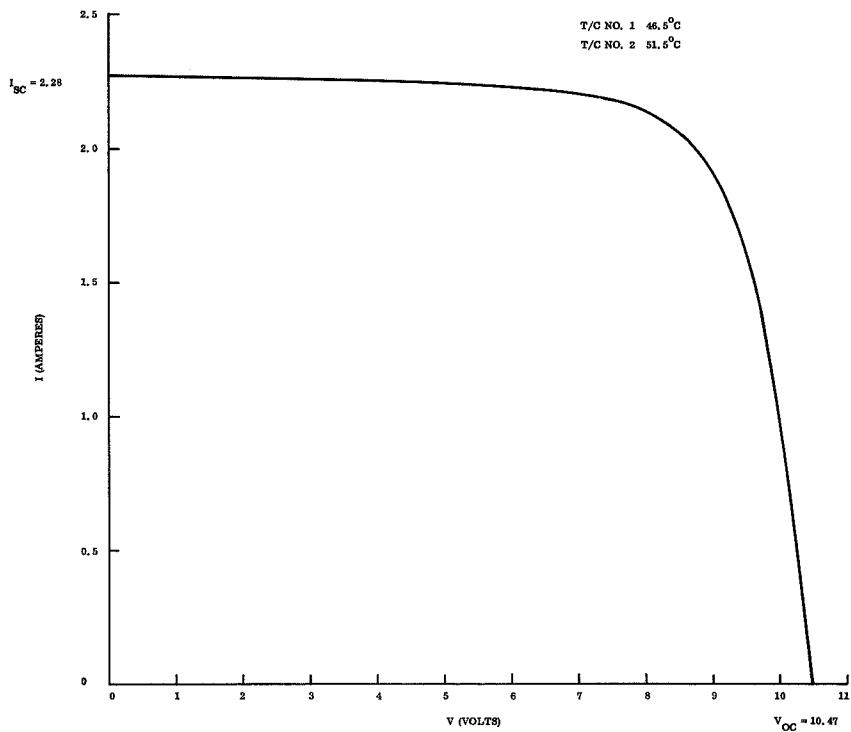


Figure 2.1-7. I-V Curve - Heliotek Module (19p x 20s)

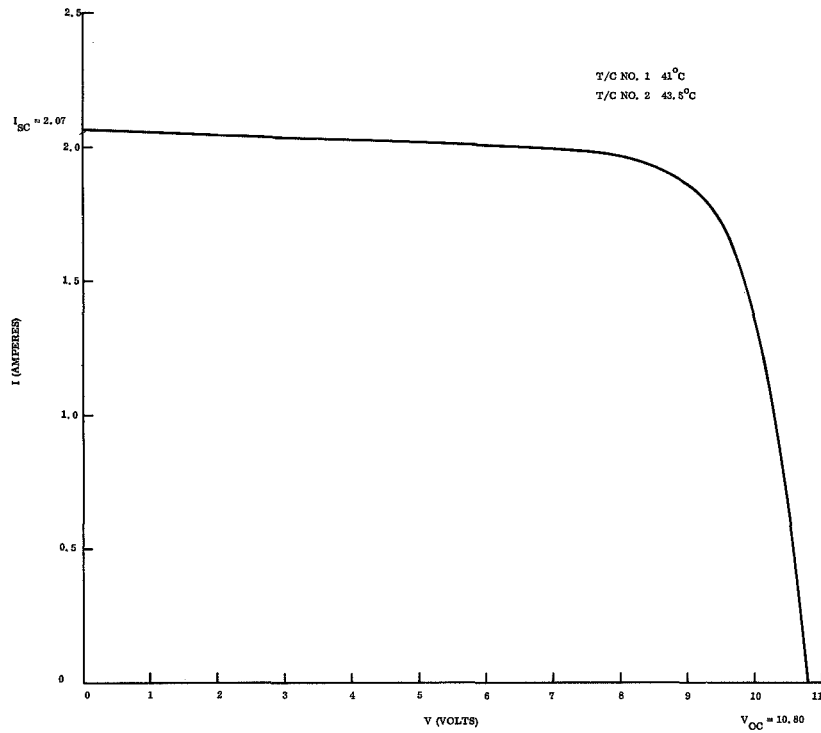


Figure 2.1-8. I-V Curve - Boeing Module (18p x 20s)

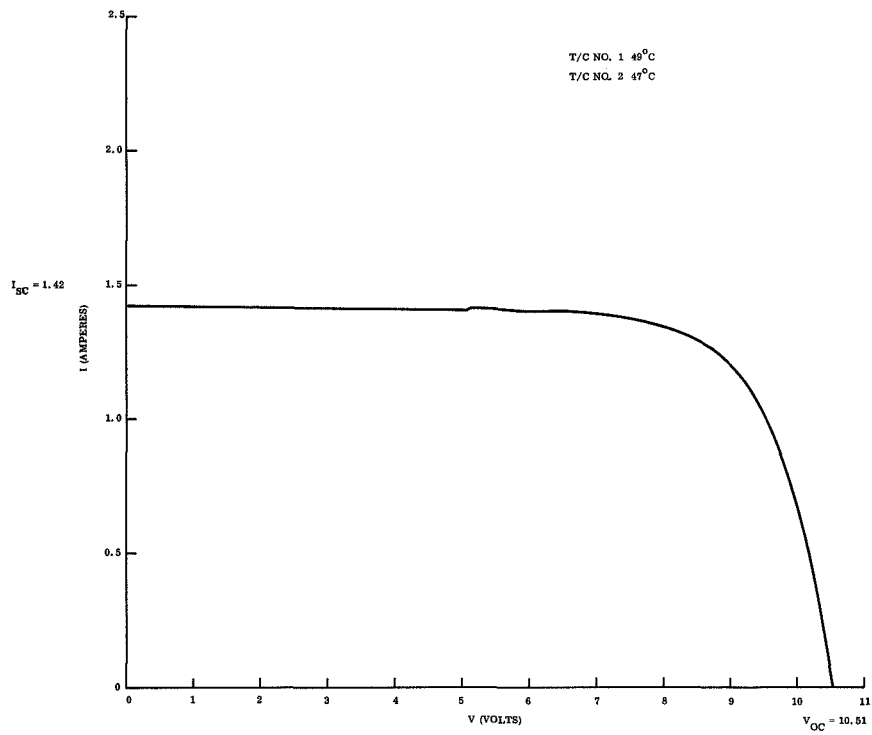


Figure 2.1-9. I-V Curve - Spectrolab Module (12p x 20s)

Figure 2.1-10 shows the layout of these active solar cell modules on the prototype blankets. A total of 4000 solar cells will be bonded to these two blankets. The remaining area is covered with glass platelets joined with Kapton tape.

2.1.2 WEIGHT SUMMARY

The current weight summary for the prototype unit is shown in Table 2.1-2. This table has been condensed from the detailed weight breakdown which appears in reference 2 (see Section 6) since it reflects the actual weights of major subassemblies rather than individual piece part weights. The actual weight of the complete assembly less both blankets is 36.0 lb. This does not include 0.76 lb of nonflight test instrumentation which has been added during the assembly. The G1 array blanket assembly weighs 23.22 lb complete with all active solar cell modules. The actual weight of the G2 array blanket assembly is 23.36 lb. This weight includes three dummy modules which were temporarily substituted for the Centralab modules No. 2, 3, and 4 which are to be delivered. These additional active modules will be installed in place of the dummy modules following the completion of the deployed modal test.

Thus, the present weight of the prototype model is 82.5 lb. Based on this weight, the array power-to-weight ratio is $2500/82.5 = 30.3$ watt/lb. This weight should be reduced slightly by the subsequent installation of the three additional active modules in place of the heavier temporary dummy modules. For a flight model, this weight could be reduced to 79.3 lb (or 31.5 watt/lb) by the implementation of the following changes as described in reference 2.

1. Replace magnesium drum shells with beryllium
2. Remove Schjel-clad residual adhesive
3. 100 percent solar cell coverage instead of heavier dummy modules.

2.1.3 DEPLOYED DYNAMICS ANALYSIS

An analysis of the deployed rollup array in the modal test configuration with deployed length of 26 and 13 feet was performed to obtain the natural frequencies and mode shapes for both

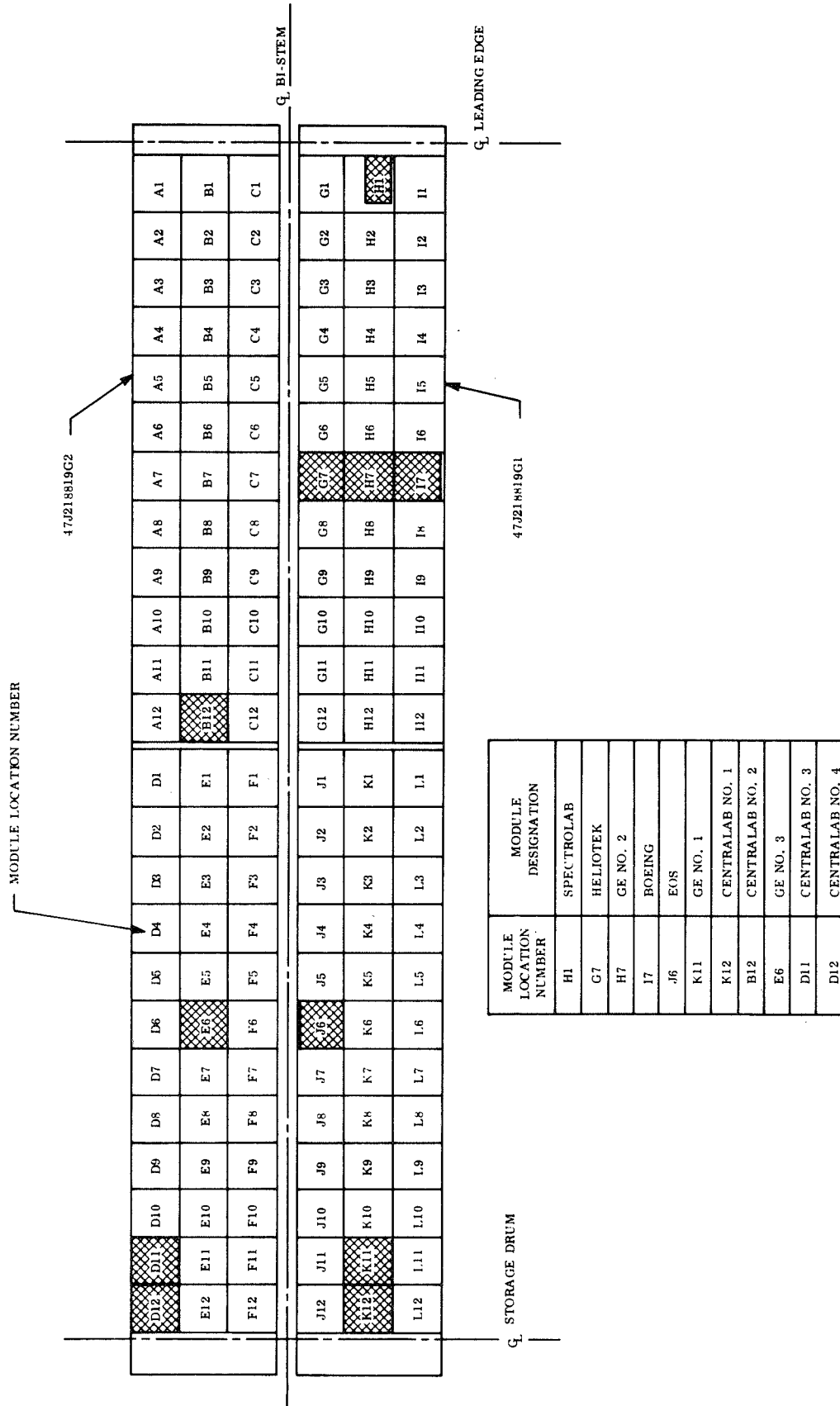


Figure 2.1-10. Active Module Locations on Prototype Blankets

Table 2.1-2. Actual Weight Summary (Prototype Model)

Nomenclature		Drawing No.	Unit Weight (lb)	Qty/ Next Assy	Total Weight (lb)
RA250	Prototype Assembly	47E214519G2	-	-	82.5
	Center Support	47E218547	1.33	1	1.33
	Leading Edge Member	-	0.85	1	0.85
	Boom Actuator	-	11.73	1	11.73
	LEM Support Brackets	-	0.11	2	0.22
	Outboard End Support	-	2.05	2	4.10
	Movable Portion	-	1.31	1	-
	Fixed Portion	-	0.69	1	-
	Bolt	-	0.05	1	-
	Drum Assembly	47E218804 G3 & G4	8.80	2	17.60
	Guide Flange	47D218535 G3 & G4	0.38	2	-
	Drum Shell	47E218144G4	2.79	1	-
	Outboard End Cap Assembly	47E218194G3	0.45	1	-
	Inboard End Cap Assembly	47E218544 G1 & G2	4.80	1	-
	Mounting Hardware (Drum-to-Center Support)	-	-	-	0.13
	Prototype Array Blanket Assembly	475218819G1	23.22	1	23.22
	Prototype Array Blanket Assembly	47J218819G2	23.36	1	23.36

out-of-plane vibrations (bending and torsion) and in-plane vibrations.* These results are presented below:

2.1.3.1 Out-of-Plane Analysis

This analysis includes the effect of the 1g field which establishes a gravity gradient in the blanket due to the blanket weight, but is limited in its scope by the following assumptions and constraints:

1. The effect of the stiffness of the individual cell interconnects is not included.
2. The antisymmetric analysis does not include the nonlinear effect of the variation of membrane tension and/or the "buckling out" of portions of the blanket in the torsion modes.
3. The deployed Bi-Stem rod is assumed to have uniform structural properties along its length ($EI = 2.39 \times 10^3 \text{ lb-ft}^2$).
4. The effect of the rotational inertia of the stowage drum and the deployment aid is not included.

The frequencies of the first 12 symmetric and antisymmetric modes for the 26 and 13 foot lengths are summarized in Tables 2.1-3 and 2.1-4, respectively. The corresponding first six mode shape plots are presented in Appendix C and D for the 26-foot length and in Appendix E and F for the 13-foot length. It is noted that the mode shapes for the 1g case differ from the zero g mode shapes which were obtained for other length arrays (reference 2). The 1g mode shapes result in more of a pendulum type motion and less array 'billowing' than is evident in the zero g mode shapes.

The rod motion in the four array bending modes presented does not have a node line except at the rod root, while the blanket has the node line as expected. This is not the case with zero g case where the blanket and rod exhibit the same number of node lines. There is also a shifting of the node lines toward the free or bottom edge of the array in the higher modes.

*These lengths represent test conditions being planned (or considered).

Table 2.1-3. Frequency Summary for 26-Foot Deployed Array
(1g field)

Out of Plane Modes

	Mode	Frequency (Hz)	Description
Symmetric	1	0.248	1st Array Bending
	2	0.392	Membrane Mode
	3	0.392	Membrane Mode
	4	0.561	2nd Array Bending
	5	0.806	Membrane Mode
	6	0.806	Membrane Mode
	7	0.917	3rd Array Bending
	8	1.24	Membrane Mode
	9	1.24	Membrane Mode
	10	1.32	4th Array Bending
	11	1.72	Membrane Mode
	12	1.72	Membrane Mode
Antisymmetric	1	0.232	1st Array Torsion
	2	0.392	Membrane Mode
	3	0.392	Membrane Mode
	4	0.580	2nd Array Torsion
	5	0.807	Membrane Mode
	6	0.807	Membrane Mode
	7	0.958	3rd Array Torsion
	8	1.246	Membrane Mode
	9	1.246	Membrane Mode
	10	1.365	4th Array Torsion
	11	1.722	Membrane Mode
	12	1.722	Membrane Mode

Table 2.1-4. Frequency Summary for 13-Foot Deployed Array
(1g Field)
Out of Plane Modes

	Mode	Frequency (Hz)	Description
Symmetric	1	0.418	1st Array Bending
	2	0.551	Membrane Mode
	3	0.551	Membrane Mode
	4	0.832	2nd Array Bending
	5	1.126	Membrane Mode
	6	1.126	Membrane Mode
	7	1.296	3rd Array Bending
	8	1.732	Membrane Mode
	9	1.732	Membrane Mode
	10	1.842	4th Array Bending
	11	2.385	Membrane Mode
	12	2.385	Membrane Mode
Antisymmetric	1	0.298	1st Array Torsion
	2	0.551	Membrane Mode
	3	0.551	Membrane Mode
	4	0.775	2nd Array Torsion
	5	1.126	Membrane Mode
	6	1.126	Membrane Mode
	7	1.298	3rd Array Torsion
	8	1.732	Membrane Mode
	9	1.732	Membrane Mode
	10	1.864	4th Array Torsion
	11	2.385	Membrane Mode
	12	2.385	Membrane Mode

The multiple membrane modes identified in Tables 2.1-3 and 2.1-4 are characteristics of the mathematical model and are not expected to be seen as multiple modes in the modal test.

2.1.3.2 In-Plane Analysis

An in-plane vibration analysis of the same modal test configuration (in the 1g field) with deployed array lengths of 26 and 13 feet has been performed using the method of analysis described in Appendix A of reference 2. During this analysis, an error was discovered in the consistent mass matrix for a rectangular elastic sheet presented in the paper by Schmidt, Fox, and Bogner (reference 3). This error appears as equation (I-7) of Appendix A in reference 2. The absolute values shown in this matrix are correct but all elements should be positive in sign.

Figure 2.1-11 shows the basis configuration which is used in subsequent mode shape plots which appear in Appendix G. The fundamental natural frequency of in-plane vibrations is found to be slightly higher than that encountered for the out-of-plane vibrations. The second and higher modes have significantly higher frequencies than the corresponding modes for the out-of-plane vibration.

2.1.3.3 Orthogonality of Natural Modes

In order to anticipate the orthogonality to be expected in the measured modes during the deployed modal test, the following analysis was performed.

The theoretical mode shapes were interpolated to obtain the modal deflection pattern at the target locations. A mass was then lumped at each target location. Finally, the generalized mass matrix (M^*) was formed by

$$M^* = [\theta]^T [m] [\theta]$$

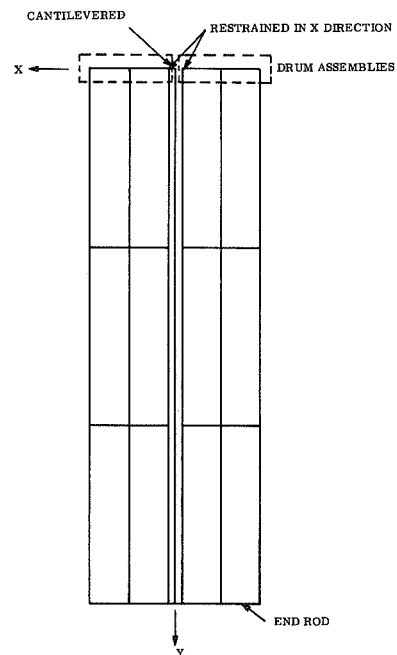


Figure 2.1-11. In-plane Configuration

where:

$[\theta]$ = matrix of modal deflections. Each column is a mode. Each row corresponds to a target.

$[m]$ = diagonal matrix of the masses lumped at each target.

The column of $[\theta]$ were normalized such that the diagonal terms of M^* are unity. The size of the off-diagonal terms in M^* then provides a measure of orthogonality of the modes, with a zero indicating perfect orthogonality.

Considering the target locations shown in Figure 2.1-12, and using the masses given in Table 2.1-5 and the mode shapes discussed in Section 2.1.3.1 and 2.1.3.2, six generalized mass matrixes were computed. These are presented in Tables 2.1-6 through 2.1-8. The modes used for Table 2.1-6 are those which respond to Z axis excitation (symmetric out-of-plane bending). The modes for Table 2.1-7 are the X axis modes (torsion) and the Y axis modes (in-plane bending) are used for Table 2.1-8.

As shown in Figure 2.1-12, data for the 26-foot deployment cases are based on 10 spanwise targets. For the 13-foot deployment, only the five outboard spanwise targets were used. In both cases, three chordwise stations were used per blanket.

Examining the generalized mass matrixes for the 26-foot deployment cases, it is found that good orthogonality is achieved except between the membrane modes. For the 13-foot cases, the coupling between the third and fourth bending modes has increased from 0.05 to only 0.15 even though the shape definition of the fourth mode with five stations is inadequate. The coupling between the membrane modes remain at the same level probably due to the chordwise coarseness. These results indicate that five spanwise stations are marginal to define the membrane modes while three chordwise stations are marginal to define the membrane modes. Based on this analysis, the masses presented in Table 2.1-5 can be used to

perform an orthogonality check of the measured modes. M^*_{ij} can be expected to be < 0.1 for 10 spanwise stations and < 0.2 for five spanwise stations for the bending modes and for the Y (in-plane) modes. Coupling between the membrane modes may be much higher, up to 0.4.

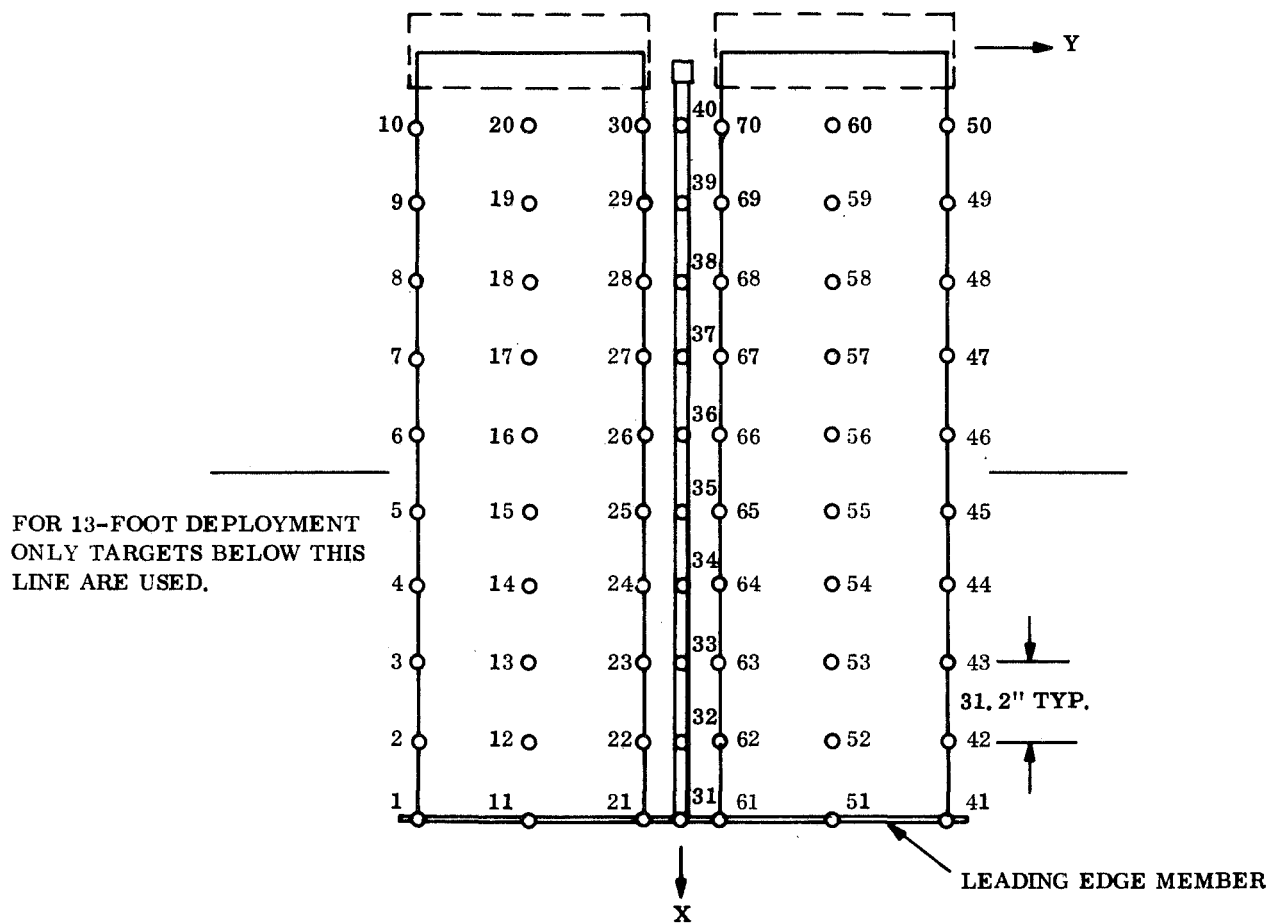


Figure 2.1-12. Target Numbering System

Table 2.1-5. Masses Associated with Target Locations

Target	Mass
1	8.4468500 / -4
2	1.1490798 / -3
3	1.1490798 / -3
4	1.1490798 / -3
5	1.1490798 / -3
6	1.1490798 / -3
7	1.1490798 / -3
8	1.1490798 / -3
9	1.1490798 / -3
10	1.1490798 / -3
11	1.2141150 / -3
12	2.2981597 / -3
13	2.2981597 / -3
14	2.2981597 / -3
15	2.2981597 / -3
16	2.2981597 / -3
17	2.2981597 / -3
18	2.2981597 / -3
19	2.2981597 / -3
20	2.2981597 / -3
21	7.8752437 / -4
22	1.1490798 / -3
23	1.1490798 / -3
24	1.1490798 / -3
25	1.1490798 / -3
26	1.1490798 / -3
27	1.1490798 / -3
28	1.1490798 / -3
29	1.1490798 / -3
30	1.1490798 / -3
31	1.0237512 / -3
32	1.3126632 / -3
33	1.3126632 / -3
34	1.3126632 / -3
35	1.3126632 / -3

Target	Mass
36	1.3126632 / -3
37	1.3126632 / -3
38	1.3126632 / -3
39	1.3126632 / -3
40	1.3126632 / -3
41	8.4468500 / -4
42	1.1490798 / -3
43	1.1490798 / -3
44	1.1490798 / -3
45	1.1490798 / -3
46	1.1490798 / -3
47	1.1490798 / -3
48	1.1490798 / -3
49	1.1490798 / -3
50	1.1490798 / -3
51	1.2141150 / -3
52	2.2981597 / -3
53	2.2981597 / -3
54	2.2981597 / -3
55	2.2981597 / -3
56	2.2981597 / -3
57	2.2981597 / -3
58	2.2981597 / -3
59	2.2981597 / -3
60	2.2981597 / -3
61	7.8752437 / -4
62	1.1490798 / -3
63	1.1490798 / -3
64	1.1490798 / -3
65	1.1490798 / -3
66	1.1490798 / -3
67	1.1490798 / -3
68	1.1490798 / -3
69	1.1490798 / -3
70	1.1490798 / -3

Mass Units are Lb-Sec²/Inch

Table 2.1-6. Generalized Mass Matrix for Z Modes
(Bending, Out-of-Plane)

	1st Bending			2nd Bending			3rd Bending			4th Bending*			
1.0	.000	.000	-.038	-.000	-.000	-.033	.000	.000	.023	.000	.000	.000	
	1.0	.131	.000	-.003	.000	.011	.002	-.000	-.000	.009	.001	.000	
		1.0	.000	-.020	.000	.001	.012	-.000	-.000	.001	.009	.000	
			1.0	.000	.000	-.006	-.000	-.012	.000	.000	-.000	-.000	
				1.0	.131	-.000	-.050	-.007	.000	-.024	-.003	-.000	
					1.0	-.000	-.006	-.005	-.000	-.003	-.024	-.000	
						1.0	-.000	-.049	-.000	-.000	-.000	-.000	
							1.0	-.001	.086	.011	.086	.000	
								1.0	-.000	.011	.086	.000	
									1.0	.000	.000	.000	
										1.0	.130	.130	
											1.0	1.0	
												1.0	
													1.0

Symmetric

26-Foot Deployment

1.0	.000	.000	-.063	.000	-.000	-.017	-.000	.000	-.049	.000	.000	.000
	1.0	.130	-.000	.001	-.000	.000	-.023	-.003	-.000	.075	.010	.000
		1.0	-.000	.000	-.001	.000	-.003	-.022	-.000	.010	.075	.000
			1.0	.000	-.000	.035	-.000	.000	-.107	.000	-.000	-.000
				1.0	-.130	.000	-.041	-.005	-.000	.193	.025	.000
					1.0	-.000	.005	.041	.000	-.025	-.193	.000
						1.0	-.000	-.145	.000	.000	.000	.000
							1.0	.130	-.000	.373	.049	.000
								1.0	-.000	.048	.372	.000
									1.0	.000	.000	-.000
										1.0	.130	.130
											1.0	1.0
												1.0

Symmetric

13-Foot Deployment

*Modes not explicitly identified are membrane modes.

Table 2.1-7. Generalized Mass Matrix for X Modes

(Torsion)

1st Bending	2nd Bending	3rd Bending	4th Bending*
1.0	.024	-.017	-.036
-.074	.030	-.044	-.014
1.0	-.020	.014	.012
-.090	.007	.017	-.004
1.0	-.007	-.017	.012
-.049	-.020	.017	.025
1.0	-.053	.017	.018
-.060	1.0	-.065	-.018
1.0	-.0368	1.0	-.050
1.0	1.0	-.080	-.023
1.0	1.0	1.0	-.042
1.0	1.0	1.0	.039
1.0	1.0	1.0	.075
1.0	1.0	1.0	.086
1.0	1.0	1.0	.091
1.0	1.0	1.0	.032
1.0	1.0	1.0	.086
1.0	1.0	1.0	.021
1.0	1.0	1.0	.368
1.0	1.0	1.0	1.0

Symmetric

26-Foot Deployment

1.0	-.019	.023	.007	-.004	-.005	-.076	-.010	-.012
-.068	-.083	-.044	.007	-.004	-.005	-.076	-.010	-.012
1.0	-.368	.058	.014	-.022	.008	-.006	.075	-.028
1.0	.070	-.001	.017	.008	-.022	-.008	-.027	.007
1.0	1.0	.048	.055	-.009	-.010	-.110	-.005	-.006
1.0	1.0	.368	.073	-.041	.015	-.016	.193	-.007
1.0	1.0	1.0	-.089	-.015	.041	.019	.071	-.192
1.0	1.0	1.0	1.0	-.022	-.027	-.158	.010	.012
1.0	1.0	1.0	1.0	1.0	-.368	-.078	.372	-.137
1.0	1.0	1.0	1.0	1.0	1.0	-.095	-.137	.372
1.0	1.0	1.0	1.0	1.0	1.0	1.0	-.039	-.048
1.0	1.0	1.0	1.0	1.0	1.0	1.0	1.0	-.368
1.0	1.0	1.0	1.0	1.0	1.0	1.0	1.0	1.0

Symmetric

13-Foot Deployment

* Modes not explicitly identified are membrane modes.

Table 2.1-8. Generalized Mass Matrix for Y Modes (In-Plane)

$$\begin{bmatrix} 1.0 & & & & & & & & \\ & -.011 & .009 & -.008 & .013 & & & & \\ & 1.0 & -.002 & .002 & -.004 & & & & \\ & & 1.0 & -.001 & .003 & & & & \\ & & & 1.0 & -.003 & & & & \\ & & & & 1.0 & & & & \\ \text{Symmetric} & & & & & 1.0 & & & \\ & & & & & & 1.0 & & \\ & & & & & & & 1.0 & \end{bmatrix}$$

26-Foot Deployment

$$\begin{bmatrix} 1.0 & & & & & & & & \\ & -.028 & .025 & -.019 & .023 & & & & \\ & 1.0 & -.007 & .005 & .010 & & & & \\ & & 1.0 & -.005 & .001 & & & & \\ & & & 1.0 & -.002 & & & & \\ & & & & 1.0 & & & & \\ \text{Symmetric} & & & & & 1.0 & & & \\ & & & & & & 1.0 & & \\ & & & & & & & 1.0 & \end{bmatrix}$$

13-Foot Deployment

2.2 FABRICATION AND PROCUREMENT

2.2.1 GENERAL

All procurement and fabrication of mechanical, electromechanical, and structural elements of the rollup solar array was completed during this quarter. Detailed descriptions of each of the items discussed in this section are contained in Reference 1 (see Section 6). The rollup solar array mechanical assembly has been completed and installed on the holding fixture, as shown in Figure 2.2-1. Bonding of the array blankets to the storage drums and leading edge member will commence early in the next quarter.

2.2.2 SOLAR PANEL ACTUATOR

2.2.2.1 General

The Bi-Stem solar panel actuator was tested by the vendor for compliance with the procurement specification and subsequently received at GE, Valley Forge. Figure 2.2-2 shows

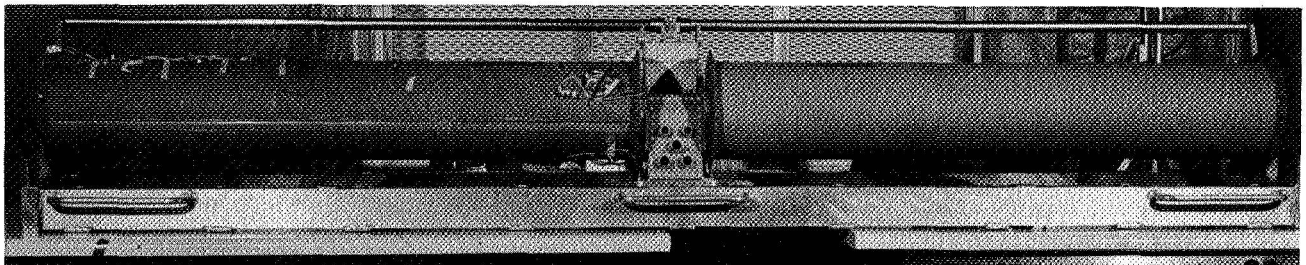
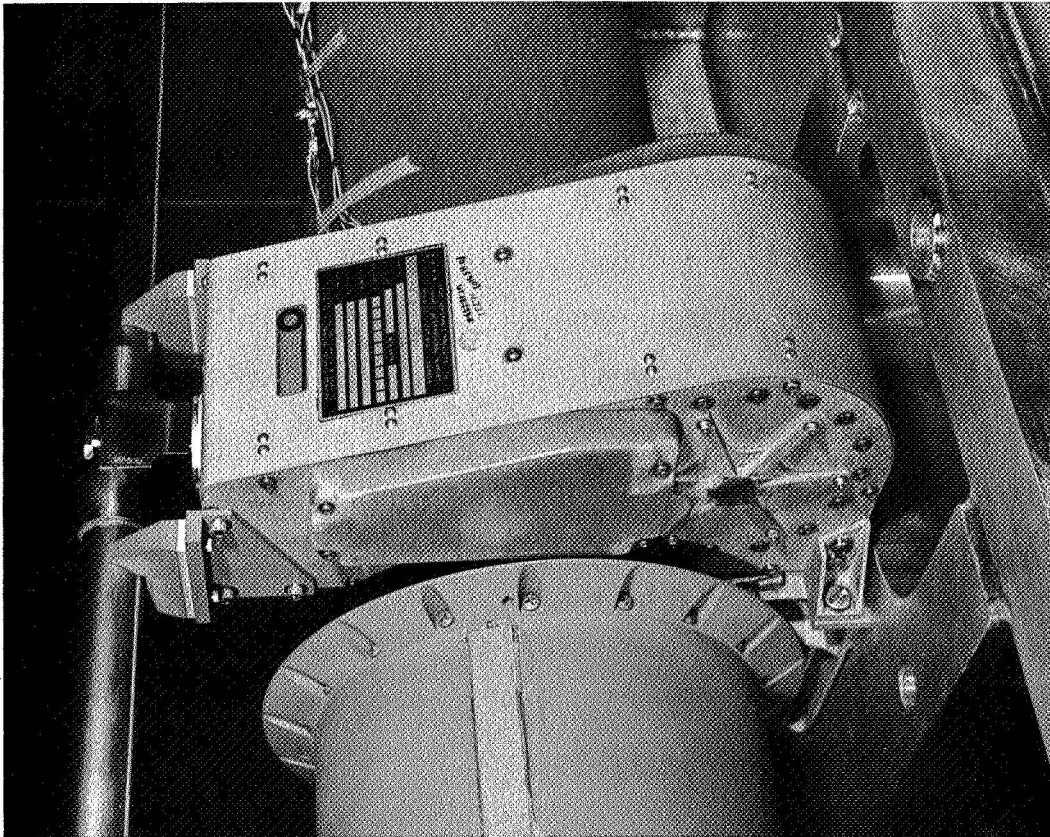
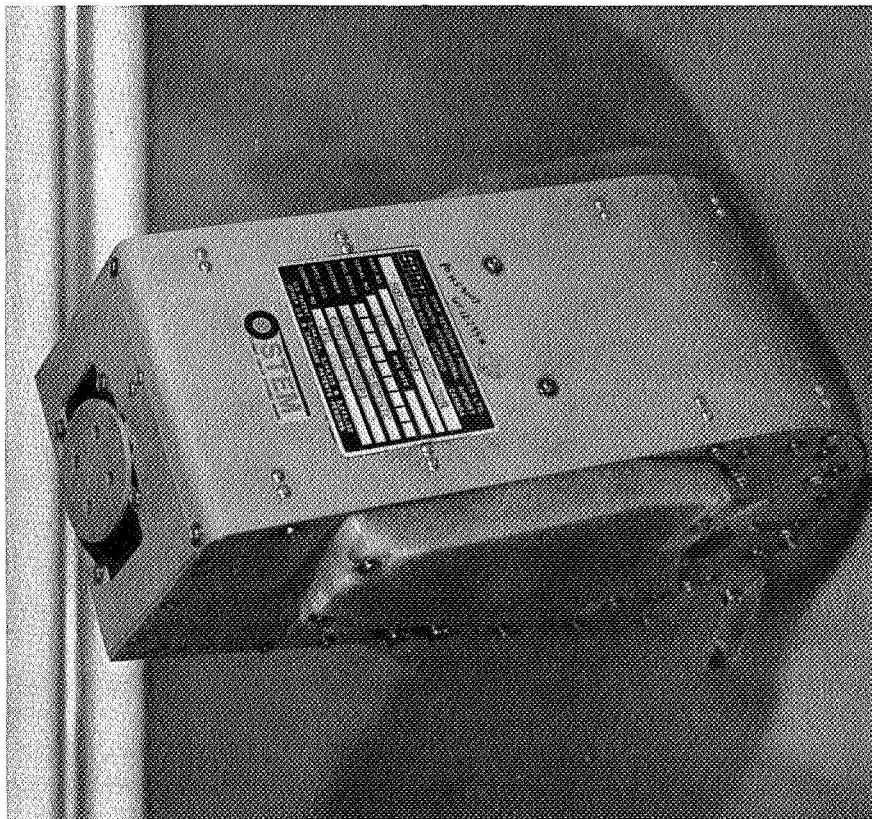


Figure 2.2-1. RA250 Mechanical Assembly (Less Solar Array Blankets)
(VF 70-136 E)



b. Mounted on Center Support
(VF 70 - 136C)



a. Bi-Stem Component
(VF 70 - 136D)

Figure 2.2-2. Solar Panel Actuator

this component in the as-received condition, and in the mounted position on the center support structure.

This RA250 solar panel actuator has been subjected to both random and sinusoidal vibration testing on two occasions. During the first vibration test sequence, the rear motor support bracket failed. This caused problems near the forward mounting bracket which are attributable to the cantilevered effect of the 1-pound motor. The vibration tests pinpointed another highly stressed structural area which was not anticipated by the design analysis. This critical area is at the storage spool/side plate interface. During each vibration test sequence, an approximate 0.020-inch bow was experienced in the side plates and spool shaft bearing housings. This bow has been compensated for in the existing unit by additional shimming. However, for future units, additional analysis/redesign in this area is needed. It should be noted that the actual responses were measured in this area during vibration, and amplifications of approximately four were recorded.

2.2.2.2 Dry Lubricated Motor/Gearhead Problem

The original actuator design used a size 13 motor/gearhead built by Clifton Precision Products Corporation (CPPC) to SPAR Source Control Drawing 5914C1, which called for duroid retainer bearings and no other lubrication. The gearhead consisted of three epicyclic passes in series, consisting of sun and three planet gears mounted on a carrier in each stage. Internal teeth cut in the gearhead housing form a common annulus gear for all three passes. One Vespel SP1 planet gear and two 416 stainless steel planet gears are in each pass. The planet gears rotate on 416 stainless steel studs pressed into the carrier discs. Operating failures were experienced in that a steel planet gear in the third pass (low speed output) seized on its steel spindle stud.

The motor gearhead was replaced with an Airesearch unit that has been used in flight. This unit has a viscous lubricant.

2.2.3 LEADING EDGE MEMBER

Solar Division of International Harvester Company delivered the leading edge member to GE, Valley Forge (see Figure 2.2-3). No problems were encountered with the leading edge

member (LEM) itself at installation onto the RA250 mechanical assembly. However, modifications were required to the saddles/brackets and post which mount to the actuator. These modifications provided adjustment to attain proper alignment of the LEM between the restraining taper plugs on the movable arms. Until the solar array blankets are completely bonded to the drums and testing is started, the leading edge member will be temporarily installed with only one bearing in the tee fitting. This approach will simplify operations requiring removal/installation of the LEM by requiring only removal of a nut and a temporary restraining plate securing the LEM to the post.

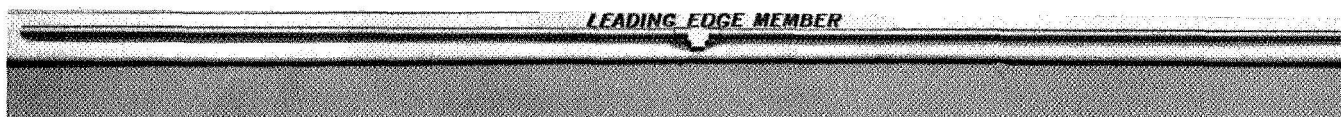


Figure 2.2-3. Leading Edge Member (VF 70-73B)

2.2.4 CENTER SUPPORT

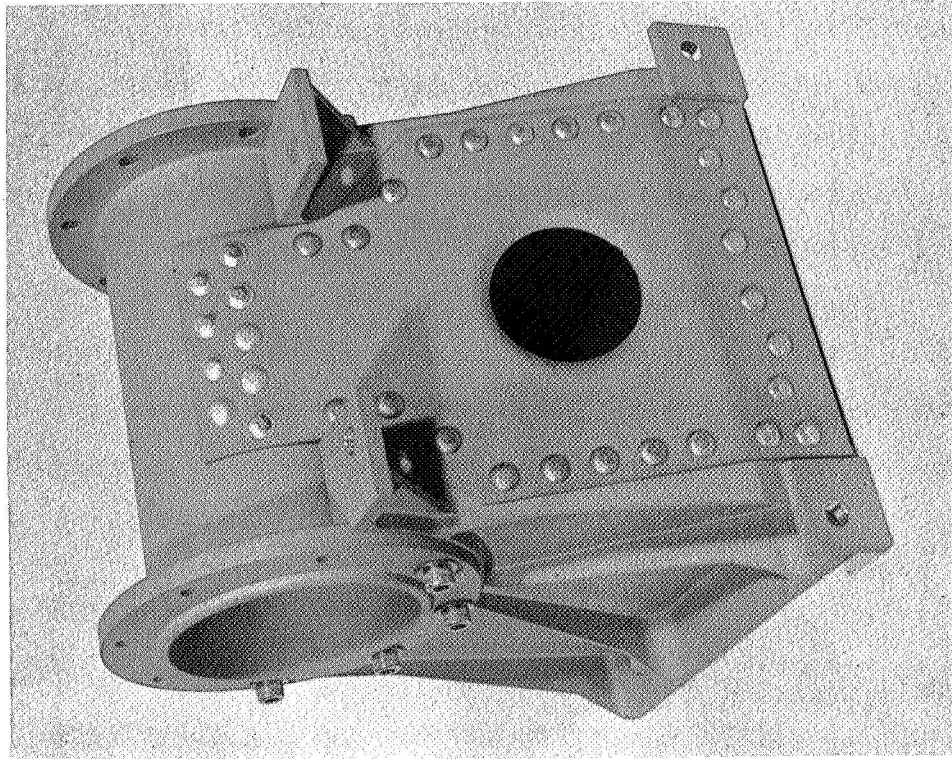
Fabrication and anodizing of the magnesium center support was completed. The required instrumentation was incorporated onto the center support prior to installation into the RA250 mechanical assembly. The only problem encountered during fabrication of the center support was a slight offset of the shaft mounting hole pattern. The offset did not interfere with the mounting bolt installation and subsequent torquing operations.

Figure 2.2-4 shows both the center support component and the installation with both storage drums and Bi-Stem actuator attached. The five connectors carry array power from the slip rings, signals from the thermistors on the blankets, and power to the Bi-Stem.

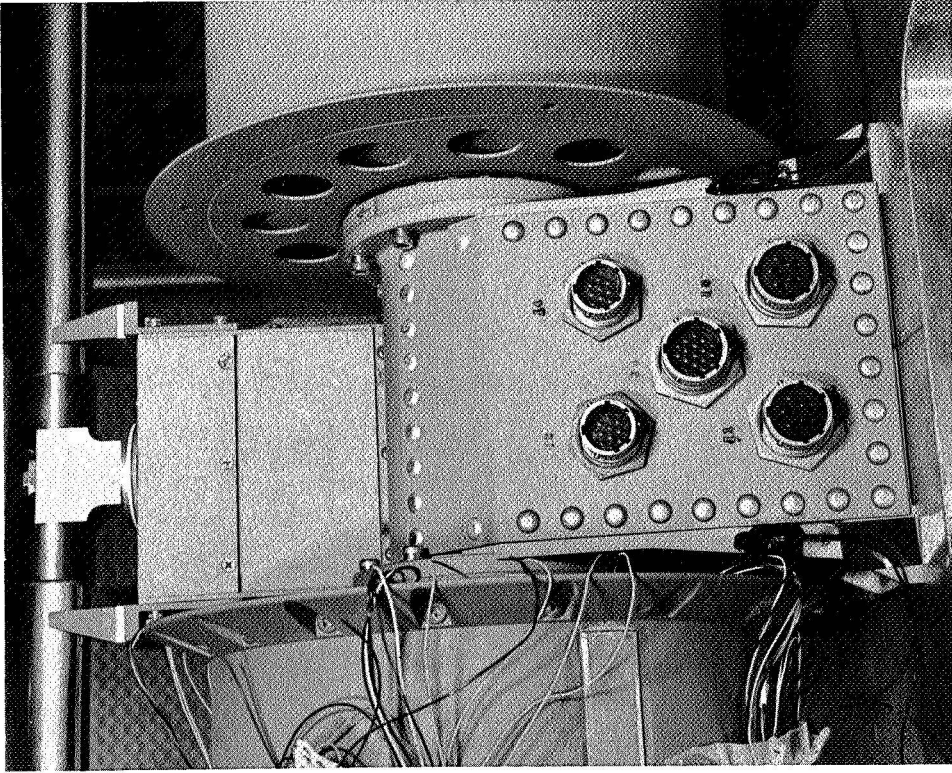
2.2.5 STORAGE DRUMS

2.2.5.1 Magnesium Drum Shells

The drum shells are 47.10-inch long, 0.032-inch thick sheet magnesium rolled into an 8-inch diameter cylinder, which is closed with a lap-butt joint utilizing a 0.75-inch wide



a. Component
(VF 70 - 68)



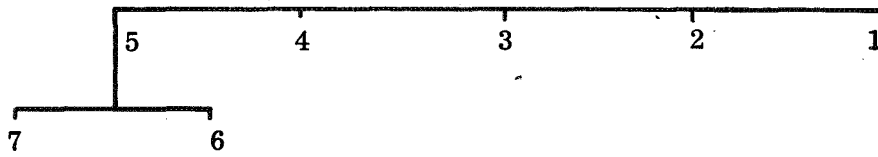
b. Assembly
(VF 70 - 136D)

Figure 2.2-4. Center Support

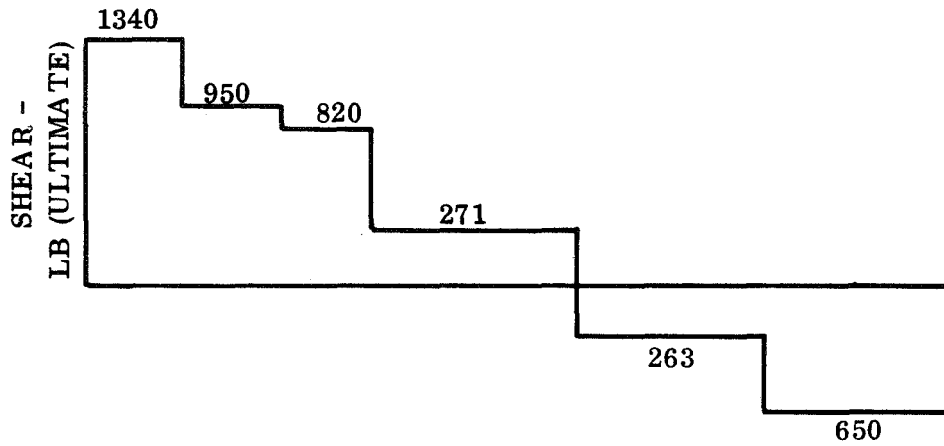
strip of magnesium bonded with Epon 934. Test samples bonded at the same time as the first drum joint resulted in an average shear strength of 915 psi with a low single value among the 5 samples of 819 psi. Based on results for bare aluminum specimens 2000 psi was expected. Inspection of these pull test specimens at the time of the failure showed that it was not the bonding adhesive (Epon 934) that failed but the Dow 17 coating parted from the magnesium base material.

While an analysis to determine the structural adequacy of the existing bonds was in process, test samples from a second bonding operation were pulled. The average lap shear strength on these Dow 17 coated magnesium test samples was 548 psi (with a single value minimum of 476 psi) as compared to 915 psi on the initial set of test samples.

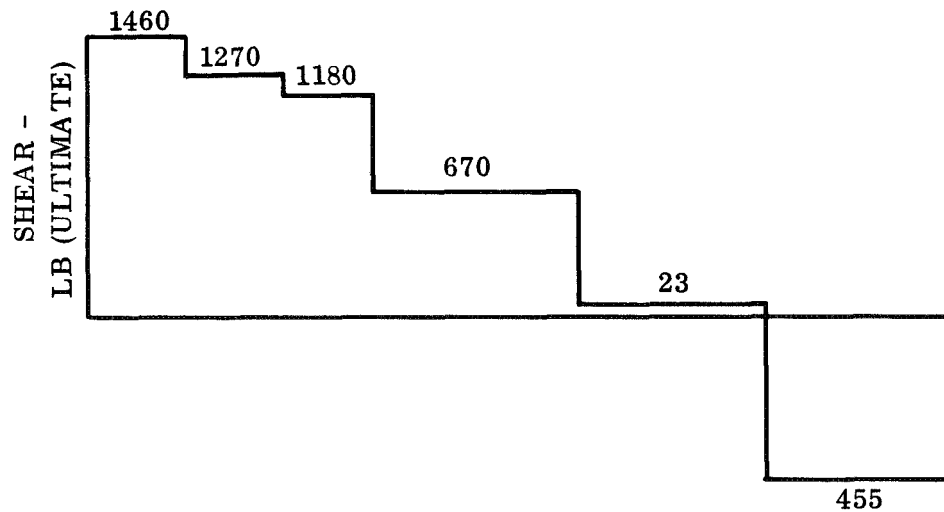
This structural analysis of the drum shells concluded that if the minimum bond shear strength of 476 psi obtained during the coupon testing exists in the splice joint, the bond would be adequate to sustain the design loads and no rework would be required on the splice joint. The resulting shear diagrams are shown in Figure 2.2-5 for two different drum shell configurations. As shown, the loads are somewhat higher in the magnesium drums used for the test unit. Using the 1270 lb, which includes a 1.25 ultimate load factor, and the 476 psi bond shear strength based on the lowest test value, the maximum bond width required is 0.21 inch. From an inspection of the drum shells, actual width is about 0.30 inch. This provides a 43 percent margin for the expected drum loading.



(a) MASS POINT LOCATIONS



(b) SHEAR DIAGRAM FOR BERYLLIUM DRUM LOADING



(c) SHEAR DIAGRAM FOR MAGNESIUM DRUM LOADING

Figure 2.2-5. Shear Diagrams for the RA250 Dynamic Model

2.2.5.2 Inboard End Cap Assembly

Procurement of the bearings, slip ring assembly, and constant torque spring motor was completed. After completion of fabrication and match drilling of the end caps to the drum shells, the inboard end cap assemblies were built up as shown in Figure 2.2-6. During the build up minor rework of the shaft/bearing and shaft/output spool interfaces to obtain proper seating and rotation of the end cap assemblies was required. One end cap assembly has the required instrumentation installed and both end cap assemblies were incorporated into the RA250 mechanical assembly.

2.2.6 OUTBOARD END SUPPORTS

The magnesium weldment movable arm assembly was attached to the hinge bracket with the hinge pin. This partial assembly was aligned with the center support and match drilling was performed on the holding fixture. After installation of the RA250 mechanical assembly onto the holding fixture, the tapered plugs which interface with the outboard end caps and leading edge member were adjusted. The locking pin interfacing with the outboard

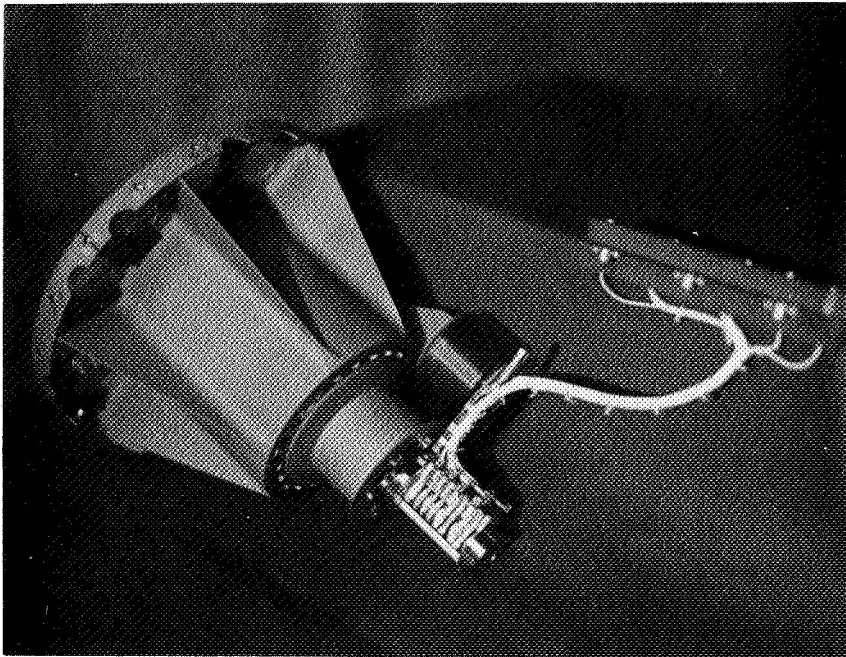


Figure 2.2-6. Inboard End Cap Assembly

end cap assembly was adjusted also for proper engagement. Experience during assembly of the outboard end supports led to the addition of restraining features in the hinge pins and LEM taper plugs so that proper seating and subsequent torqueing could be more easily accomplished. To facilitate subsequent operations prior to start of the test program, the bolt catcher remains uninstalled and the bolt into the separation nut is only installed finger tight.

Figure 2.2-7 shows the output end support as installed on the mechanical assembly.

2.2.7 SLIP RING ASSEMBLY

The slip ring assemblies designed and developed by Poly-Scientific Division of Litton Precision Products, Inc. were delivered to GE, Valley Forge (see Figure 2.2-8). Since receipt, the slip ring assemblies have been incorporated into the RA250 mechanical assembly. No problems have been encountered with these assemblies.

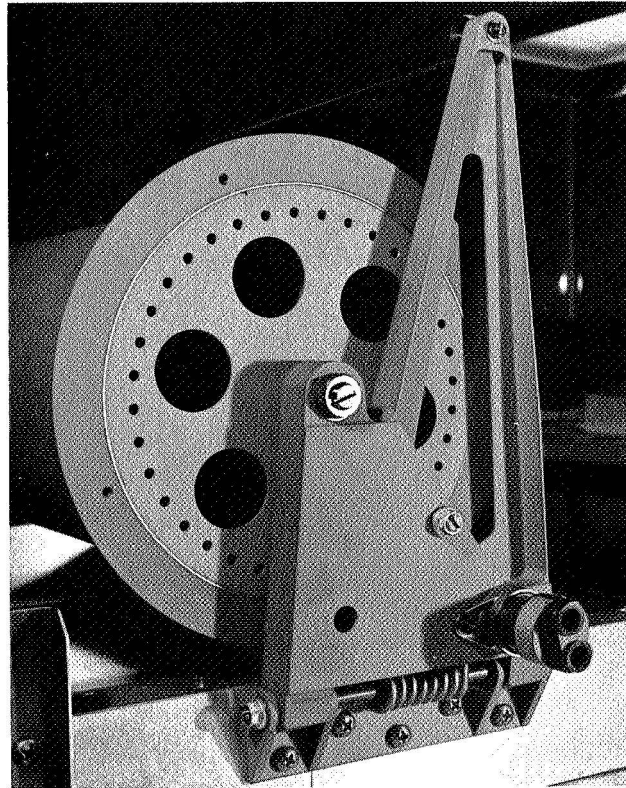


Figure 2.2-7. Outboard End Support (VF 70-136B)

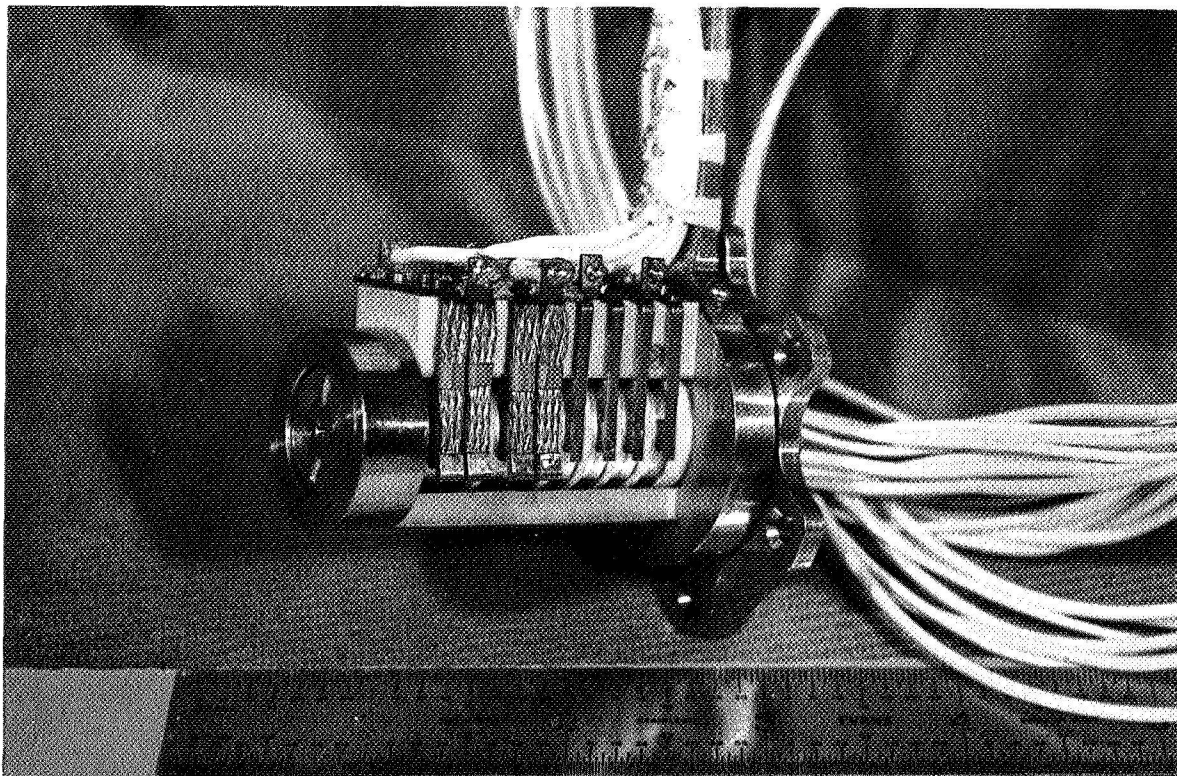


Figure 2.2-8. Slip Ring Assembly (VF 70-73I)

2.2.8 ARRAY BLANKET

During this report period, the installation of all modules (both dummy and active) was completed on both array blankets. This basic installation procedure was changed from the initial approach as described in Reference 2. To remove the majority of the inherent wrinkles in the substrate material (Kapton H film with etched copper bus strips), the sheet was stretched in the longitudinal direction on a 35-ft long horizontal table as shown in Figure 2.2-9. A tension of approximately 150 lb was applied at each end. This procedure resulted in marked improvements in the number and size of adhesive voids between the modules and the substrate. With each substrate in this stretched condition, each module is placed on the substrate as shown in Figure 2.2-10. The adhesive (SMRD 745) is cured by heating blankets which are placed on top of weighting plates over each module.

Figure 2.2-11 shows an overall view of each completed blanket as stretched on the same long table. Close-up photographs of each active module on both of these blankets are shown

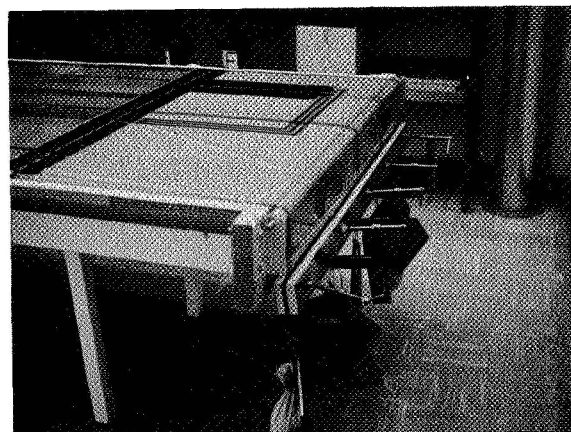
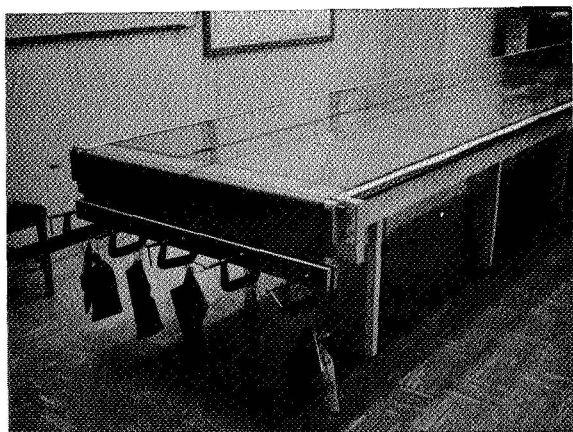
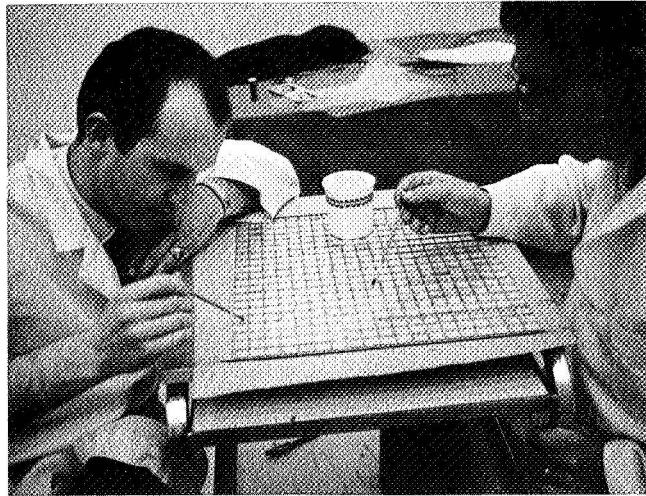
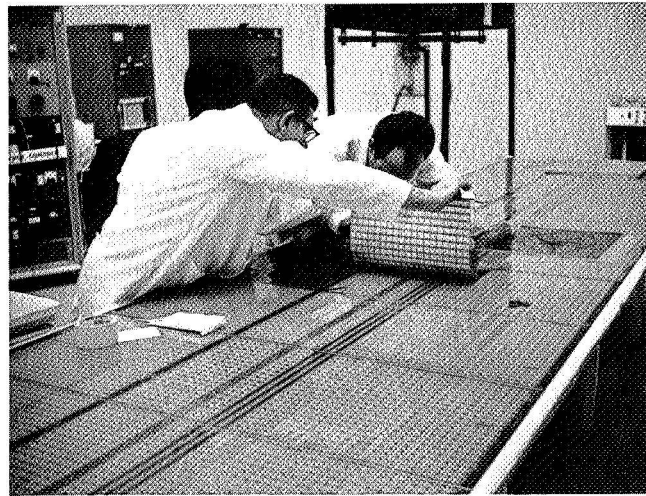


Figure 2.2-9. Substrate Stretching Setup

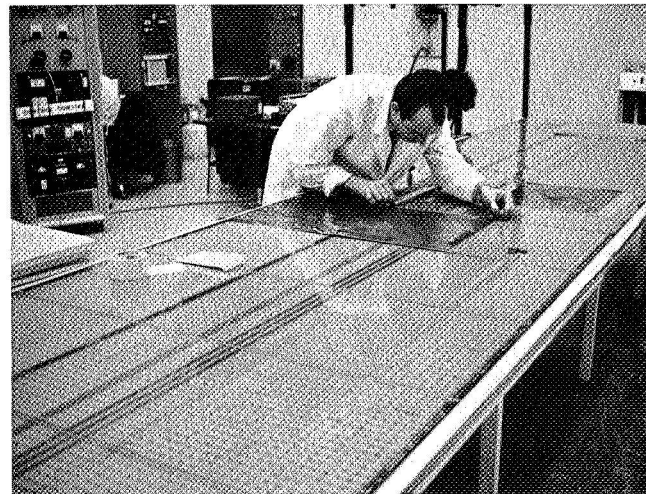
in Figures 2.2-12 through 2.2-16. The tabs projecting beyond the edge of the blankets are thermocouple leads. There are two thermocouples installed under each module between the cells and the substrate.



a.

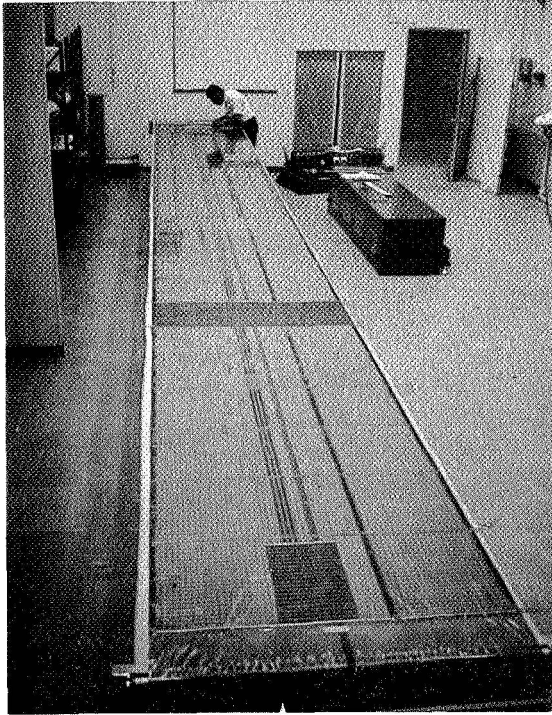


b.

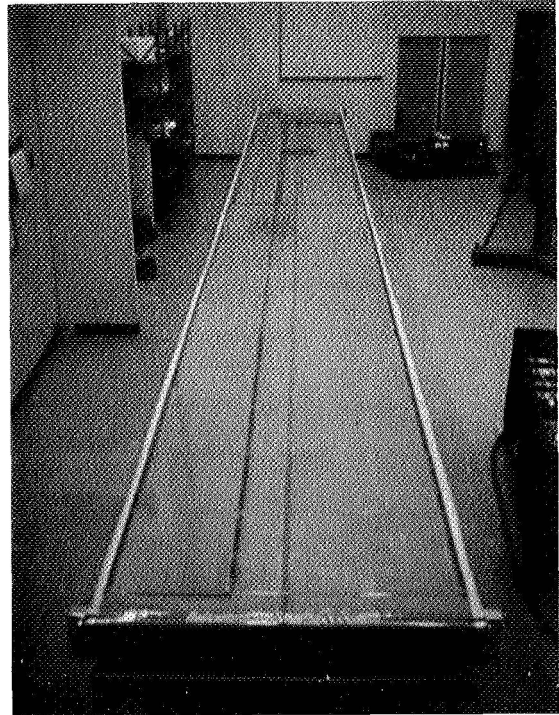


c.

Figure 2.2-10. Installation of Active Solar Array Modules



a. G1 Assembly



b. G2 Assembly

Figure 2.2-11. Array Blankets

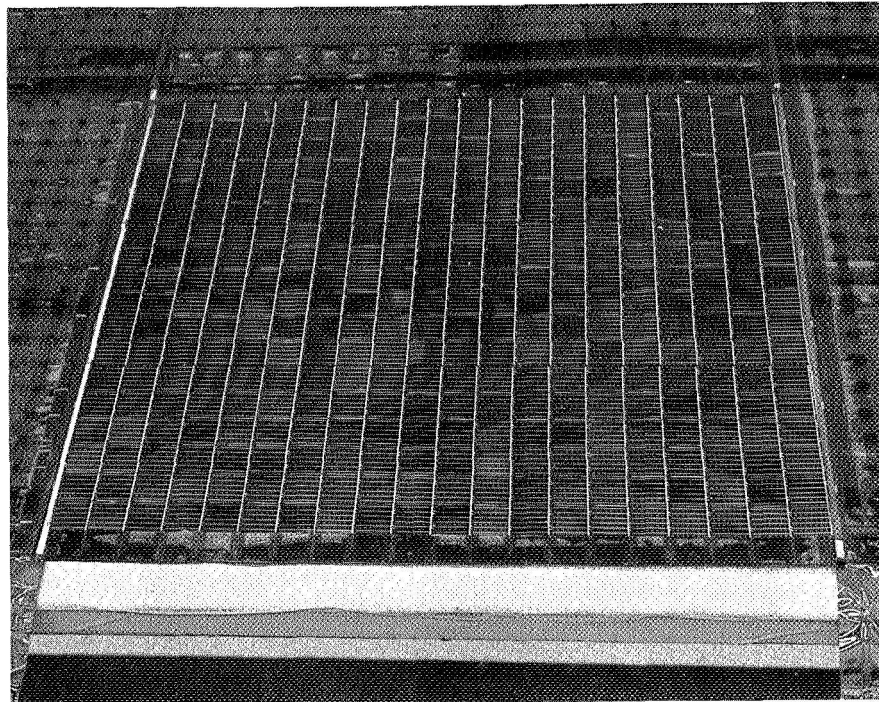


Figure 2.2-12. EOS Module Mounted on G1 Blanket Assembly (VF 70-127B)

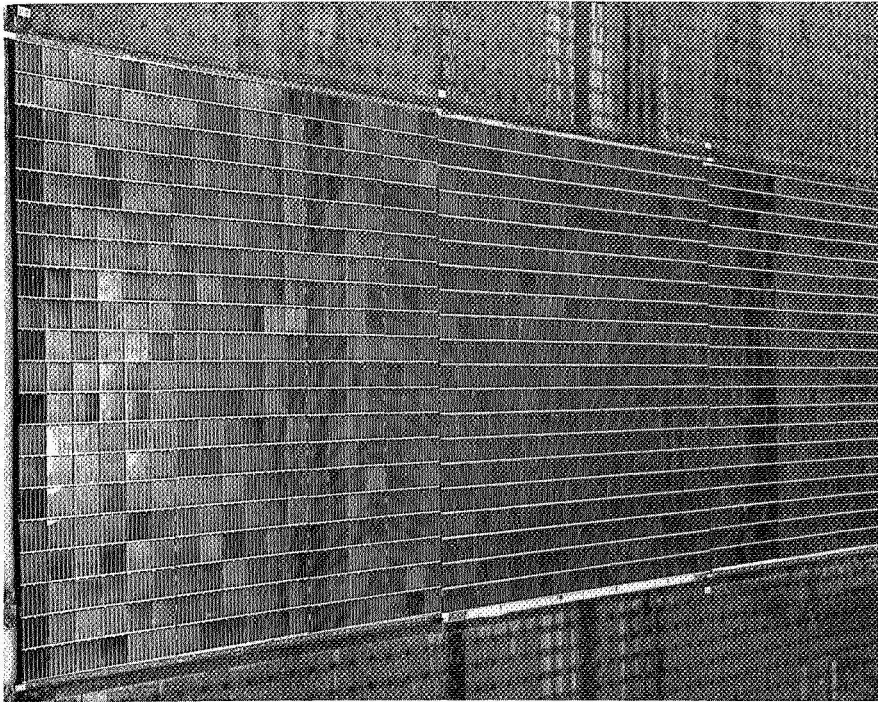


Figure 2.2-13. Heliotek (near), GE No. 2 (middle), and Boeing (far) Modules Mounted on G1 Blanket Assembly (VF 70-127E)



Figure 2.2-14. Spectrolab Module Mounted on G1 Blanket Assembly (VF 70-127D)

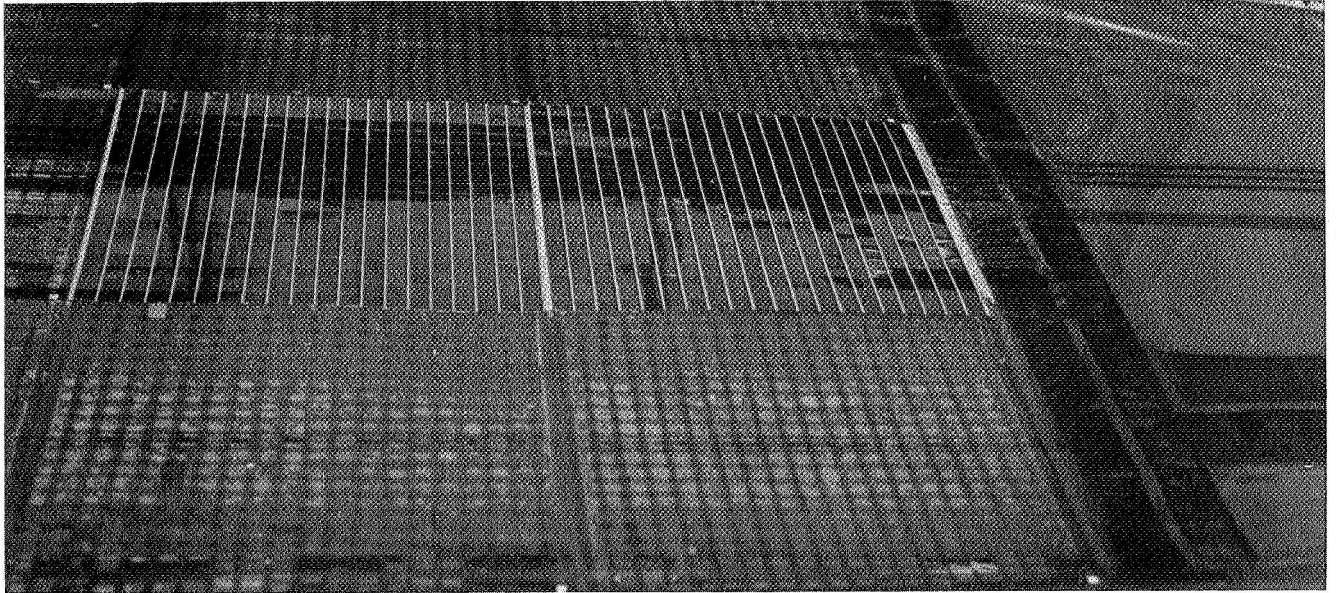


Figure 2.2-15. GE No. 1 (left) and Centralab No. 1 (right)
Modules Mounted on G1 Blanket Assembly (VF 70-127C)

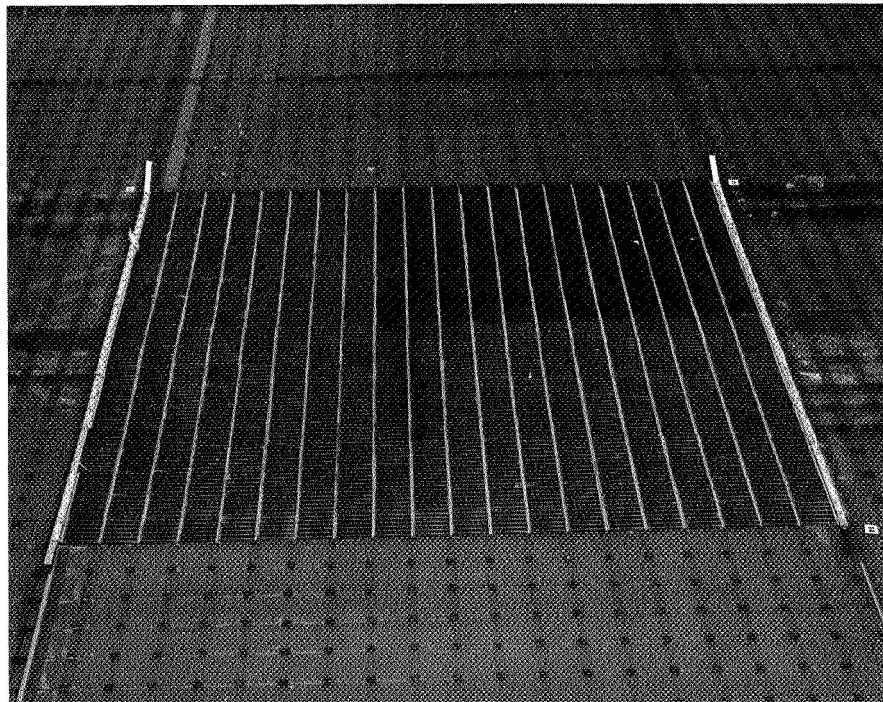


Figure 2.2-16. GE No. 3 Module Mounted on G2 Blanket Assembly (VF 70-136A)

2.3 DEVELOPMENT TESTING

2.3.1 BI-STEM THERMAL BENDING TEST

2.3.1.1 Background

NASA/GSFC has completed tests on the silver plated Bi-Stem specimens provided by General Electric for thermal bending tests. The thermal vacuum chamber utilized in investigating boom thermal bending behavior consists essentially of a vertical cylinder approximately 1 foot in diameter and 13 feet high, incorporating a liquid N₂ shroud, and solar simulation that provides an intensity equivalent to one solar constant over the full length of a 10 foot boom surface with an intensity uniformity of better than +5 percent. The facility is shown in Figure 2.3-1.

In addition, the facility employs a high-speed, low backstreaming pumping system and provision for rotating the suspended test specimen over a range of angular velocities. The degree of bending and thermal excitation can be recorded photographically as well as by optical means. Samples were removed from the test specimen for measurement of solar absorptance necessary to correct the observed bending which resulted from essentially an IR source. Peripheral temperature distribution, time constants relating to heat conductions around the perimeter, and heat flow from the solar source to boom and shroud were recorded.

Over the past 2 years, NASA/GSFC has employed this facility in the development of a technique for measurement of gravity

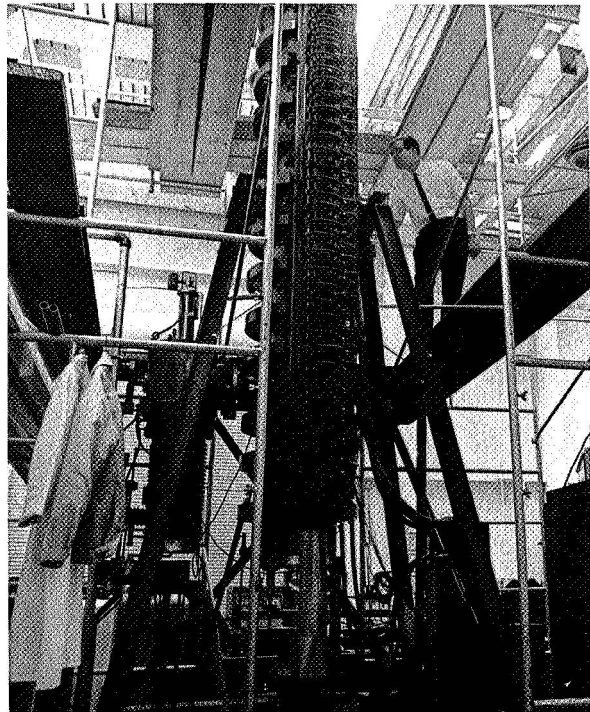


Figure 2.3-1. Thermal Bending Test Setup (NASA G-69-4536)

gradient rod deflections under the influence of solar heating. The RA250 Bi-Stem is one of many boom configurations tested by NASA/GSFC. For comparison bending behavior twist and thermal instability for each type tested are related to the basic spar overlapped Stem and a seamless thin wall boom as an indication of the improvement in performance, if any, that is observed.

Test results were provided for use in this program and are included in this report. Eventually, NASA/GSFC will issue a complete official report on the entire boom thermal test program including the RA250, 1.34-inch diameter Bi-Stem.

2.3.1.2 Test Results Discussion

The information supplied by NASA/GSFC was in the form of plots depicting in-plane and out-of-plane bending relative to a fixed sun. The test specimen bending at each 30 degrees of boom rotation relative to the fixed sun was plotted.

Two tests were conducted on the silver plated Bi-Stem. The first test allowed unrestrained relative motion between the Bi-Stem elements, while the second test eliminated relative motion between the two elements at the tip. The test restraining the relative element motion was accomplished by welding the tip end of the boom over the entire overlap area. This basically represents the condition existing in the RA250 solar panel actuator when the tip plug is attached to both elements.

The actual Bi-Stem tests took about 10 times longer to complete than other boom tests conducted by NASA/GSFC. Most of the other booms tested during the program were 0.5 inch in diameter and 0.002 inch thick. Apparently, the main reasons for the increased test time were relative motion (rotation) between the two Bi-Stem elements and thermal gradients. The relative motion of the elements with respect to each other was suspected as the reason for a rotation noted when the sun was turned on and off.

Basically, the measured tip deflections were repeatable, especially for the non-welded configuration, although some slight variations were noted with the welded specimen when selective points were checked. When the tip deflection patterns for the non-welded and welded tests were drawn as a smoothed curve for a rotating sun/ fixed boom and for a rotating boom/ fixed sun, they did not reflect what was expected from the temperature profile analysis provided prior to the test (Section 2.3.12 of Reference 2). Idealized patterns symmetrical about the rod axes, similar to those experienced on 0.5-inch diameter Bi-Stems, were anticipated. However, the RA250, 1.34-inch diameter Bi-Stem idealized tip deflection patterns were offset, skewed or nonsymmetrical to the rod axes. Representative idealized tip deflections for both the 0.5- and 1.34-inch diameter Bi-Stems with a rotating sun/ fixed boom and rotating boom/ fixed sun are shown in Figure 2.3-2.

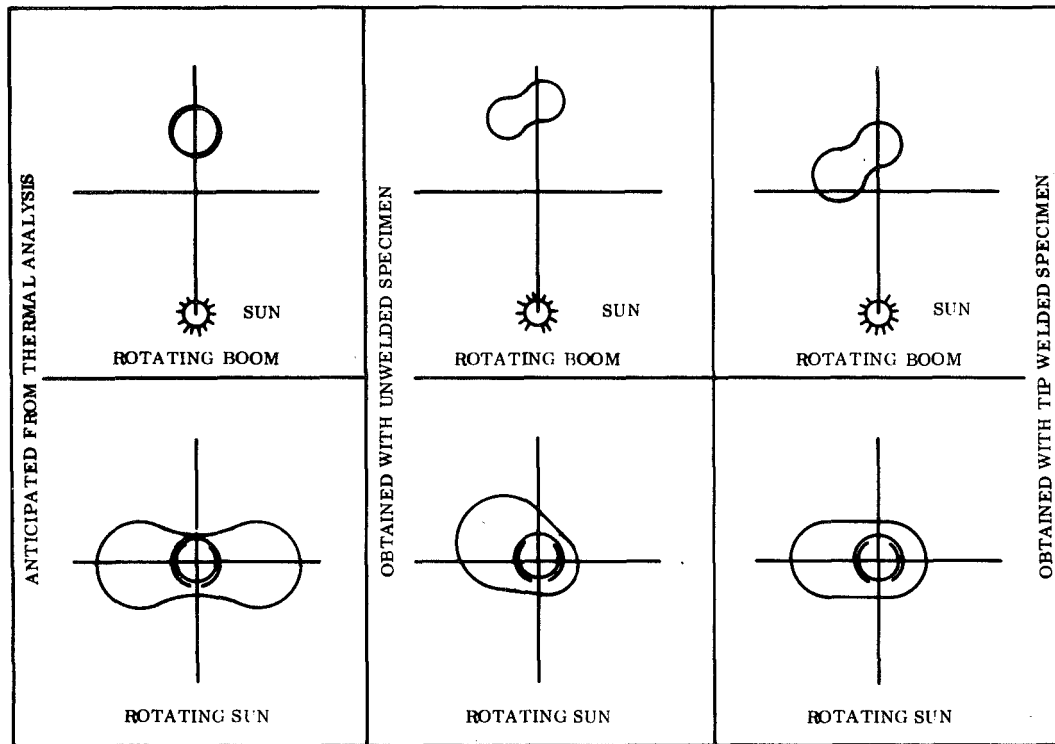


Figure 2.3-2. Idealized Tip Deflection Patterns

Inspection of Figure 2.3-3 reveals that in position 2 (300-degree boom rotation), the welded test specimen exhibited a negative bending toward the sun. This condition is generally considered to be unstable and could result in thermal "flutter". The amount that the welding

technique contributed to this negative bending is unknown at this time. After welding it was noted the outer element was displaced along its edges from the inner element at some points.

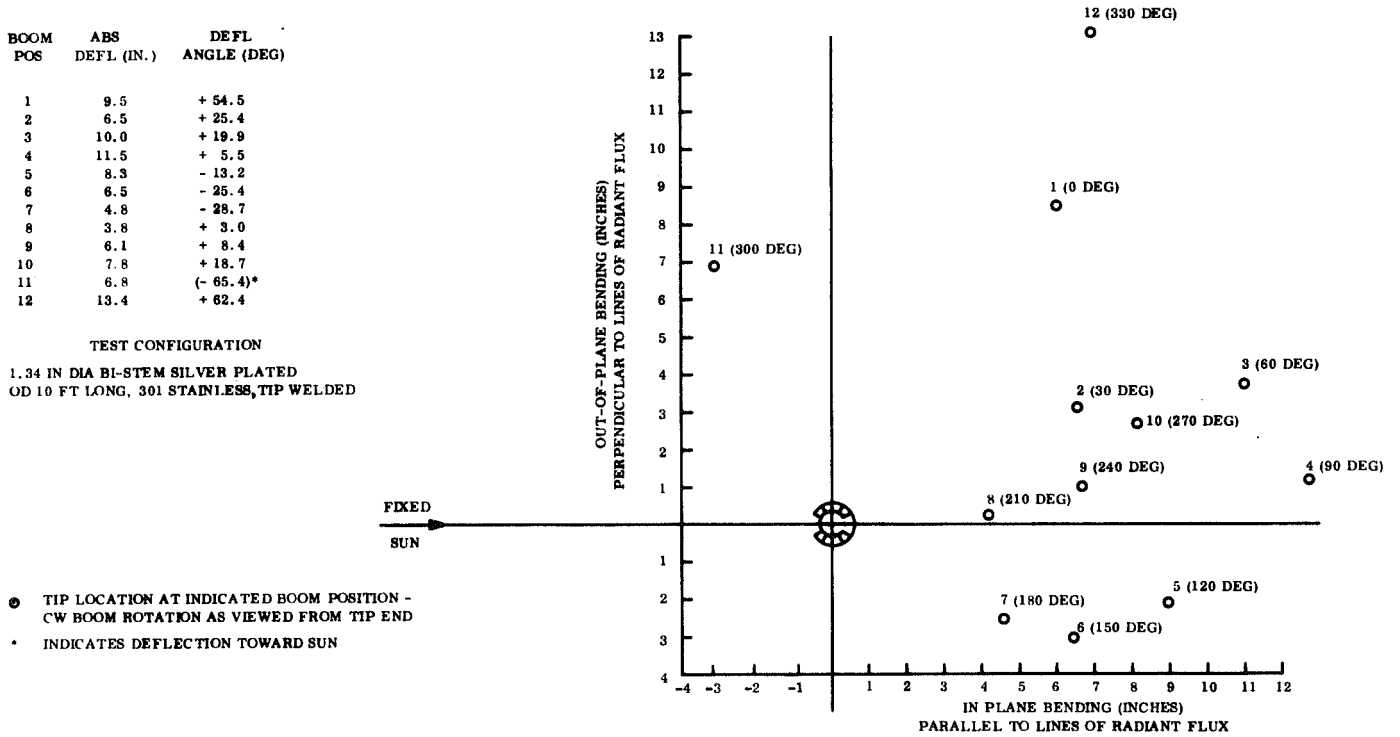


Figure 2.3-3. Extrapolated Absolute Zero-g Thermal Bending at 33.5 Ft²

2.3.1.3 Extrapolation Derivation

Utilizing the measured deflection and absorptivity data it was necessary to separate the deflection due to 1 G and 1 sun (140 mw/cm²). The following formula was utilized to determine this deflection.

$$\delta_{11} 0'G + 1 \text{ sun} = \left(\frac{k_g}{k_{IR}} \right) \delta_{MEAS} = 1.698 \delta_{MEAS}$$

where

$$k_{\text{IR}} = \frac{\alpha_{\text{IR}}}{\alpha_{\text{sun}}} = 0.596$$

with

$$\alpha_{\text{IR}} = 0.106$$

and

$$\alpha_{\text{sun}} = 0.178$$

and

$$k_g = 1 + \frac{WL^3}{7.66 EI_{11}} = 1.0109$$

with

$$W = 16 \text{ lb/in.}$$

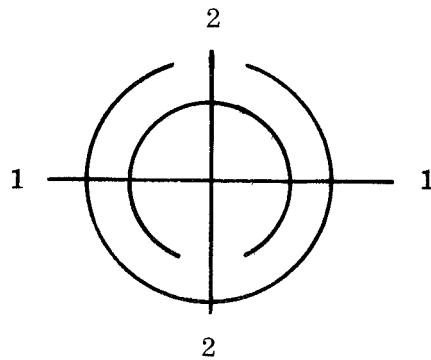
$$L = 120 \text{ in.}$$

$$EI_{11} = 332 \times 10^3 \text{ lb-in.}^2$$

The moment of inertia has two different values for the axes of symmetry in the test specimen utilized. These are:

$$I_{11} = 1.185 \times 10^{-2} \text{ in.}^4$$

$$I_{22} = 1.321 \times 10^{-2} \text{ in.}^4$$



As the rod is rotated in the flux field, the moments of inertia most affecting the amount of bending vary from position to position. At any position other than 0, 90, 180 or 270 degrees, the rod principal axes are not aligned with the deflection components measured. Therefore, the moments of inertia should be resolved into the measurement axes and the components then combined into the absolute value of deflection and its direction. Due to the preliminary nature of the data received, the moment of inertia giving the largest factor k_g was utilized throughout the calculations. This would result in larger than actual absolute deflections. As a consequence, the data presented herein should be considered as an approximation and not an exact representation of extrapolated thermal deflections from actual measurements taken during test.

An approximation of the actual radius of rod curvature due to thermal bending may be represented by:

$$R_{ACT} \approx \frac{L^2}{2\delta}$$

For extrapolation purposed to the 33.5-foot length utilized in the RA250 solar panel actuator, the deflection was represented by:

$$(\delta)(33.5) \approx (18.9)(\delta_{MEAS})$$

This was derived from the following:

1. A 10-Foot Test Specimen

$$R_{ACT} \approx \frac{L^2}{2 \delta_{10'G + 1 \text{ sun}}} \approx \frac{0.72 \times 10^4}{\delta_{10'G + 1 \text{ sun}}}$$

2. A 33.5-Foot Extrapolated Rod

$$\delta_{\text{EXT}} \approx \frac{L^2}{2 R_{\text{ACT}}} \approx 11.11 \delta_{\text{"0"G + 1 sun}}$$

Where

$$\delta_{\text{"0"G + 1 sun}} = 1.698 \delta_{\text{MEAS}}$$

References 4 and 5 were utilized in deriving the above mentioned formulas. The extrapolated deflections calculated from these formulas were then converted to absolute deflections using the trigonometric relationship:

$$\delta_{\text{ABS}} = \sqrt{\delta_{\text{IP}}^2 + \delta_{\text{OP}}^2}$$

Their angles of deflections from the flux field were determined from the relationship:

$$\theta = \tan^{-1} \frac{\delta_{\text{OP}}}{\delta_{\text{IP}}}$$

2.3.1.4 Discussion of Results

Figure 2.3-4 shows the extrapolated absolute value of the zero-g thermal bending for a 33.5-foot overlapped Bi-Stem, and Figure 2.3-3 shows the extrapolated absolute value of the zero-g thermal bending for a 33.5-foot Bi-Stem with the tip end welded. Both of these figures were derived from plots of actual deflection measurement, supplied by NASA/GSFC. In addition to the plots, NASA/GSFC supplied the solar and lamp absorptivities utilized in the derived formulas of Section 2.3.1.3.

When the maximum absolute value of the zero-g thermal deflections indicated on Figure 2.3-3 and 2.3-4 are added to the Bi-Stem vertically deployed tip deflections measured during SPAR actuator acceptance tests, the following apparent maximum total tip deflections occur:

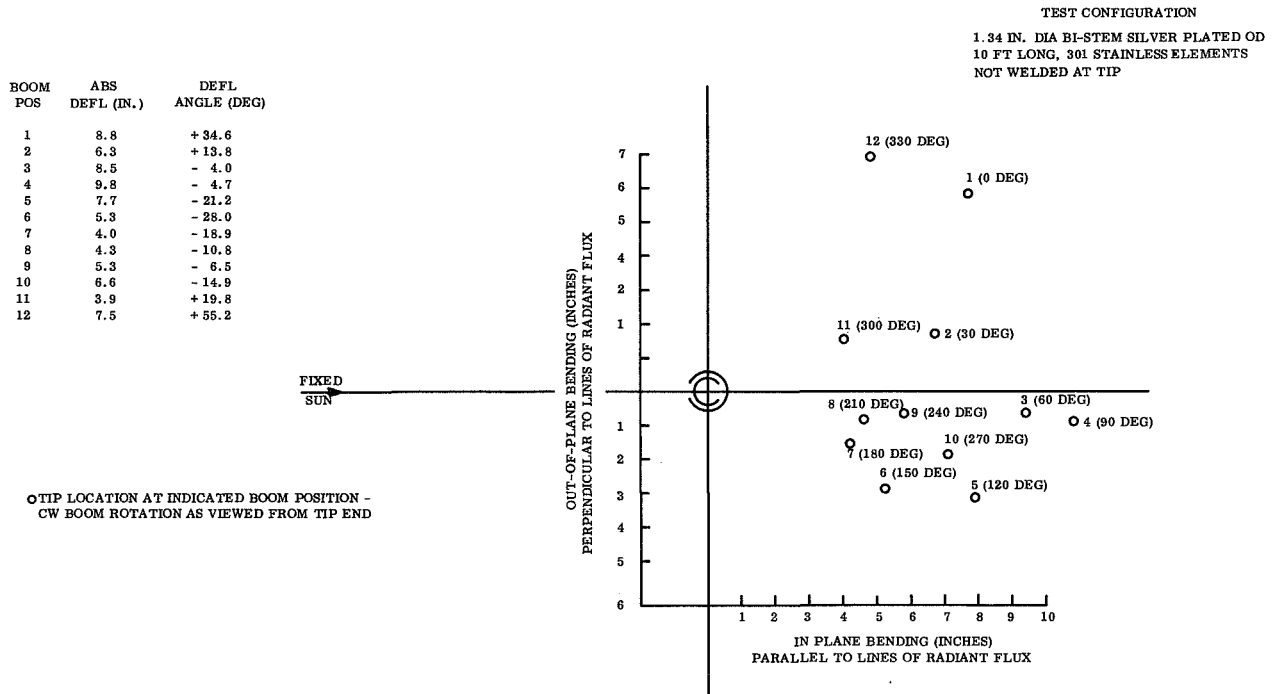


Figure 2. 3-4. Extrapolated Absolute Zero-g Thermal Bending at 33.5 Ft

	<u>Overlapped (in.)</u>	<u>Tip Welded (in.)</u>
Boom deflection for vertical deployment	8.0	8.0
Deflection due to 5.2 lb. load	11.0	11.0
Absolute thermal deflection (maximum)	<u>9.8</u>	<u>13.4</u>
Maximum Total Apparent Deflection	28.8	32.4

Analysis of the rod deployed condition contained in Section 4.3 of Reference 6 indicated that with a temperature gradient of 53.9^oF, a blanket tension of 4.0 pounds, and a solar illumination at 260 mw/cm² intensity (1.5 suns), a rod tip deflection of 35.68 inches could be expected. The maximum total apparent deflections above for either boom condition do not exceed the predicted deflections.

Considering the approximate nature of the extrapolated data, as well as the vertical deployed measurements, a more realistic apparent total deflection could be obtained by

combining deflections obtained with the sun orientation for the solar array. This position of the boom during the testing was position 7 (180 degrees) on Figures 2.3-3 and 2.3-4, observed thermal bending was in the same general direction as the bending due to loading in the deployment test.

The thermal analysis supplied to NASA/GSFC and shown in Section 2.3.1.2 of Reference 2 indicates a temperature gradient of 17°F for a solar illumination of 140 mw/cm² for this boom position. Position 7 (180°) with respect to the sun is shown in the following illustration.

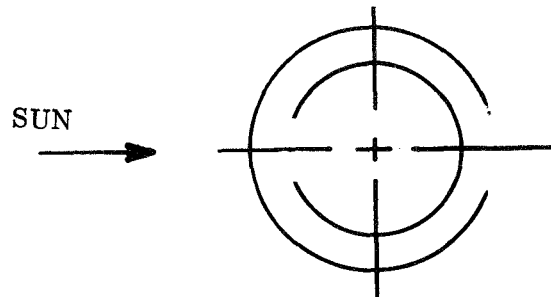


Table 2.3-1 shows the total apparent deflection for the sun position that will occur in the rollup solar array.

Table 2.3-1. Comparison of Analyses with Total Tip Deflection

	<u>Non-welded</u>	<u>Welded</u>
ΔT_{MAX} (°F)	17	17
Solar flux (mw/cm ²)	140	140
Tip mass (lb)	1.2	1.2
Blanket tension (lb)	4.0	4.0
<u>Deflections (in.)</u>		
No load	8.0	8.0
Full load	11.0	11.0
Abs thermal	4.0	4.2
<u>Position 7 Total</u>		
Apparent deflection	23.0	23.2

2.3.2 MODULE THERMAL CYCLING TEST

Three sample solar cell modules (two 4 x 4 and one 5 x 7) have been thermally cycled 34 times between -200°F and $+285^{\circ}\text{F}$. These modules were fabricated utilizing the JPL furnished solar cells and coverglass. The cells were interconnected with silver expanded metal per drawing number 47C218187. The three modules were bonded to a Kapton substrate with SMRD-745. The rear side of the substrate had cushioning buttons installed as on the prototype blanket. A copper strip was also etched on the rear of the substrate to simulate the bus strip network. This copper strip was insulated with 1-mil Kapton silicone pressure sensitive tape, as on the prototype blanket.

Figure 2.3-5 shows the three modules mounted on the common substrate suspended in front of an array of Quartzline lamps which provided the heat input in the vacuum chamber. In addition to this active module substrate, a module of dummy glass platelets was placed in the same test so that the thermal cycling effects on the dummy glass modules could be determined.

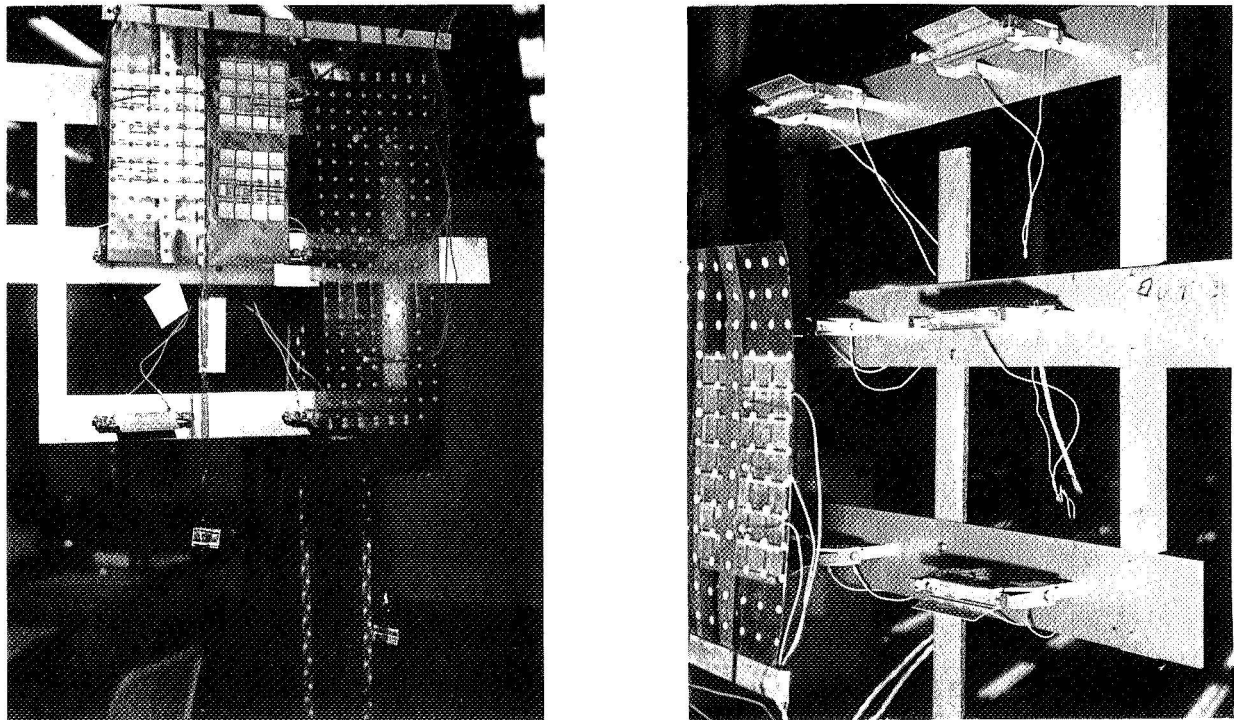


Figure 2.3-5. Thermal Cycling Module Test Setup

Figure 2.3-6 shows a typical active module temperature profile during one 50-minute cycle.

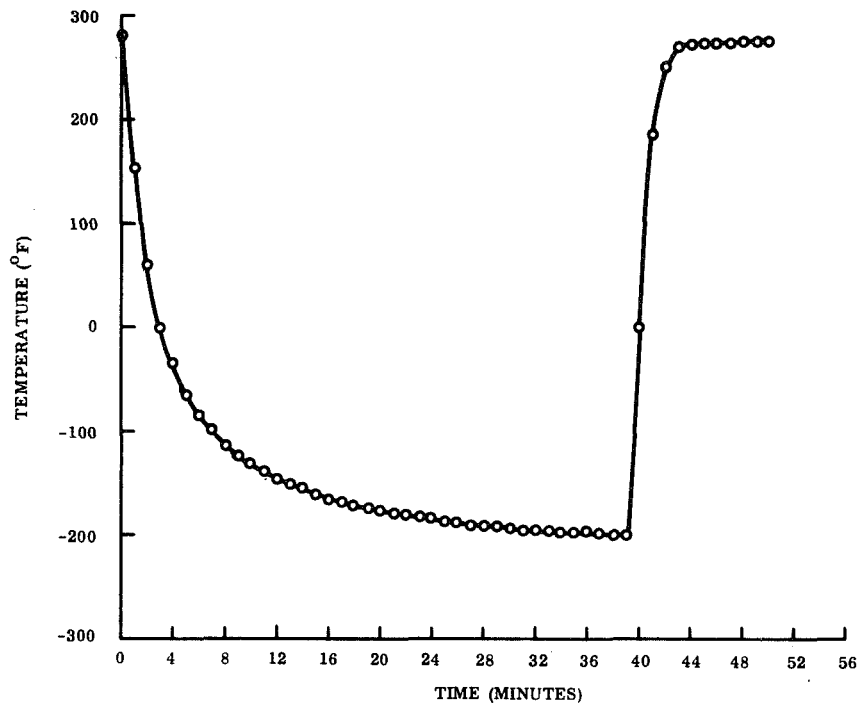


Figure 2.3-6. Typical Active Module Temperature Profile

A detailed visual examination of the solar cell modules revealed a failure mode which could be attributed to this thermal cycling test. This failure mode is the fracture of the expanded metal stands in localized areas. This type of failure occurred only in areas where the interconnect loop had been deformed (or scored) by the mesh forming tool. An example of this loop scoring is shown in Figure 2.3-7. The cause of this deformation was corrected by rework of the forming tool and subsequent 100 percent visual inspection of each strand after forming.

2.3.3 ARRAY STRUCTURE LOAD DEFLECTION TEST

2.3.3.1 Scope

This test report covers load-deflection testing of the drums and end supports of the RA250 solar array, stowed configuration.

2.3.3.2 Test Summary

The drum and end supports of the RA250 solar array were subjected to a series of load deflection tests (see Figure 2.3-8).

The objectives of these tests were:

1. To measure deflections on the extremities of the stowed configuration drums (with the end supports unattached) under controlled loading conditions and to obtain data from which bearing assembly flexibility coefficients can be obtained.
2. To measure deflections on the unattached end support under controlled loading conditions, and to obtain data from which its flexibility influence coefficients can be obtained.

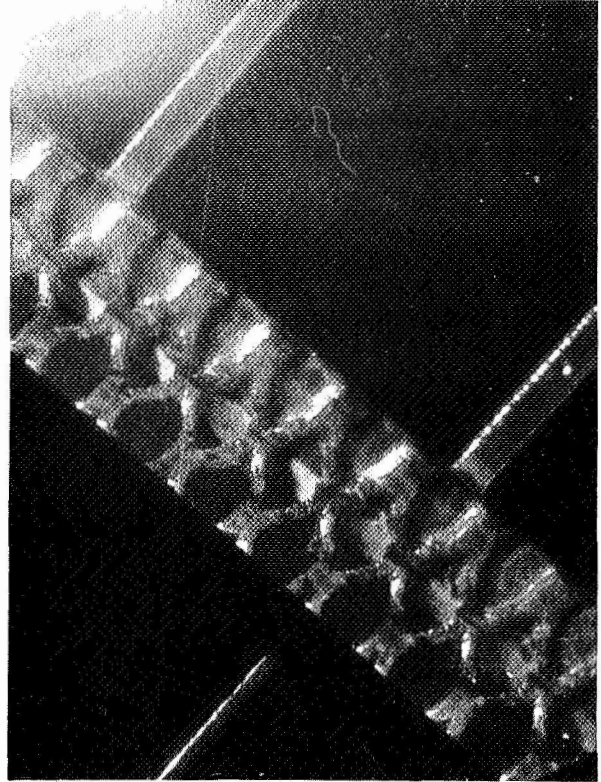
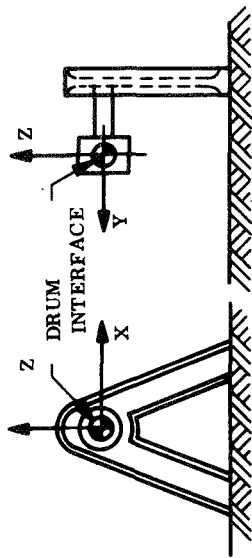


Figure 2.3-7. Example of Deformed Expanded Metal Interconnect Loop

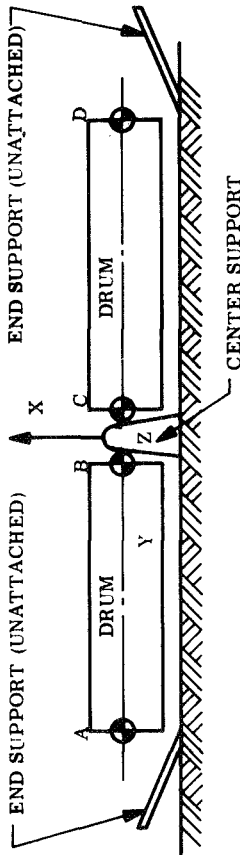
These experimental flexibility influence coefficients will be converted to stiffness coefficients suitable for usage in revised stowed configuration structural dynamic analyses.

These objectives were attained. In addition, other significant data was also acquired during the test:

1. The drums exhibited very little, if any, indications of bearing assembly-induced chatter, or "free-play".
2. A flexibility coefficient for the center support was also obtained from data measured during the test.
3. The drum and bearing assembly possesses a relatively high level of longitudinal (Y-axis) stiffness, i. e., it could not be measured by the test techniques employed.



(b) END SUPPORT TEST GEOMETRY (SIMPLIFIED)



(a) DRUM DEFLECTION TEST GEOMETRY

NOTE: A BULLSEYE ● DENOTES A POINT OF LOAD APPLICATION AND/OR DEFLECTION MEASUREMENT; THE CAPITAL LETTER, I.E., B, ADJACENT TO IT IDENTIFIES THE POINT.

TEST NO.	RUN NO.	TEST DESCRIPTION	LOADING AND DEFLECTION DATA		
			TEST AXIS	LOADING DESCRIPTION APPLIED AT	DEFLECTIONS MEASURED AT
1	a	Loads @ Drums - Outboard	X	Symmetrical	A, D
1	b	Loads @ Drums - Inboard	X	Symmetrical	B, C
2	a	Loads @ Drums - Outboard	X	Antisymmetrical	A, D
2	b	Loads @ Drums - Outboard	X	Antisymmetrical	B, C
3	a	Loads @ Drums - Outboard	Z	Symmetrical	A, D
3	b	Loads @ Drums - Inboard	Z	Symmetrical	B, C
4	a	Loads @ Drums - Outboard	Z	Antisymmetrical	A, D
4	b	Loads @ Drums - Inboard	Z	Antisymmetrical	B, C
5	a	Loads @ Drums - Outboard	Y	Symmetrical	A, D
6	a	Loads @ Drums - Inboard	Y	Antisymmetrical	A, D
7	a	End Support Deflection	-	Z-Force	At Drum Interface
7	b	End Support Deflection	-	X-Force	At Drum Interface
7	a	End Support Deflection	-	Y-Force	At Drum Interface

Figure 2.3-8. Load Deflection Tests

2.3.3.3 Test Sequence

2.3.3.3.1 Test Arrangements

2.3.3.3.1.1 Solar Array Configuration. The test article used for the load deflection tests consisted of the RA250 solar array test article in its stowed configuration. The end supports were detached for the test. This article was mounted to its handling fixture during these tests.

2.3.3.3.1.2 Test Configuration. The solar array general arrangements for the load deflection tests are illustrated in Figure 2.3-9. These tests were performed in the solar array test area in the GE Valley Forge Space Center. As indicated in Figure 2.3-9, the solar array was in its stowed configuration, mounted to its aluminum handling fixture (which in turn was sitting on a dolly), and had its end supports detached.

Several provisions had to be incorporated into the assembly described above, in order to perform the test program outlined in Figure 2.3-8. First, in order to take deflection measurements at the drum end caps (Points A, B, C and D in Figures 2.3-9 and 2.3-8), aluminum blocks were attached by means of double-backed tape. The dial indicators used to measure deflections had their indicator arms touching these blocks; their other extremities were clamped securely to magnetic stands. These stands sat on steel plates, firmly anchored to the RA250 aluminum handling fixture by means of C-clamps.

In order to load the drums at the ends without imposing loading directly upon the stowed blankets, nylon core was passed through lightening holes in the end caps, and tied together to form loops (Figure 2.3-9). A manually operated force gage was hooked to these loops, and operated in a pull mode. Care was taken to make these loops long enough to preclude their interference with the dial indicator arrangements.

The two force gages employed for this test were manually operated units capable of registering up to 50 pounds of force. The four dial indicators, each with sensitivities of 10^{-3} inches, were capable of registering deflections of up to 1 inch.

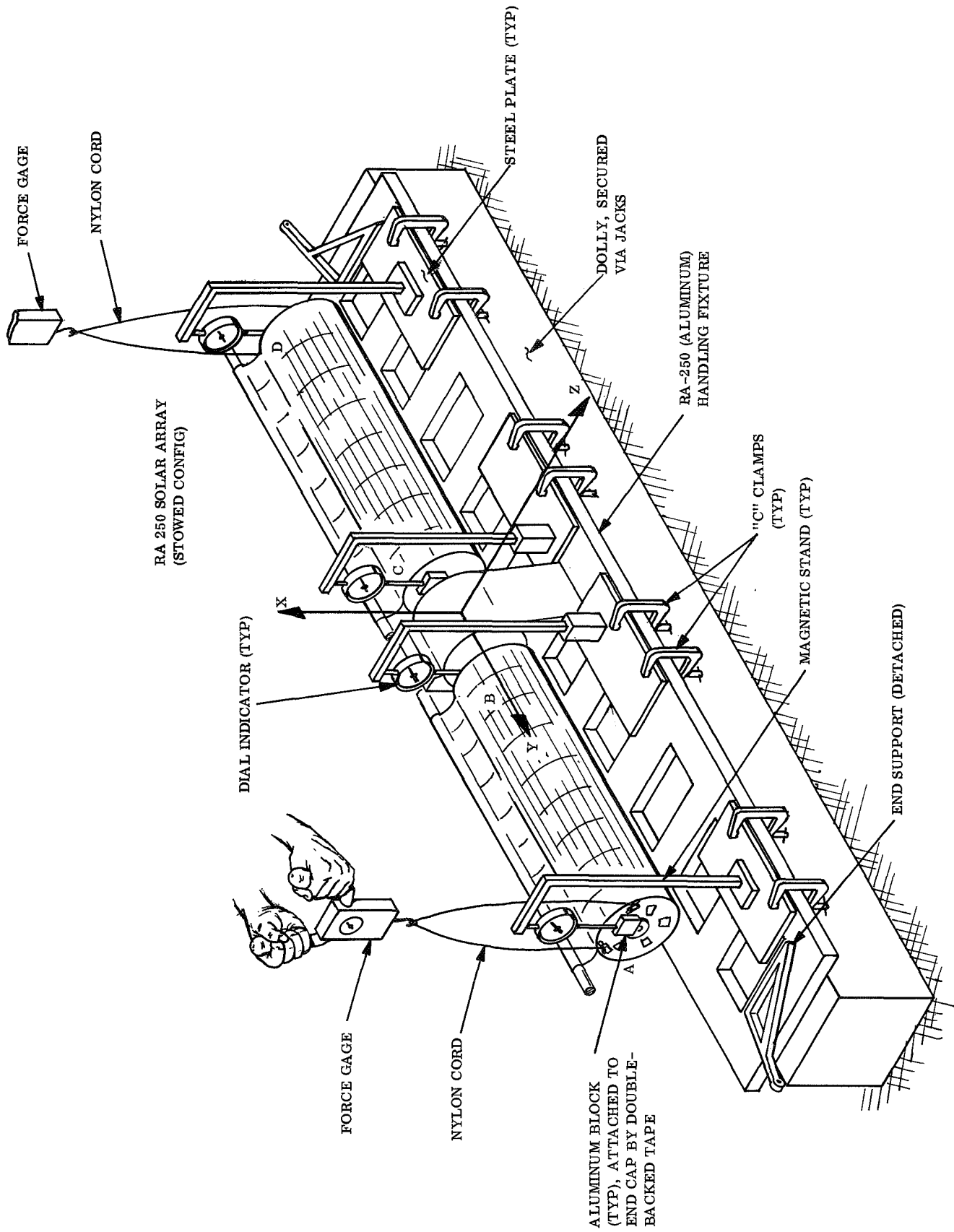


Figure 2.3-9. Test Arrangements

2.3.3.3.1.3 Test Data Provisions. As cited above, loads were manually applied by two force gages, and deflections measured by four dial indicators. Locations of these dial indicators are described in Figure 2.3-8 and illustrated in Figure 2.3-9.

During these tests, force was regulated by maintaining the desired manual pull, based on the force gages dial indicator. These loads were applied incrementally and recorded (Table 2.3-2). Load was applied in gradual increments, whose deflections were read and recorded.

2.3.3.4 Test Procedures

2.3.3.4.1 Test Program

The RA250 solar array test article was subjected to a series of load-deflection tests (Figure 2.3-8). With the end supports detached from the stowed configuration drum, tests will be performed both on the drums alone (tests 1 through 6) and also on the unattached end supports (test 7).

Full specifics of these tests including loading and deflection measurement plans are given in Figure 2.3-8. It will be noted that both symmetric loading conditions (tests 1, 3, 5) and antisymmetric loading conditions (tests 2, 4, 6) were imposed on the drums. This loading and deflection data from each drum test (i. e. , test 1a and 1b) was manipulated in the manner shown in Appendix A, to yield flexibility influence coefficient data.

Tests performed on the drums (tests 1 through 6) consisted (where practicable), of loading applications (Figure 2.3-8) in accordance with the following schedule:

1. +5 lb	5. +15 lb	9. -5 lb	13. -15 lb
2. +10 lb	6. +10 lb	10. -10 lb	14. -10 lb
3. +15 lb	7. +5 lb	11. -15 lb	15. -5 lb
4. +20 lb	8. 0 lb	12. -20 lb	16. 0 lb

Table 2.3-2. Test Data

Test 1A, Symmetric Loads in X-Direction

Applied Load (lb)		Dial Indicator Reading				Deflection (in.)			
A	B	A	B	C	D	A	B	C	D
0	0	500	700	200	300	0	0	0	0
+5	+5	523	700	200	320	0.023	0	0	0.020
+10	+10	548	700	200	345	0.048	0	0	0.045
+15	+15	585	700	200	380	0.085	0	0	0.080
+20	+20	615	700	200	410	0.115	0	0	0.110
+15	+15	585	700	200	378	0.085	0	0	0.078
+10	+10	545	700	200	348	0.045	0	0	0.048
+5	+5	520	700	200	325	0.020	0	0	0.025
0	0	496	700	200	302	-0.004	0	0	0.002

Test 2A, Antisymmetric Loads in X-Direction

Applied Load (lb)		Dial Indicator Reading				Deflection (in.)			
A	B	A	B	C	D	A	B	C	D
0	0	500	700	200	300	0	0	0	0
+5	-5	521	700	200	265	0.021	0	0	-0.035
+10	-10	552	700	200	233	0.052	0	0	-0.067
+15	-15	600	700	200	195	0.100	0	0	-0.105
+20	-20	640	700	200	160	0.140	0	0	-0.140
+15	-15	610	700	200	182	0.110	0	0	-0.118
+10	-10	565	700	200	220	0.065	0	0	-0.080
+5	-5	530	700	200	260	0.030	0	0	-0.040
0	0	497	700	200	290	-0.003	0	0	-0.010

Table 2.3-2. Test Data (Cont'd)

Test 3A, Symmetric Loads in Z-Direction

Applied Load (lb)		Dial Indicator Reading				Deflection (in.)			
A	B	A	B	C	D	A	B	C	D
0	0	500	700	400	200	0	0	0	0
+5	+5	523	700	400	220	0.023	0	0	0.020
+10	+10	549	700	400	245	0.049	0	0	0.045
+15	+15	570	700	400	267	0.070	0	0	0.067
+20	+20	592	700	400	292	0.092	0	0	0.092
+15	+15	574	700	400	270	0.074	0	0	0.070
+10	+10	557	700	400	250	0.057	0	0	0.050
+5	+5	535	700	400	224	0.035	0	0	0.024
0	0	509	700	400	201	0.009	0	0	0.001
-5	-5	483	700	400	179	-0.017	0	0	-0.021
-10	-10	459	700	400	159	-0.041	0	0	-0.041
-15	-15	434	700	400	137	-0.066	0	0	-0.063
-20	-20	410	700	400	115	-0.090	0	0	-0.085
-15	-15	431	700	400	130	-0.069	0	0	-0.070
-10	-10	456	700	400	152	-0.044	0	0	-0.048
-5	-5	475	700	400	176	-0.025	0	0	-0.024
0	0	498	700	400	195	-0.002	0	0	-0.005

Test 4A, Antisymmetric Loads in Z-Direction

Applied Load (lb)		Dial Indicator Reading				Deflection (in.)			
A	B	A	B	C	D	A	B	C	D
0	0	500	700	400	200	0	0	0	0
-5	-5	465	700	400	236	-0.035	0	0	0.036
-10	-10	425	700	400	278	-0.075	0	0	0.078
-15	-15	385	700	400	315	-0.115	0	0	0.115
-20	-20	346	700	400	358	-0.154	0	0	0.158
-15	-15	377	700	400	325	-0.123	0	0	0.125
-10	-10	411	700	400	293	-0.089	0	0	0.093
-5	-5	447	700	400	265	-0.053	0	0	0.065
0	0	493	700	400	211	-0.007	0	0	0.011

Continuous deflection readings were taken. Acquired deflections were plotted against applied load to ascertain the degree of force-play within the bearing assemblies. Such free-play would be evidenced by the existence of hysteresis loops in the load-deflection plots (Figure 2.3-10).

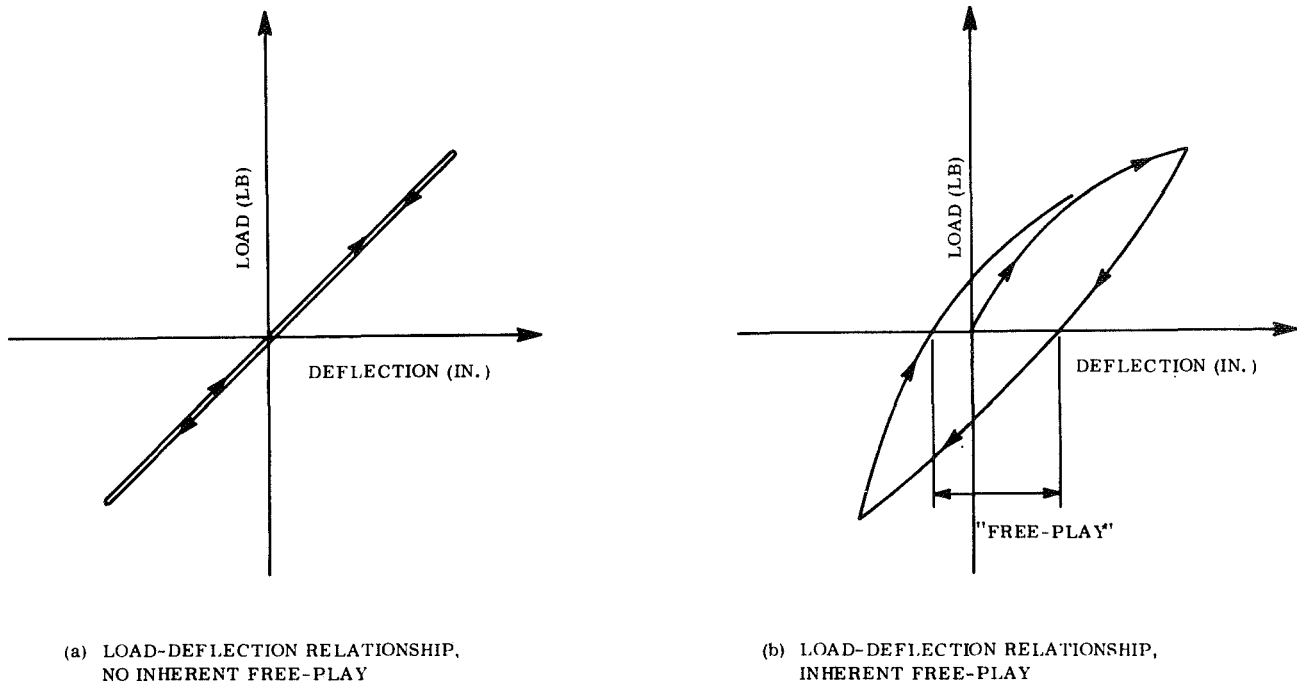


Figure 2.3-10. Effects of Free-Play on Load-Deflection Curves

2.3.3.4.2 X-Axis Symmetric Loading Tests

Test 1a (symmetric loads on outboard drum end caps) and test 1b (symmetric loads on drums inboard drum caps) were performed initially. In performing test 1a, it was observed that only positive (+X-direction) could be applied to the drum as a result of clearance problems between drum and detached end support. Consequently, load was applied to drum caps in 5-pound increments, up to 20-pounds; loading was gradually decreased at a similar rate.

While the outboard drum extremities deflected under applied load, no motion at all was detected at the inboard drum caps.

Data acquired during test 1a is shown in Table 2.3-2, and in Figure 2.3-11.

Test 1b did not yield any deflection data at all for loads of up to 30 pounds, consequently, plans to perform this test could not be carried out. One fact was evidenced, however, the drum exhibits no, free play or chatter.

2.3.3.4.3 X-Axis Antisymmetric Loading Tests

Experiences and performance of test 2b were identical to those of tests 1a and 2a. Test results are shown in Table 2.3-2 and Figure 2.3-12.

2.3.3.4.4 Z-Axis Symmetric Loading Tests

Experience in performing tests 3a and 3b (Figure 2.3-8) were identical to those cited in Section 2.3.3.4.2 (for X-axis symmetric loading conditions). Here, however, loads on the outboard drum extremities (test 3a) were increased to +20 pounds, then decreased gradually to -20 pounds, and thence increased to zero.

Test data is presented in Table 2.3-2 and Figure 2.3-13. It should be noted that:

(1) force-deflection values are quite linear and relatively free of hysteresis effects, and
(2) the data is in very close proximity to data acquired for the X-axis symmetric loading test (test 1a).

2.3.3.4.5 Z-Axis Antisymmetric Loading Tests

Tests 4a and 4b experiences were identical to those of their X-axis counterparts, test 2a and 2b (Section 2.3.3.4.3).

Test results are presented in Table 2.3-2 and Figure 2.3-14. Here, it should also be noted that: (1) force deflection values are quite linear and free of hysteresis effects, and (2) the data is in close proximity to that acquired during the X-axis antisymmetric loading test (test 2a).

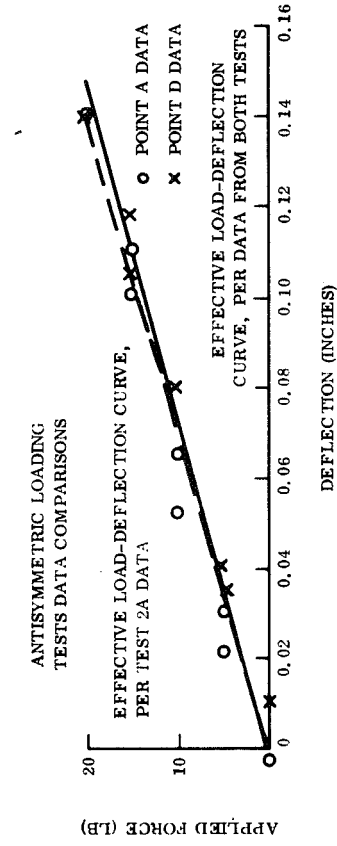
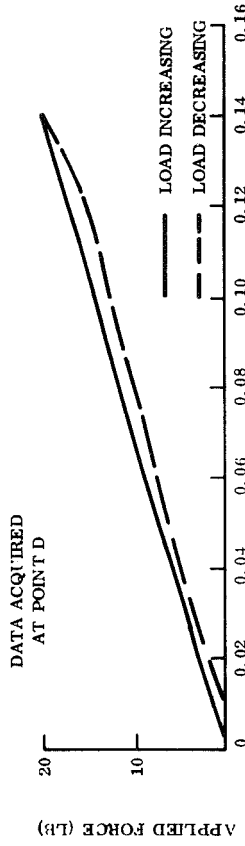
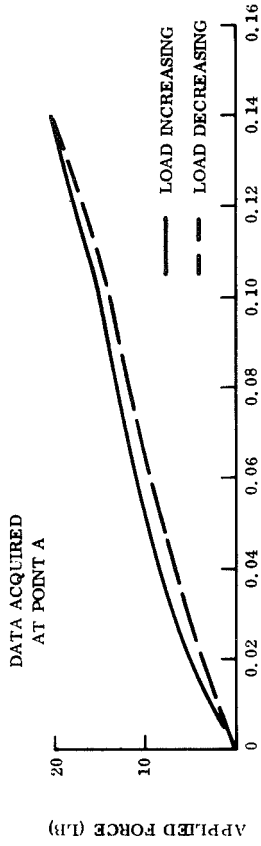
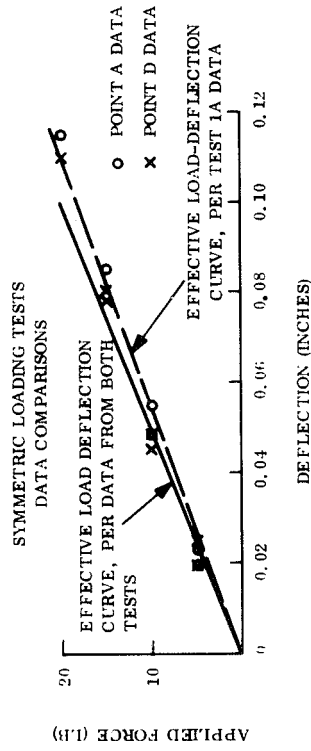
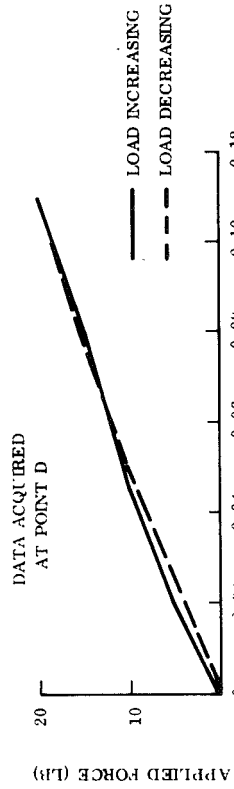
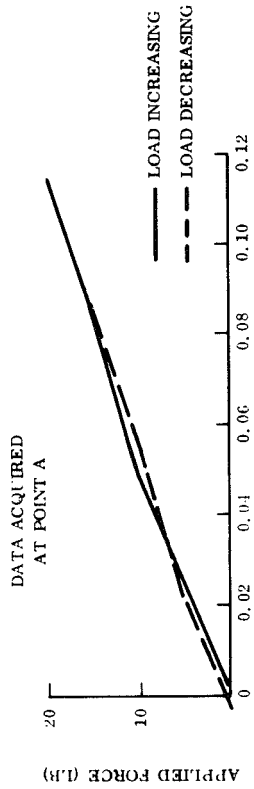


Figure 2.3-11. Results of Test 1A, Symmetric Loading in X-Direction

Figure 2.3-12. Results of Test 2A, Antisymmetric Loading in X-Direction

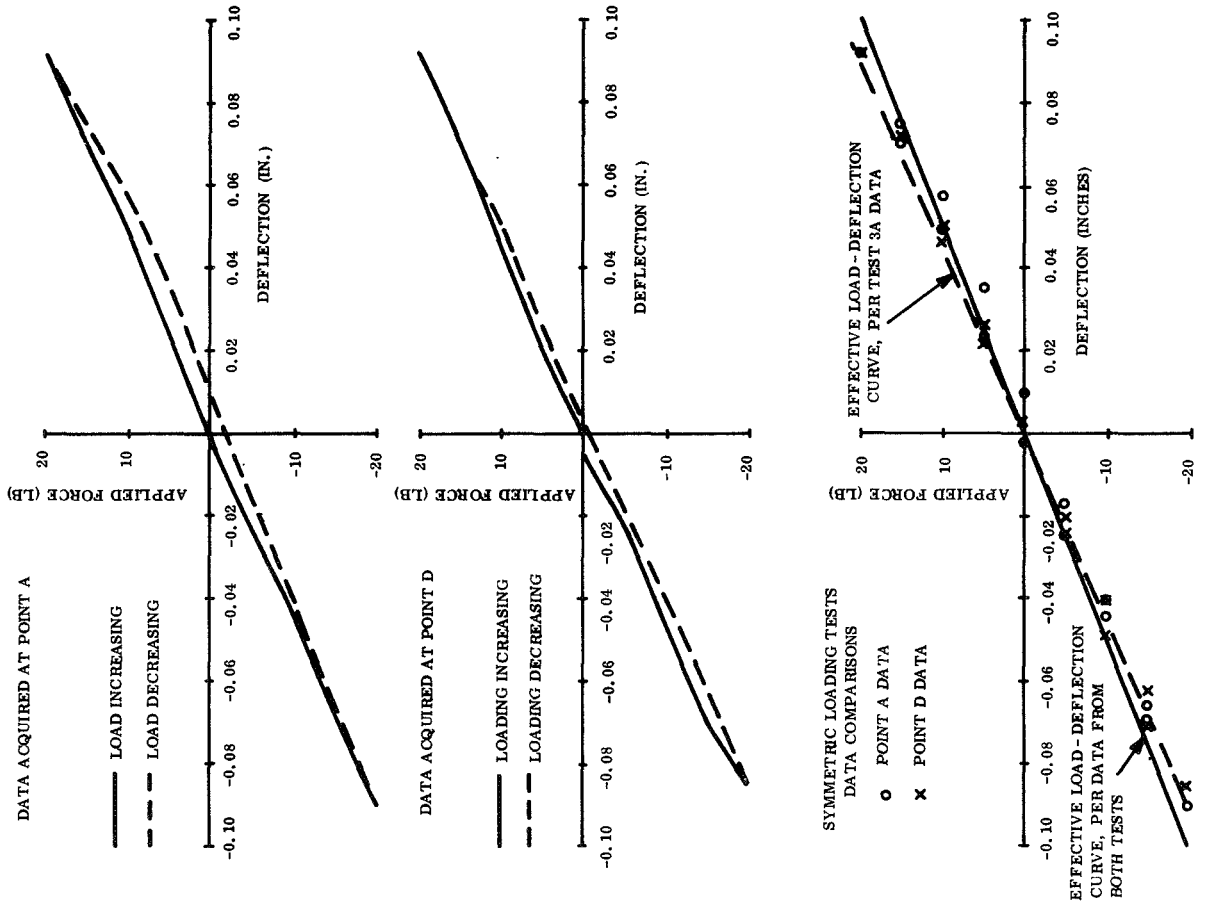


Figure 2.3-13. Results of Test 3A, Symmetric Loading in Z-Direction

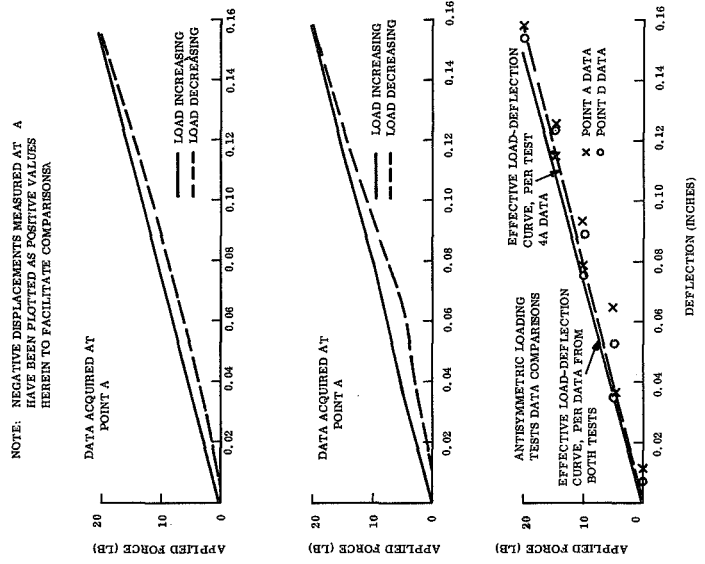


Figure 2.3-14. Results of Test 4A, Antisymmetric Loading in Z-Direction

2.3.3.4.6 Y-Axis Loading Tests

The Y-axis testing (tests 5a and 6a) yielded no measurable longitudinal (Y-axis) deflections under up to 30 pounds of applied force.

2.3.3.4.7 End Support Tests

The unique spring-latch attachment of the end support to the handling fixture precluded performing tests 7b and 7c; test 7a (Z-axis loading, per Figure 2.3-8) was performed. A 0.080-inch Z-displacement was recorded under a 15 pound, X-axis force.

2.3.3.5 Test Results

2.3.3.5.1 Linearity and Repeatability of Data

As indicated by Figures 2.3-11 through 2.3-14 and Table 2.3-2, there is good agreement between load deflection measurements for both the X-axis (test 1a) and Z-axis (test 3a) symmetric loading conditions. A similar statement also holds for the measurements taken for both the X-axis (test 2a) and Z-axis (test 4a), antisymmetric loading conditions. The test data exhibits very little (if any) hysteresis effects, and thus indicates that there is no free-play or chatter inherent in this assembly. Straight-line plots of load versus deflection show extremely good correlation with measured test data.

This lack of free-play or chatter was also verified by the lack of Y-axis displacements (in milli-inches) under applied loads (tests 5a and 6a).

2.3.3.5.2 Bearing Assembly Flexibility Coefficients

The linearity and similarity of data acquired during the X-axis and Z-axis symmetric tests (tests 1a, 1b, 3a, and 3b) make it possible to extrapolate load and deflection data from which a bearing assembly flexibility coefficient can be extracted. The load-deflection relationships from Table 2.3-2, Figure 2.3-11, and Figure 2.3-13 are as follows:

Test No.	Test Axis	Mean Deflections Under 20-lb Force (in.)		$K_{\text{eff}} = \frac{20\text{-lb Force at A}^*}{\text{Deflection at A}}$
		At A&D	At B&C	
1A	X	0.110	0	182
3A	Z	0.090	0	122
Mean for both tests		0.100	0	200
*(Tolerance of K_{eff} is approximately $\pm 10\%$ with respect to test 1A and 3A data)				

Therefore, a mean deflection of 0.10 inch at A and D (Figures 2.3-9 and 2.3-10) and zero deflection at B and C, can apply for both X-axis and Z-axis symmetric loading conditions (with 20-pound forces applied at A and D). The ± 10 percent tolerance is considered acceptable.

The flexibility influence coefficients across the bearing assembly was calculated (Appendix B) using the derivations and assumptions given in Appendix A. The following results from Appendix B are applicable to both the X- and Z- axes):

1. Rotation at B Due to Applied Moment

$$(C_{\theta_B, M})_{\text{brg}} = 2.365 (10^{-6}) \text{ rad/in. -lb}$$

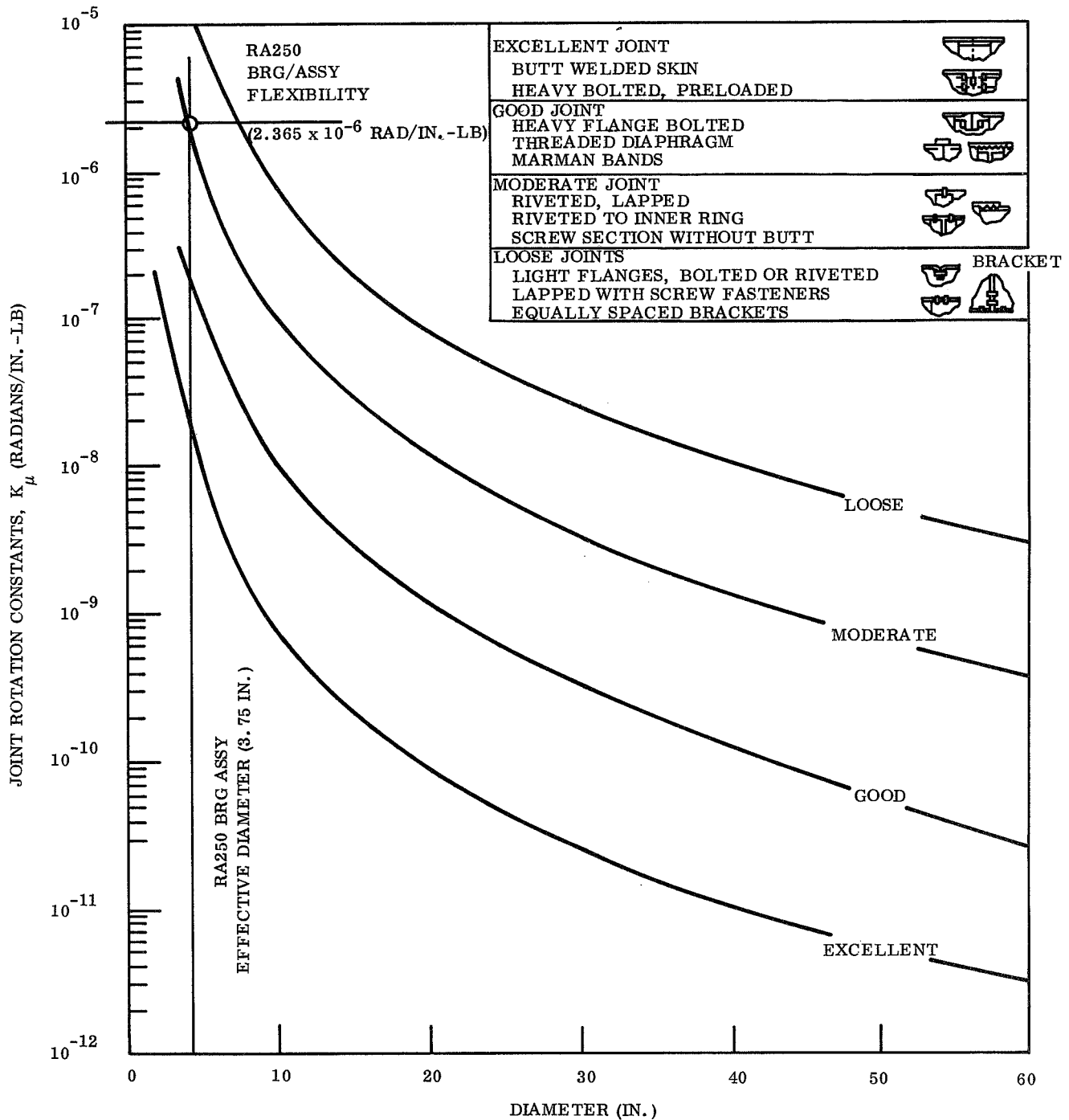
2. Displacement at B Due to Applied Force

$$(C_{\delta_B, F})_{\text{brg}} = 0$$

3. Displacement at B Due to Applied Moment

$$(C_{\delta_B, M})_{\text{brg}} = 1.088 (10^{-4}) \text{ in/in. -lb}$$

A check on $(C_{\theta_B, M})_{\text{brg}}$ can be furnished from the joint flexibility curves of Alley and Leadbetter (Ref. 7) (Figure 2.3-15). With no free-play inherent in the small finite-length



REF: ALLEY, V. L., AND LEADBETTER, S. A., "PREDICTION AND MEASUREMENT OF NATURAL VIBRATIONS OF MULTISTAGE LAUNCH VEHICLES" AIAA, VI, N2, P377 (FEB 1963)

Figure 2.3-15. Comparison of Bearing Flexibility Coefficient With Alley-Leadbetter Joint Flexibility Curves

bearing assembly, this could be placed in the "moderate joint" category* in Figure 2.3-15. For an effective 3.75 inches in diameter, the joint rotation constant is 2×10^{-6} rad/in. -lb, a value in good agreement with C_{θ_B} , M.

2.3.3.5.3 Center Support Flexibility

The linearity and similarity of data acquired during both the X-axis and Z-axis antisymmetric loading tests (tests 2a, 2b, 4a, and 4b) make it possible to extrapolate load and deflection data from which a center support flexibility coefficient can be extracted. The load-deflection relationships from Table 2.3-2, Figure 2.3-12 and Figure 2.3-14 are as follows:

Test No.	Test Axis	Mean Deflections Under 20-lb Force (in.)		$K_{\text{eff}} = \frac{20\text{-lb Force at A}^*}{\text{Deflection at A}}$
		At A&D	At B&C	
2A	X	0.140	0	143
4A	Z	0.156	0	128
Mean for both tests		0.148	0	135
*(Tolerance of K_{eff} is approximately $\pm 6\%$ with respect to test 2A and 4A data)				

A mean deflection of 0.148 inches at A and D (Figures 2.3-9 and 2.3-10) and zero deflection at B and C can apply for both Z-axis and X-axis antisymmetric loading conditions (with 20-pound forces applied at A and D). The ± 6 percent tolerance is considered acceptable.

This displacement (per assumptions in Appendixes A and B) is attributed both to bearing assembly flexibility and center support flexibility. Using data derived previously for bearing flexibility effects, the center support flexibility coefficient was calculated (Appendix B). The following results from Appendix B are applicable to both the X- and Z- axes:

$$\frac{\text{Rotation Due to Applied Moment}}{(C_{\theta, M}) \text{ c/s}} = 5.12 (10^{-7}) \text{ rad/in. -lb}$$

*Had the assembly experienced free play, it would be classified as a "loose joint."

2.3.3.5.4 End Support Flexibility Coefficient

From test data cited in Section 2.3.3.4.7, the flexibility coefficient (C_{δ_Z, F_Z}) describing the Z-axis displacement of the end support due to an X-axis force is:

$$C_{\delta_Z, F_Z} = 5.33 (10^{-3}) \text{ in./lb}$$

2.3.3.6 Conclusions

Test results and conclusions may be summarized as follows:

1. The drums exhibit very little, if any, indications of chatter or free-play in the bearing assembly.
2. Test-acquired load deflection data was quite linear and did not show any big vestiges of free-play produced hysteresis (Figures 2.3-9 through 2.3-14).
3. Test data acquired during X-axis and Z-axis symmetric loading tests were in quite close (± 10 percent) proximity. Similarly, data measured during X-axis and Z-axis antisymmetric loading tests, were in better (within ± 6 percent) agreement.
4. The drum and bearing assembly possess a relatively high level of longitudinal (Y-axis) stiffness, i. e. , it could not be measured by the test techniques employed.
5. Flexibility coefficients for the bearing assembly shown below are applicable to both the X-axis and the Z-axis:

a. Rotation at B Due to Applied Moment

$$(C_{\theta_B, M})_{\text{brg}} = 2.365 (10^{-6}) \text{ rad/in-lb}$$

b. Displacement at B due to Applied Force

$$(C_{\delta_B, F})_{\text{brg}} = 0$$

c. Displacement at B due to Applied Moment

$$(C_{\delta_B, M})_{\text{brg}} = 1.088 (10^{-4}) \text{ in/in-lb}$$

The $(C_{\theta, M})_{\text{Brg}}$ value is in good agreement with the data in the Alley-Leadbetter curves for a "moderate joint".

6. The center support flexibility coefficient shown below is applicable to both X-axis and Z-axis:

- a. Rotation Due to Applied Moment

$$(C_{\theta, M})_{\text{c/s}} = 5.12 (10^{-7}) \text{ rad/in-lb}$$

7. The end support Z-axis flexibility under an applied force is:

$$C_{\delta_Z, F_Z} = 5.33 (10^{-3}) \text{ in/lb}$$

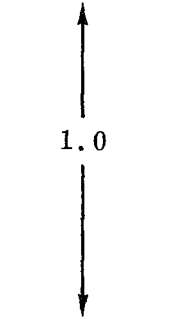
The unique spring-latch attachment of the end support, precluded taking Y-axis and Z-axis measurements.

8. The experimental flexibility coefficients derived from this test are being incorporated into the RA250 stowed configuration analytical model.

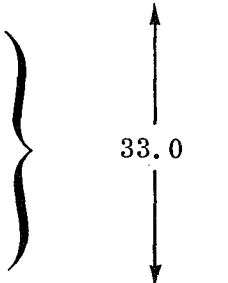
2.3.4 BI-STEM COMPONENT VIBRATION TEST

The Bi-Stem solar panel actuator designed and developed by Spar Aerospace Products Ltd. successfully passed the following component vibration levels of General Electric Specification SVS 7552. Vibration associated anomalies are discussed in Section 2.2.

A. Sinusoidal

Frequency Range (Hz)	Acceleration Input Level	Sweep Rate (oct/min)
10 to 13	0.5 in. DA displ	
13 to 50	± 4.0 g	
50 to 150	± 8.0 g	
150 to 380	± 12.0 g	
380 to 550	0.0016 in. DA displ	
550 to 2000	± 27.0 g	

B. Random

Frequency Range (Hz)	Power Spectral Density (g ² /Hz)	Acceleration (g - rms)
20 to 117	Increased at +6db/octave	
117 to 300	1.7	
300 to 400	Decreased at -6db/octave	
400 to 700	1.0	
700 to 2000	Decreased at -6db/octave	

2.3.5 AIRESEARCH MOTOR/GEARHEAD TEST

2.3.5.1 General Discussion

An Airesearch Gearhead Motor P/N 36790-1-1 was tested to determine if it was capable of operating the rollup solar array for the required duty cycle without overheating when in vacuum. It had already been determined from previous testing (Airesearch Test Report F-4105-R) that it would operate under rated conditions in vacuum. The ratings are 120 oz-in. load 1 minute on, 5 minutes off. The present test was to determine if it would handle the maximum expected load of 20 oz-in. with a duty time of 5 minutes on.

Operating conditions were represented by use of the following assumptions:

1. Motor losses are made up of a constant (friction and windage) plus a variable (I^2R).
2. With no heat paths out of the motor, temperature rise is linearly proportional to motor losses.
3. The heat lost through radiation and conduction with a high temperature differential (100°F) is no less than that lost through all methods under still air conditions and low temperature differential ($< 10^{\circ}\text{F}$).

The motor was run without any load, and the input power was measured to determine friction and windage losses. This was repeated at the maximum load available (6.4 oz-in.) as a check of assumption 1.

After allowing a cooling off period, a controlled current was applied to the motor with the rotor locked. The temperature rise in the motor was measured by means of winding resistance for a period of 10 minutes. A second test was run at a higher input power level but otherwise identical conditions.

2.3.5.2 Conclusions

The temperature rise predicted by this test was 96° F in 5 minutes. This is well within the capabilities of this motor, and therefore, no problem is anticipated.

In addition, two other items should be noted. First, the experiment was designed to simulate a condition where there was no heat transfer from the motor. Actually, there will be both radiation and conduction. While these may not be very large, they will dissipate some heat; therefore, the actual temperature rise should not be as great as projected.

Second, it was noticed that when running, the total losses in the motor were very high compared to the I^2R loss. This means that there is high friction and heat generation in the power train - (gears, bearings, lubrication, etc.) - rather than in the armature winding. These devices are in fairly good thermal contact with the motor frame compared to the armature; therefore, heat loss through conduction should be quite high. All of this tends to indicate that the motor will be capable of driving its anticipated load under vacuum conditions.

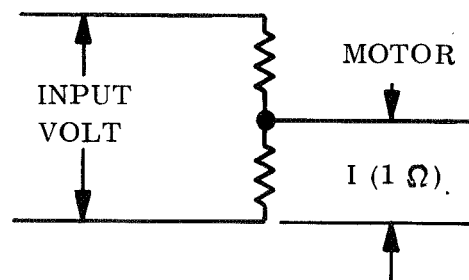
2.3.5.3 Test Results

The test data was plotted, and as expected, showed hyperbolic type curves. In accordance with assumption 3, the slope of the curve near the origin was used to plot the temperature rise under no heat loss conditions. From assumption 1, the motor losses for the expected loads were calculated. The slope of the temperature rise curve was then increased by the ratio of the expected motor run losses to the losses measured during the test in accordance with assumption 2. These curves are plotted in Figure 2.3-16.

2.3.5.3.1 Data

A. No Load:

R_{RG}^* = 3.85 Ω at 100° F base temperature
Run current = 0.880 amperes
Run voltage = 27 volts



* R_{RG} is the resistance of the armature circuit which includes the brushes.

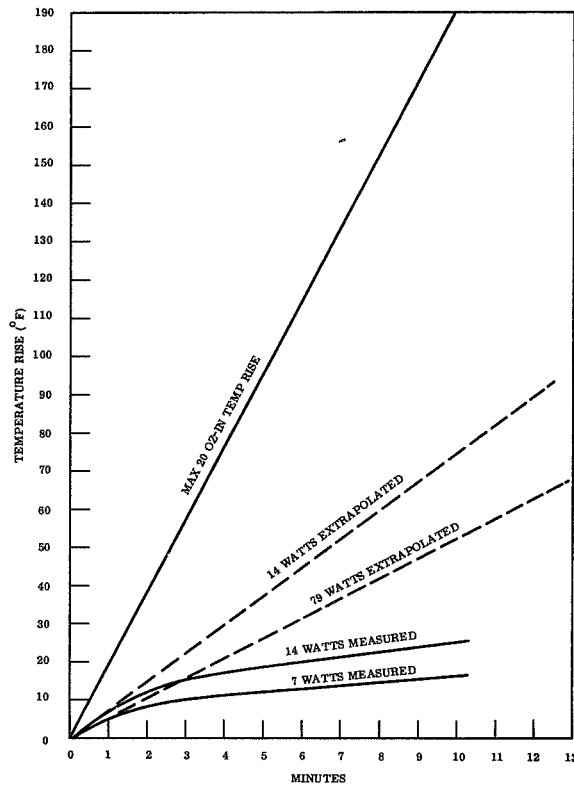


Figure 2.3-16. Extrapolated Temperature Rise for the Airesearch P/N 36790-1-1 Gearhead dc Motor

Run power = 23.8 watts
 R_{RG} = 3.95 Ω
 Δ Temperature = 9.8 $^{\circ}$ F in 1 minute (field WDG)
Winding loss = \approx 5 watts

B. At 6.4 in. -oz Load

Run current = 0.970 amperes
Run power = 26.2 watts
 R_{RG} = 4.08 Ω
 Δ Temperature = 18 $^{\circ}$ F in 2 minutes (field)
 Δ Temperature = 30 $^{\circ}$ F in 4 minutes with 45 seconds off
Winding loss = \approx 7 watts

C. Locked Rotor

Power Input: 7 watts, 6.98 volts, 1 Ω shunt

<u>Minutes</u>	<u>Amperes</u>	<u>Δ ohms</u>	<u>Δt °F</u>
0	1.100	6.35	0
1	1.088	6.42	5.06
2	1.081	6.45	7.23
3	1.077	6.47	8.7
4	1.074	6.49	10.1
5	1.064	6.55	14.5
6	1.061	6.57	15.9
7	1.064	6.55	14.5
8	1.063	6.56	15.2
9	1.061	6.57	15.9
10	1.060	6.58	16.6

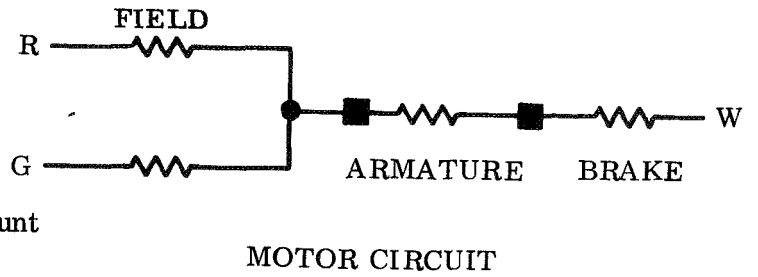
D. Locked Rotor

Power input: 14 watts

<u>Minutes</u>	<u>Amperes</u>	<u>Δ ohms</u>	<u>Δt °F</u>
0	1.500	6.24	0
1	1.456	6.42	13.2
2	1.475	6.34	7.4
3	1.463	6.39	11.0
4	1.452	6.43	14.0
5	1.444	6.48	17.6
6	1.439	6.50	19.1
7	1.434	6.52	20.6
8	1.432	6.53	21.3
9	1.416	6.61	27.5
10	1.416	6.61	27.5

2.3.5.3.2 Note

1. G-W used for locked rotor tests
2. Brush contact problems may account for poor running data
3. Motor was quite noisy
4. High friction loss in gearing



2.3.5.3.3 Calculations

A. Slope of Temperature Rise Lines

7 watts → 5.2°/min or 0.743°/w/min
 14 watts → 7.5°/min or 0.536°/w/min
 Average = 0.639°/w/min

B. Friction and Windage Power

No Load

Total input power = 23.8 watts
 $I^2 R$ losses = 5.0 watts
 Friction and windage = 18.8 watts

A 6.4 oz-in. Load (Check, 405 rpm)

Total input power = 26.2 watts
 $I^2 R$ losses = 7.0 watts
 Power delivered = 0.3 watts
 Friction and windage = 18.9 watts

Power Delivered

$$\begin{aligned} &= (6.4 \text{ oz-in.}) \left(\frac{1}{192} \frac{\text{ft-lb}}{\text{oz-in.}} \right) \left(\frac{405 \text{ rev}}{\text{min}} \right) \left(\frac{2.26 \times 10^{-2} \text{ w-min}}{\text{ft-lb}} \right) \\ &= \frac{(6.4) \cdot (405) \cdot (2.26 \times 10^{-2})}{192} = 0.3 \text{ watts} \end{aligned}$$

C. The 20 oz-in. Load Conditions

Input Current

$$I_{20} = \frac{(I_{6.4} - I_{NL}) (T_{20})}{T_{6.4}} + I_{NL}$$

where

I_{20} = input current at 20 oz-in.

$I_{6.4}$ = input current at 6.4 oz-in. = 0.970 amperes

I_{NL} = input current no load = 0.880 amperes

T_{20} = load torque at 20 oz-in. = 20 oz-in.

$T_{6.4}$ = load torque at 6.4 oz-in. = 6.4 oz-in.

$$I_{20} = \frac{(0.970 - 0.880) (20)}{6.4} + 0.880 = 1.16 \text{ amperes}$$

Power in = (27) (1.16) = 31.2 watts = 31.2 watts

Power out = $\frac{(20) (390) (2.26 \times 10^{-2})}{192} = \underline{0.92}$ watts

Power dissipated in motor = 30.3 watts

D. Slope of 20 oz-in. Temperature Rise Line

$$(0.639^{\circ}/\text{w}/\text{min}) (30.3 \text{ w}) = 19.3^{\circ}/\text{min}$$

E. Expected Temperature Rise in 5 Minutes

$$= 96^{\circ}$$

2.4 SYSTEM TEST PLANNING

The present system test flow remains essentially unchanged from that which appears in Reference 2, with the exception that the acoustic test has been relocated in the sequence so that it follows the deployed modal test (and associated post-test health check). This was done to allow more time for the installation of the vacuum thermal test equipment.

2.4.1 DEPLOYED MODAL TEST

The deployed modal test plan remains essentially unchanged from the description which appears in Reference 2 except for the following simplifications and clarifications:

1. During the out-of-plane bending and torsional modal survey test runs, the trackers should acquire only Z-axis (normal to blanket) measurements. Previous plans called for both Y- (along storage drum axis) and Z-measurements to be taken; the Y-axis movements are expected to be negligible for these test runs. This simplification will greatly reduce data acquisition and reduction time.
2. Perform the out-of-plane bending test run first. Solar array motions along this axis are those most amenable both to analysis and resolution of test data anomalies. Consequently, any unique or unexpected test experiences (including equipment type problems) can be more readily, easily and expediently resolved here.
3. During all sweep tests, position the optical trackers at the 80 percent span station of the deployed array. The analytical predictions show this to be the best location for discerning modes.

The optical target locations to be utilized during the deployed modal test are shown in Figure 2.4-1. The targets on the array blankets are white paper rectangles having a maximum dimension of 14 x 17.5 inches. The targets on the Bi-Stem rod are fabricated from polystyrene and secured to the rod in the double backed tape. Extensive calibration of optical tracker heads and target configurations has been conducted during this report period. With the target configurations specified, it is possible to measure biaxial displacement (Y and Z) over a ± 4 inch Z-stroke and a ± 2 -inch Y stroke with accuracies of ± 3 percent of full stroke.

NOTES

1. TRACKERS 1 AND 8
FIXED.
2. TRACKERS 2-7 TRAVERSE
ALONG X-AXIS, SIGHTING
AT 30 DEGREES TO
Y-X PLANE.

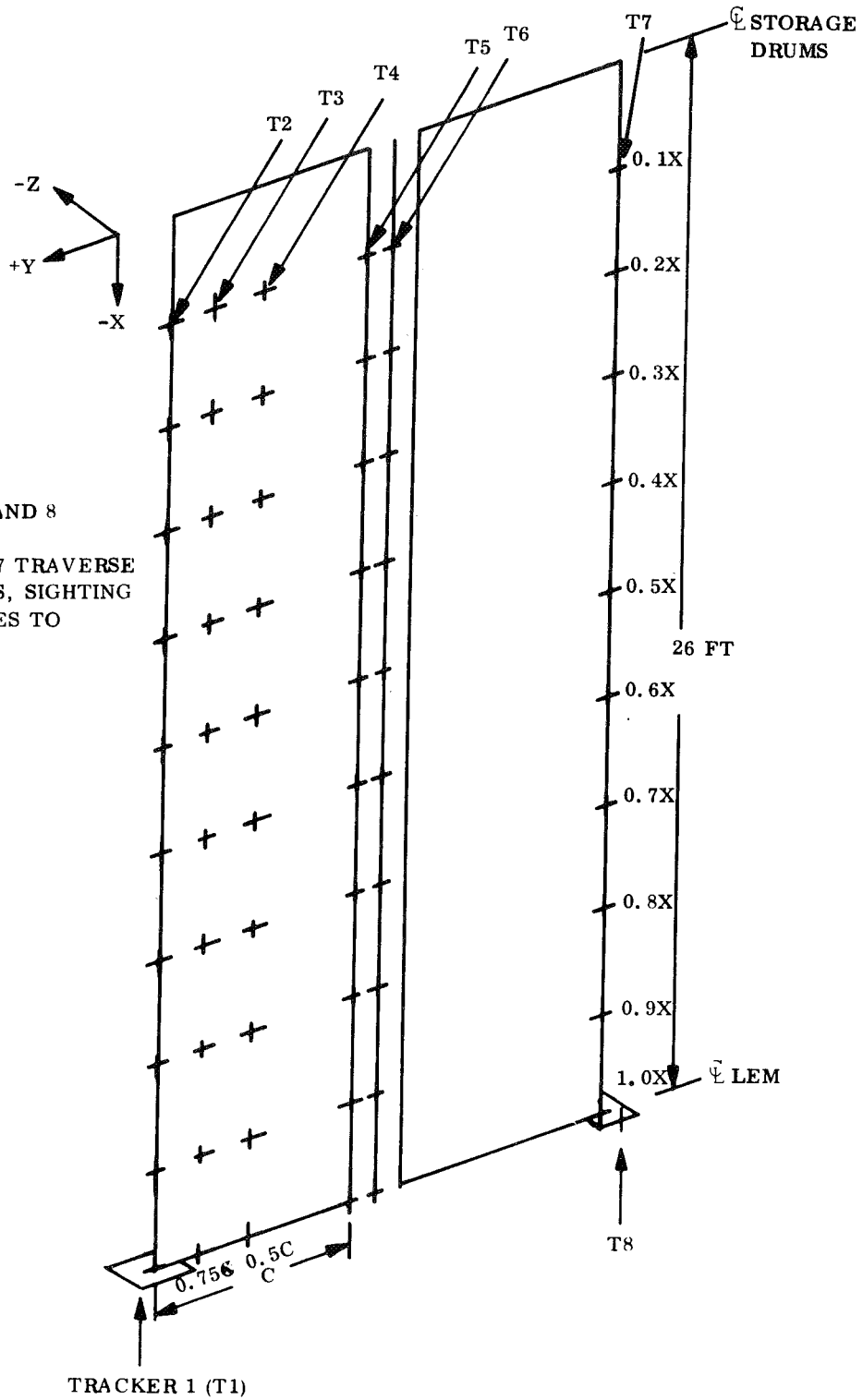


Figure 2.4-1. Array Optical Target and Tracker Distribution

A block diagram of the exciter control and the data recording and processing is shown in Figure 2.4-2. It should be noted that, while all tracking output channels can be recorded simultaneously, only one channel at a time can be analyzed in real time.

2.4.2 Stowed Modal Test

2.4.2.1 Test Objectives

The test article in its stowed configuration shall be subjected to a series of sinusoidal vibration excitations in the 10-2000 Hertz frequency bandwidth. The purposes of these tests are to:

1. Obtain measured natural frequencies and corresponding mode shapes for (up to ten) resonances occurring below 100 Hz; similar data will likewise be obtained for principal drum/assembly resonances occurring in the 100-200 Hz bandwidth. This data shall be employed to assess the accuracy of analytical predictions of structural dynamic characteristics. If the degree of correlation between analytical predictions and experimental data is not good, the latter can be used in any subsequent investigations employing stowed configuration mode shapes and frequencies.
2. Obtain a measure of the damping characteristics of the test model in ambient conditions.
3. Evaluate those modes of vibration peculiar to the blankets (either alone or in conjunction with the storage drums).

2.4.2.2 Test Program

The test program shall consist of a series of sinusoidal vibration test runs (Table 2.4-1) involving the test specimen; these test runs totally will yield a restricted (or limited) modal survey of the solar array in its stowed configuration. This modal survey shall be classified as "restricted" or "limited", in as much as the orthogonality of the measured mode shapes shall not be demonstrated. In all test runs, the stowed solar array shall be cantilevered off its base attachment (fixed-free boundary conditions).

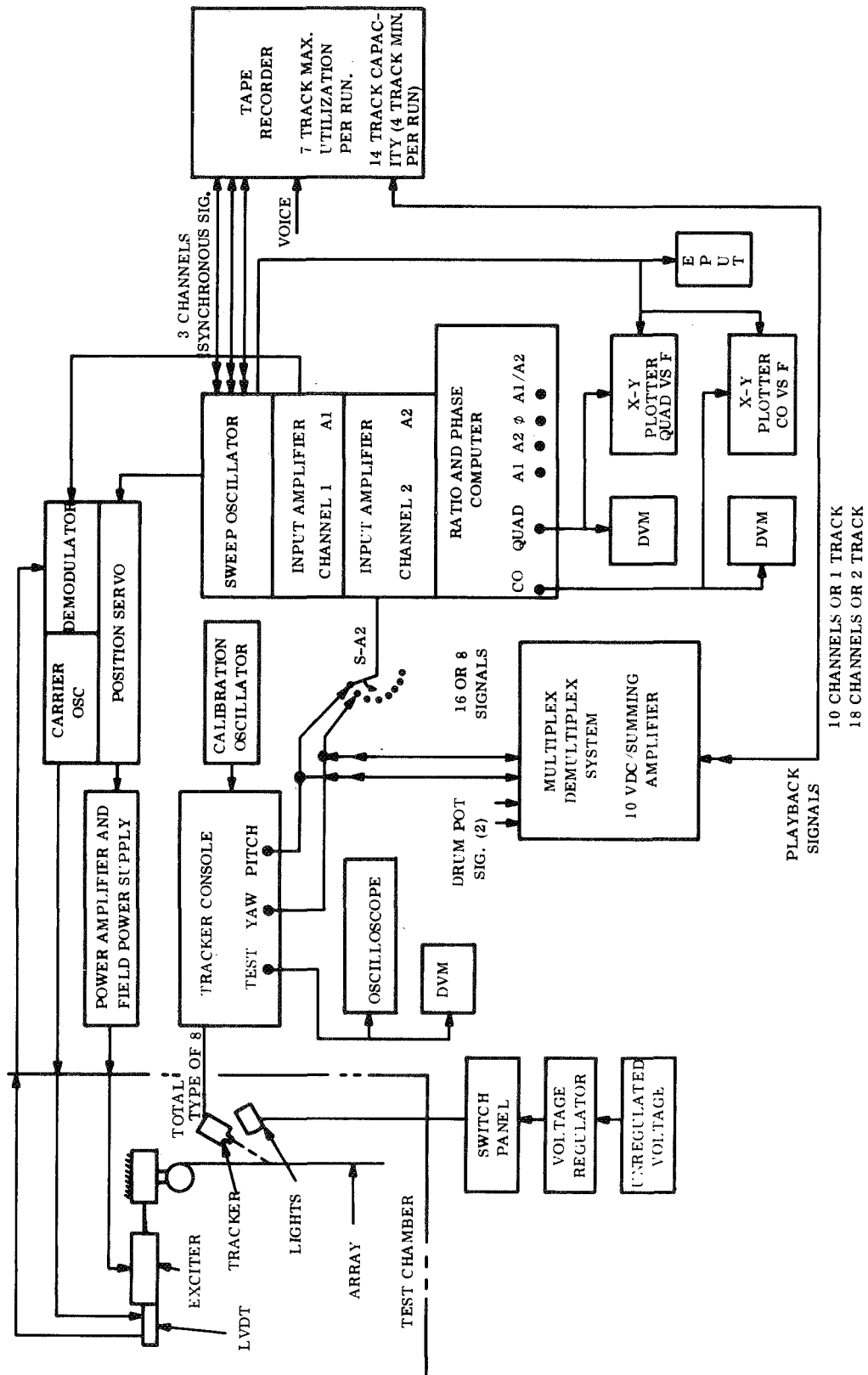


Figure 2. 4-2. Deployed Modal Test Exciter Control and Data Handling Block Diagram

Table 2.4-1. Test Program (Reference: Figure 2.4-3)

Test Schedule Test	Run	Solar Array Configuration	Laboratory Conditions	Excitation Axis	Test Description
1	a	Stowed	Ambient	Lateral (Z-Z)	Resonance Search. Consisting of a low-level sweep (+ 1.0g) from 10 to 2000 Hz. This sweep shall be done at a logarithmic rate (0.5 octave/minute) sufficiently slow to establish the frequencies of peak quadrature.
1	b	Stowed	Ambient	Lateral (Z-Z)	(Virtual) Resonance Swells. (At the four lowest principal resonances.)
1	c	Stowed	Ambient	Lateral (Z-Z)	Linearity Evaluations. Consisting of slow sweeps of narrow frequency bandwidths near principal resonances. These sweeps shall be performed at reduced input levels.
2	a	Stowed	Ambient	Lateral (X-X)	Same as for Test 1a
2	b	Stowed	Ambient	Lateral (X-X)	Same as for Test 1b
2	c	Stowed	Ambient	Lateral (X-X)	Same as for Test 1c
3	a	Stowed	Ambient	Longitudinal (Y-Y)	Same as for Test 1a
3	b	Stowed	Ambient	Longitudinal (Y-Y)	Same as for Test 1b
3	c	Stowed	Ambient	Longitudinal (Y-Y)	Same as for Test 1c

Testing of the stowed configuration shall be performed under ambient conditions at the Valley Forge Vibration Test Facility, Building 400. Excitation shall be furnished by an MB Model C-220 electromechanical shaker. This excitation shall be applied to the base of the test article, via a test fixture; an 800 Hz minimum allowable frequency criteria shall be required for the stowed configuration test fixture(s). The modal tests along the X-, Y-, and Z-axes are illustrated schematically in Figure 2.4-3. Shaker input locations for the modal tests shall be as indicated in Figure 2.4-3. These test arrangements shall employ five Team units as illustrated. The modal test program for each test axis consists of three test runs:

1. Resonance searches (Tests 1a, 2a, 3a)
2. Resonance dwells (Tests 1b, 2b, and 3b) to obtain mode shape data
3. Linearity evaluation tests (Tests 1c, 2c, and 3c) to obtain structural damping data.

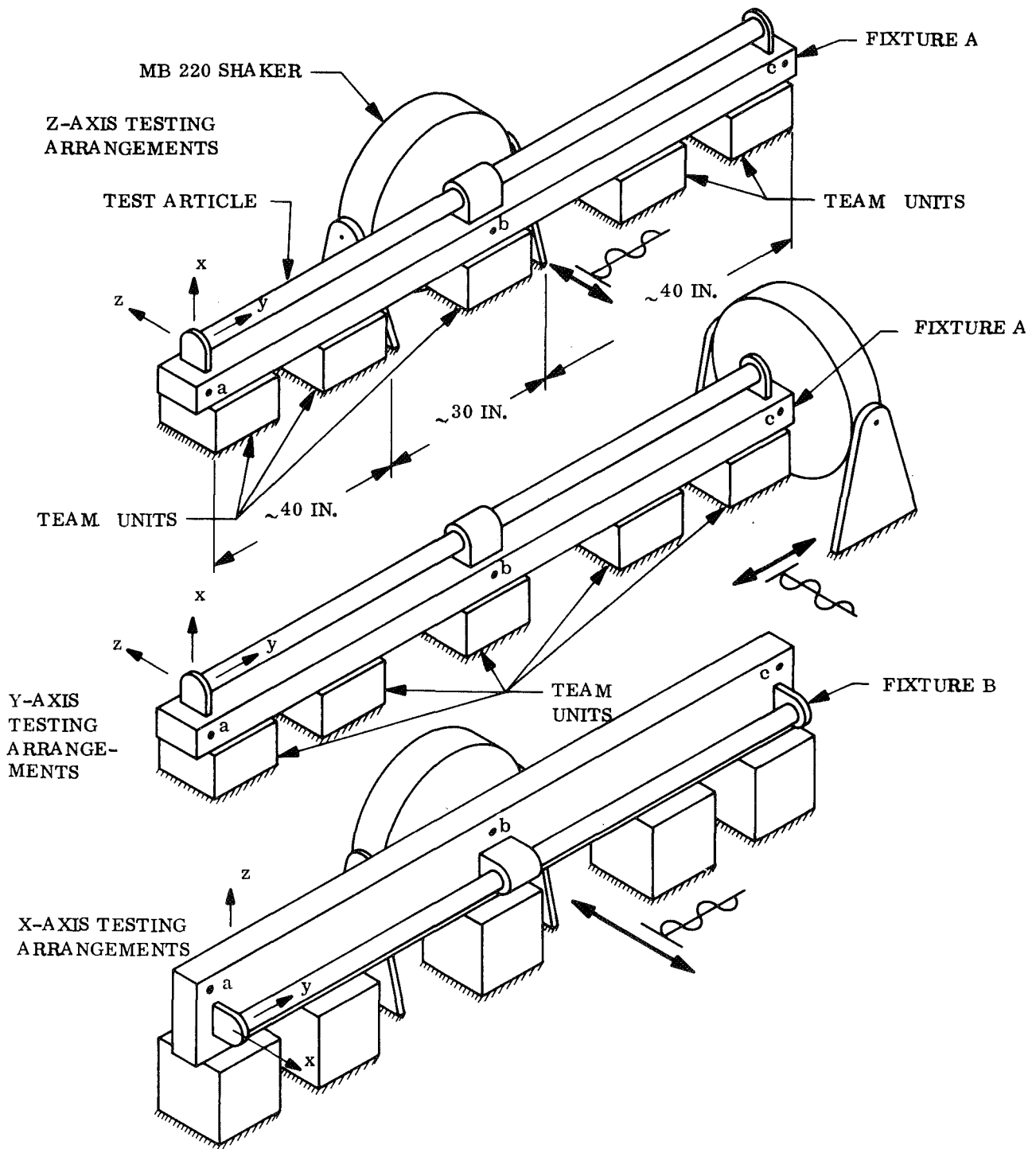


Figure 2.4-3. Schematic Stowed Configuration Modal Test Arrangements

Resonance Searches

The resonant frequencies of the test article will be determined by exciting the structure with a constant sinusoidal lateral base motion. The frequency of the base motion will be logarithmically swept at a rate sufficiently slow to establish the frequency of peak quadrature from 10 to 2000 Hz. The quadrature (or out-of-phase to the exciting motion) at selected locations will be used to determine the resonant frequencies of the test article for the ensuing dwells.

Resonance Dwells

At each of the first three resonant frequencies indicated by the peaking of the quadrature response, the mode shapes of the test article shall be determined. The frequency will be slowly varied in the region of the first resonance and tuned to peak the quadrature response. The first mode shape shall then be determined by scanning all the locations on the test article. The base motion shall then be abruptly stopped and the free decay of the resonant response measured. This procedure shall then be repeated for the next three indicated resonances.

Data obtained during these dwells will be processed to yield mode shapes via the techniques outlined in Section 2.4.2.4. In the event of modal clustering, i. e. , several resonances occur in close frequency proximity, the phase separation technique described in Section 2.4.2.4 shall be employed to separate the modal data.

Modal damping data shall also be obtained from the results of Tests 1b and 1c by two methods. The decay rate of the resonant response induced by abruptly stopping shaker inputs at each principal resonance can be related to modal damping. In addition, the frequencies (f_a) and f_b) at which the in-phase response peaks on either side of a given resonance are related to the damping coefficient via:

$$g = \frac{(f_a/f_b)^2 - 1}{(f_a/f_b)^2 + 1}$$

Values of (f_a) and (f_b) shall be obtained from slow sweeps through narrow frequency bands in the vicinity of each resonance.

Linearity Evaluation Tests

At each of the three resonances investigated during resonance dwells, linearity evaluation tests shall be performed (Tests 1c, 2c and 3c). During these tests, the base motion will be reduced to half the amplitude used for the previous mode shape measurements. The frequency shall be slowly varied to peak the quadrature response. The resonant frequency shall be measured. The base motion shall be abruptly stopped, and the free decay of the resonant response measured. Damping coefficients shall be measured via the same two techniques outlined above. Similar testing will also be performed with the base motion adjusted to some (to be established) factor times the amplitude used for the resonance dwells. Similar data shall be obtained. This will allow explicit curves showing the variation of modal damping with excitation level to be formulated.

Testing Tolerances

Tolerances on test levels shall not be greater than:

1. ± 2 percent on frequency end points
2. ± 10 percent on sinusoidal acceleration amplitude

2.4.2.3 Test Success Criteria

The conventional criteria for the degree of success of a modal test shall not be applied to the stowed configuration modal survey; this, therefore, places this test in the "limited" or "restricted" modal test category. This circumstance arises as a result of the inability to define an explicit mass distribution (matrix) for the stowed solar arrays. As indicated below, the definition of this mass distribution is necessary to assess the degree of orthogonality of test results.

The success of the modal test can be measured in terms of the orthogonality of the experimental data. Orthogonal modes must satisfy the Sturm-Liouville condition, that

$$\int_a^b \left[\frac{\partial m(x)}{\partial x} \right] \phi^{(r)}(x) \phi^{(s)}(x) dx \equiv \begin{bmatrix} \phi_i^{(r)} \end{bmatrix}^T \begin{bmatrix} m_{ij} \end{bmatrix} \begin{Bmatrix} \phi_j^{(s)} \end{Bmatrix}$$

$$= M_{rs} = \begin{cases} 0, & r \neq s \\ M_s, & r = s \end{cases}$$

where (m) reflects the mass distribution (weighting function) and $(\phi_i^{(r)})$ reflects the displacement of the ith station in the rth mode of vibration.

(The probability of attaining $M_{rs} = 0, r \neq s$ is virtually nil when dealing with both discrete mass analytical results and with experimental data. The accepted "complete success" criteria for a modal test is that $M_{rs} < 0.1 M_r$. At the other end of the spectrum, $M_{rs} > 0.3 M_r$ reflects an unsatisfactory test.)

2.4.2.4 Test Data Provisions

Instrumentation Requirements

Modal testing shall require a total of 65 accelerometers, of which 33 shall be miniature transducers (Endevco Model 2229 or equivalent), 17 shall be microminiature accelerometers and 15 shall be regular accelerometers (Endevco Model 2213 or equivalent). Their locations are described in Table 2.4-2 and illustrated in Figure 2.4-4.

These locations shall be the same for the lateral (Z-Z) axis test (Test 1), lateral (X-X) axis test (Test 2) and longitudinal axis test (Test 3). The mounting blocks by which these transducers shall be attached to the test specimen shall be magnesium rectangular parallelepipeds.

It is anticipated that accelerations will vary between $\pm 0.1g$ and $\pm 20g$ during these tests.

Table 2.4-2. Stowed Modal Test Accelerometer Locations (Reference Figures 2.4-4)

Accelerometer Number	Accelerometer Size	Location	Sensing Axis
1	Regular	Center Support-Test Fixture Interface (Shaker Input)	X
2	Regular	Control Accelerometers	Y
3	Regular		Z
4	Miniature	Bi-Stem Actuator	X
5	Miniature		Y
6	Miniature		Z
7	Regular	Leading Edge Member, at Bi-Stem Interface	X
8	Regular		Y
9	Regular		Z
10	Miniature	Leading Edge Member A, 25% Span	X
11	Miniature		Z
12	Miniature	Leading Edge Member A, 50% Span	X
13	Miniature		Z
14	Miniature	Leading Edge Member A, 75% Span	X
15	Miniature		Z
16	Miniature	Leading Edge Member A, 100% Span	X
17	Miniature		Y
18	Miniature		Z
19	Regular	Outboard End Support, at Drum A Interface	X
20	Regular		Y
21	Regular		Z
22	Regular	Top of Center Support, Near Leading Edge Member Interface	X
23	Regular		Y
24	Regular		Z
25	Micro-Miniature	Blanket A, 100% Span, $\theta = 0^\circ$	X
26	Micro-Miniature		Z
27	Micro-Miniature	Blanket A, 100% Span, $\theta = 90^\circ$	X
28	Micro-Miniature		Z
29	Micro-Miniature	Blanket A, 100% Span, $\theta = 180^\circ$	Y
30	Micro-Miniature		Z
31	Miniature	Storage Drum A, 100% Span, $\theta = 0^\circ$	X
32	Miniature		Z
33	Miniature	Storage Drum A, 100% Span, $\theta = 90^\circ$	X
34	Miniature		Z
35	Miniature	Storage Drum A, 100% Span, $\theta = 180^\circ$	Y
36	Miniature		Z
37	Regular	Bearing Housing Inside Drum A	X
38	Regular		Y
39	Regular		Z
40	Micro-Miniature	Blanket A, 50% Span, $\theta = 0^\circ$	X
41	Micro-Miniature	Blanket A, 50% Span, $\theta = 45^\circ$	Radial
42	Micro-Miniature	Blanket A, 50% Span, $\theta = 90^\circ$	Z
43	Micro-Miniature	Blanket A, 50% Span, $\theta = 135^\circ$	Radial
44	Micro-Miniature	Blanket A, 50% Span, $\theta = 180^\circ$	Y
45	Micro-Miniature	Blanket A, 50% Span, $\theta = 225^\circ$	Radial
46	Micro-Miniature	Blanket A, 50% Span, $\theta = 270^\circ$	Z
47	Micro-Miniature	Blanket A, 50% Span, $\theta = 315^\circ$	Radial
48	Miniature	Drum A, 50% Span, $\theta = 0^\circ$	X
49	Miniature	Drum A, 50% Span, $\theta = 45^\circ$	Radial
50	Miniature	Drum A, 50% Span, $\theta = 90^\circ$	Z
51	Miniature	Drum A, 50% Span, $\theta = 135^\circ$	Radial
52	Miniature	Drum A, 50% Span, $\theta = 180^\circ$	Y
53	Miniature	Drum A, 50% Span, $\theta = 225^\circ$	Radial
54	Miniature	Drum A, 50% Span, $\theta = 270^\circ$	Z
55	Miniature	Drum A, 50% Span, $\theta = 315^\circ$	Radial
56	Miniature	Drum A, 33% Span, $\theta = 0^\circ$	Z
57	Miniature	Drum A, 33% Span, $\theta = 90^\circ$	X
58	Miniature	Drum A, 75% Span, $\theta = 0^\circ$	Z
59	Miniature	Drum A, 75% Span, $\theta = 90^\circ$	X
60	Micro-Miniature	Blanket A, Zero Span, $\theta = 0^\circ$	Z
61	Micro-Miniature	Blanket A, Zero Span, $\theta = 90^\circ$	X
62	Miniature	Drum A, Zero Span, $\theta = 0^\circ$	Z
63	Miniature	Drum A, Zero Span, $\theta = 90^\circ$	X
64	Miniature	Drum A, Zero Span, $\theta = 180^\circ$	Y
65	Micro-Miniature	Blanket A, Zero Span, $\theta = 180^\circ$	Y

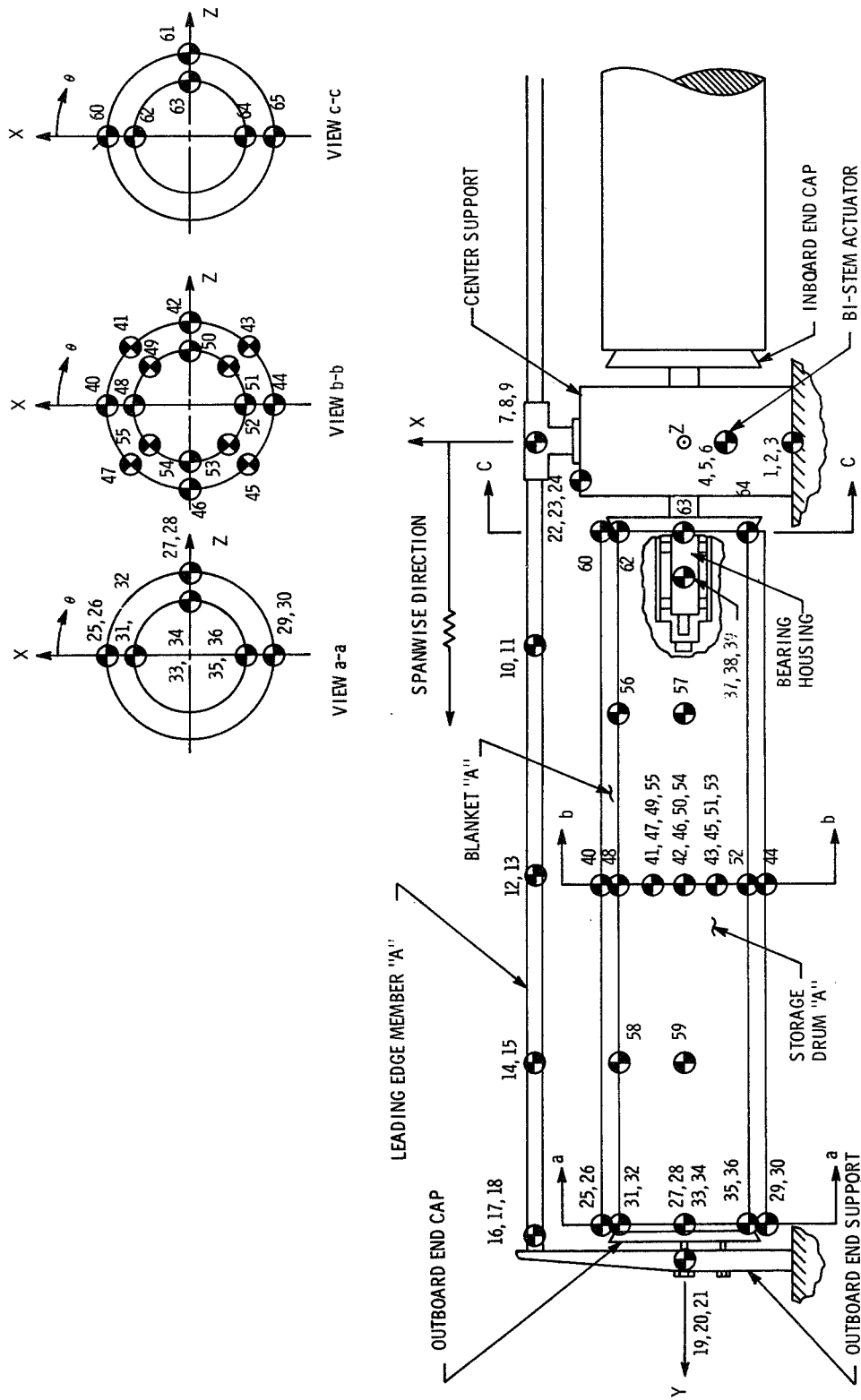


Figure 2.4-4. RA-250 Rollup Solar Array Stowed Model Test Accelerometer Locations

Data from all of these transducers shall be acquired and stored on magnetic tape for the resonance searches (Tests 1a, 2a, 3a), resonance dwells (Tests 1b, 2b, 3b), and linearity evaluation tests (Tests 1c, 2c, 3c).

Test Data Requirements

Test data shall be reduced in accordance with Table 2.4-3, in the form of linear acceleration versus log frequency plots (where applicable).

Table 2.4-3. Modal Testing Data Reduction Requirements

Description	Test	Data Requirements	Data Channels
Resonance Searches	1a, 2a, 3a	In-phase response versus frequency plots	Approximately eight channels to be selected prior to the test
		Total response versus frequency plots	
		Quadrature response at each resonance	
Resonance Dwells	1b, 2b, 3b	Quadrature response at each resonance	All Not more than eight channels, to be selected following completion of resonance search
		Response time history (following abrupt shaker stoppage)	
Linearity Evaluation	1c, 2c, 3c	In-phase response versus frequency (in vicinity of resonances)	Same channels used to yield similar data from resonance dwells
		Response time histories (following shaker stoppage)	

This test data, upon its receipt from the data reduction facility, shall undergo further analysis to transform response data into mode shapes. A matrix interpretive digital computer program (the same tool employed for structural dynamic analysis) shall be employed for this purpose. The equation of modal motion (ξ_r) under base excitation \ddot{x}_1 has the

following solution at the resonance of the rth mode (assuming that the quadrature response of that one mode predominates):

$$\ddot{\xi}_r = \frac{- [\phi_i^{(r)}]^T [m_{ij}] [\bar{\phi}_j] \ddot{x}_b}{gM_r}$$

where,

$\bar{\phi}_j$ is an array of rigid body mode shapes

M_r is the generalized mass, to be taken as unity, i. e.,

$$[\phi_i^{(r)}]^T [m_{ij}] \{\phi_j^{(r)}\} = 1$$

Since the quadrature response is:

$$\{\ddot{x}_i\}_q = \{\phi_i^{(r)}\} \ddot{\xi}_r$$

at the resonant frequency of the rth mode, it follows that:

$$\{\ddot{x}_i\}_q = \frac{- \{\phi_i^{(r)}\} [\phi_i^{(r)}]^T [m_{ij}] [\bar{\phi}_j] \ddot{x}_b}{g_r}$$

an expression from which the $\{\phi_i^{(r)}\}$ vector can be established.

In the event that modal clustering is inherent in the test data, the phase separation technique developed by Stahle (Ref 8) shall be used to separate the modes from the resulting combined

quadrature response. For a system subjected to base excitation, Stahle has shown that the measured quadrature response $[x_i(f)]_q$ at the i th station at some frequency is related to the quadrature responses $(\ddot{x}_i^{*(s)}(f))_q$ of the individual modes (S) by:

$$\begin{aligned}
 (\ddot{x}_i(f))_q &= (\ddot{x}_i^{*(1)}(f))_q \left[\frac{\left(\frac{f}{f_1}\right)^2 g_1^2}{\left(1 - \frac{f^2}{f_1^2}\right)^2 + g_1^2} \right] + \dots \\
 &+ (\ddot{x}_i^{*(s)}(f))_q \left[\frac{\left(\frac{f}{f_s}\right)^2 g_s^2}{\left(1 - \frac{f^2}{f_s^2}\right)^2 + g_s^2} \right]
 \end{aligned}$$

where, for base excitation,

$$(\ddot{x}_i^{*(s)})_q = \frac{-\phi_i^{(s)} [\phi_i^{(s)}]^T [m_{ij}] [\bar{\phi}_j] \ddot{x}_b}{g_s}$$

If r modes have been established experimentally for J stations on the structure, the matrix equation for quadrature response is then

$$\begin{bmatrix}
 (\ddot{x}_1(f_1))_q & (\ddot{x}_2(f_1))_q & \dots & (\ddot{x}_J(f_1))_q \\
 (\ddot{x}_1(f_2))_q & (\ddot{x}_2(f_2))_q & \dots & (\ddot{x}_J(f_2))_q \\
 \vdots & \vdots & \dots & \vdots \\
 (\ddot{x}_1(f_r))_q & (\ddot{x}_2(f_r))_q & \dots & (\ddot{x}_J(f_r))_q
 \end{bmatrix}$$

$$= \begin{bmatrix} 1 & \frac{(f_1/f_2)^2 g_2^2}{[1 - (f_1/f_2)^2]^2 + g_2^2} & \cdots & \frac{(f_1/f_r)^2 g_r^2}{[1 - (f_1/f_r)^2]^2 + g_r^2} \\ \frac{(f_2/f_1)^2 g_1^2}{[1 - (f_2/f_1)^2]^2 + g_1^2} & 1 & & \frac{(f_2/f_r)^2 g_r^2}{[1 - (f_2/f_r)^2]^2 + g_r^2} \\ \vdots & \vdots & \ddots & \vdots \\ \frac{(f_r/f_1)^2 g_1^2}{[1 - (f_r/f_1)^2]^2 + g_1^2} & \frac{(f_r/f_2)^2 g_2^2}{[1 - (f_r/f_2)^2]^2 + g_2^2} & \cdots & 1 \end{bmatrix} \begin{bmatrix} \ddot{x}_{1q}^{*(1)} & \cdots & \ddot{x}_{Jq}^{*(1)} \\ \ddot{x}_{2q}^{*(2)} & \cdots & \ddot{x}_{Jq}^{*(2)} \\ \vdots & \ddots & \vdots \\ \ddot{x}_{1q}^{*(r)} & \cdots & \ddot{x}_{Jq}^{*(r)} \end{bmatrix}$$

where the rows of $\ddot{x}_{iq}^{*(s)}$ and $\ddot{x}_{iq}^{(f)}$ are the individual and measured mode shapes respectively. This can be written more simply as:

$$[\ddot{x}_{iq}^{(f)}] = [c][\ddot{x}_{iq}^{*(s)}]$$

where the coupling matrix $[c]$ is dependent only on the resonant frequencies. Solving for the pertinent normal modal contributions, it follows that:

$$[c]^{-1} [\ddot{x}_{iq}^{(f)}] = [\ddot{x}_{iq}^{*(s)}].$$

Although all the measured modes could be used in this equation, it is only necessary to include those modes which are sufficiently close to cause modal interaction in the quadrature response.

In any event, a set of mode shapes shall be extracted from reduced experimental quadrature response data.

These experimental vibration characteristics shall be compared with analysis in the following manner:

1. Three dimensional plots of predicted versus measured mode shapes for each principal resonance. Predicted and measured frequencies for each mode shall also be stated on the appropriate plots.
2. Tables comparing the predicted mode shapes versus measured mode shapes for each principal resonance. To facilitate comparisons, both data shall be normalized with respect to a common displacement vector component.

In addition, curves showing the experimental variation of damping coefficients with base excitation level shall be provided for each mode of vibration.

2.5 GSE AND TEST EQUIPMENT DESIGN

2.5.1 PERFORMANCE TEST RACK

The performance test rack and associated strip chart recorder are shown in Figure 2.5-1. This rack contains the circuitry and power supplies required to operate the Bi-Stem deployable boom, to fire the outboard end support pyrotechnics, and to supply rated current through the slip ring power circuits. The strip chart recorder will be used to obtain a permanent record of the Bi-Stem current and voltage, the outboard end support release events, the upward deployment aid vertical extension, and the squib firing current and voltage.

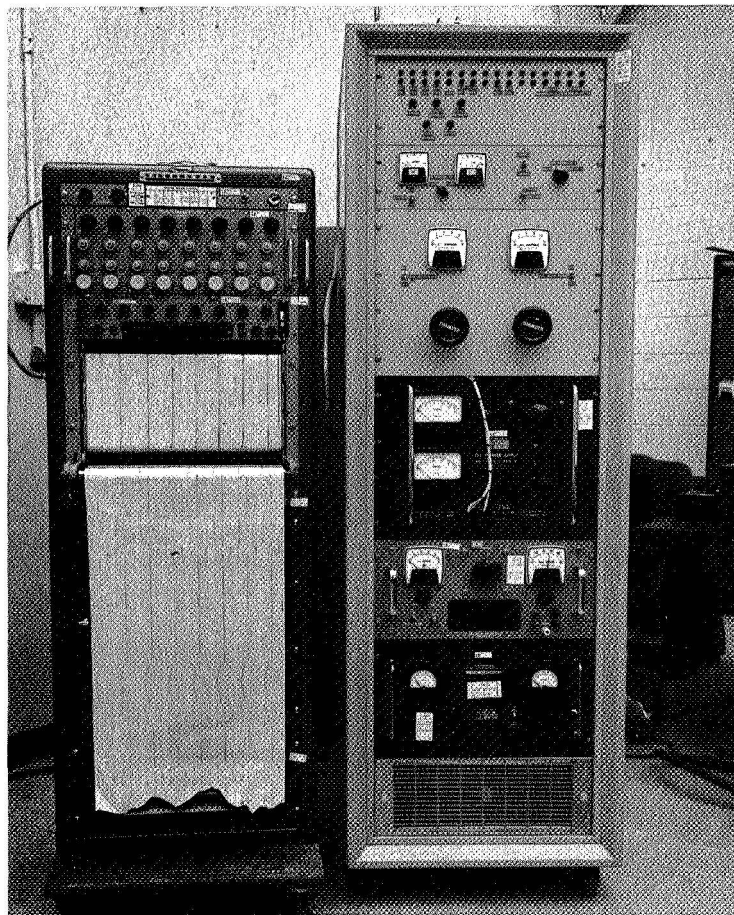


Figure 2.5-1. Performance Test Rack (VF70-127A)

Associated with this performance test equipment is a load circuit required to obtain the I-V curve for each module plus the X-Y plotter and digital voltmeters.

2.5.2 MODULE ILLUMINATOR

A solar cell module illuminator and associated ac power regulator rack will be used to illuminate each module while the I-V curve is obtained during each health check.

Figure 2.5-2 shows this equipment prior to the modification which was required to adapt it to the horizontal table. This modification consists of placing the lamp array housing on a horizontal rail system which permits the illuminator to traverse across the table at the proper elevation above the blanket. The blanket is moved beneath the illuminator in the longitudinal direction to provide both directions of motion required to illuminate each active module on the blankets.

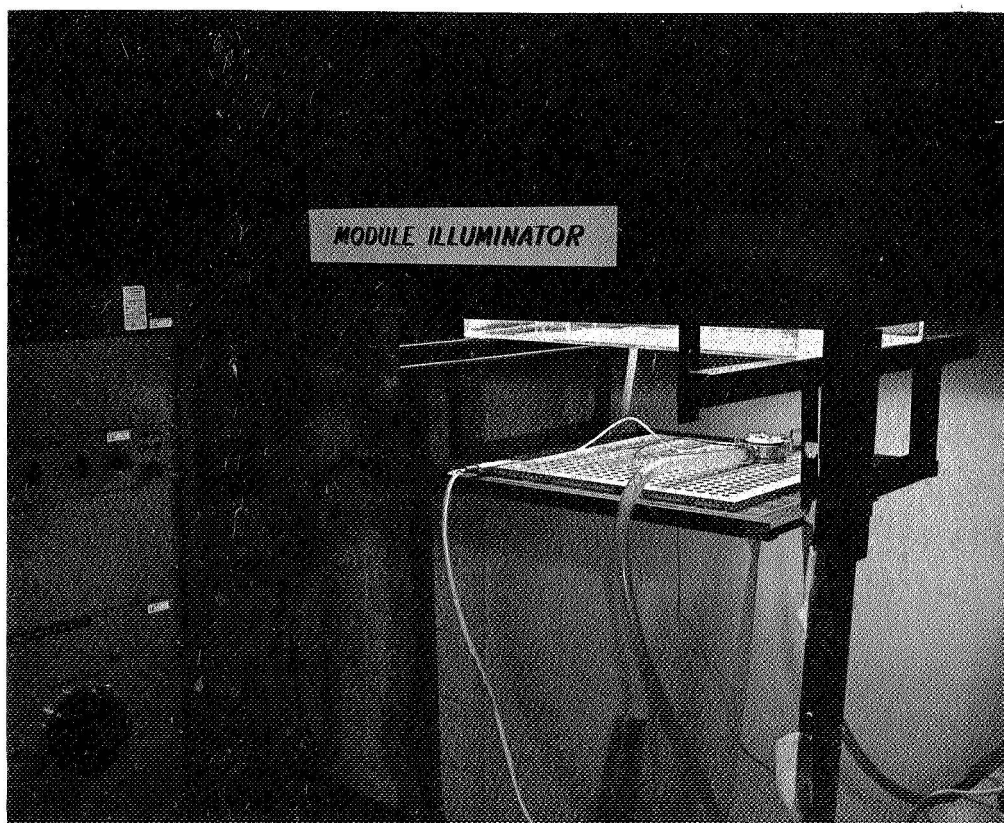


Figure 2.5-2. Module Illuminator (VF70-73H)

2.5.3 HOLDING FIXTURE

The holding fixture has been completed and has been used as the mounting base for the mechanical assembly as shown in Figure 2.2-1. Remaining activity on this fixture includes the installation of microswitches at each end support as a deployment interlock and as release event monitors.

2.5.4 DEPLOYMENT AIDS

The upward deployment aid has been assembled and is in the process of checkout at this time. This device is shown in Figure 2.5-3. It will be mounted in the performance test area at an elevation of 41 feet above the floor. In addition, this counterbalance will be utilized during the deployment tests under thermal vacuum conditions in the 54-foot chamber.

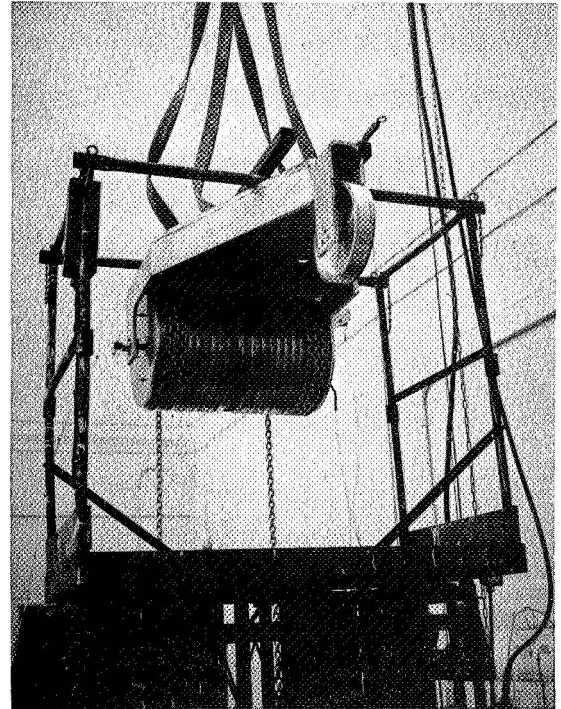
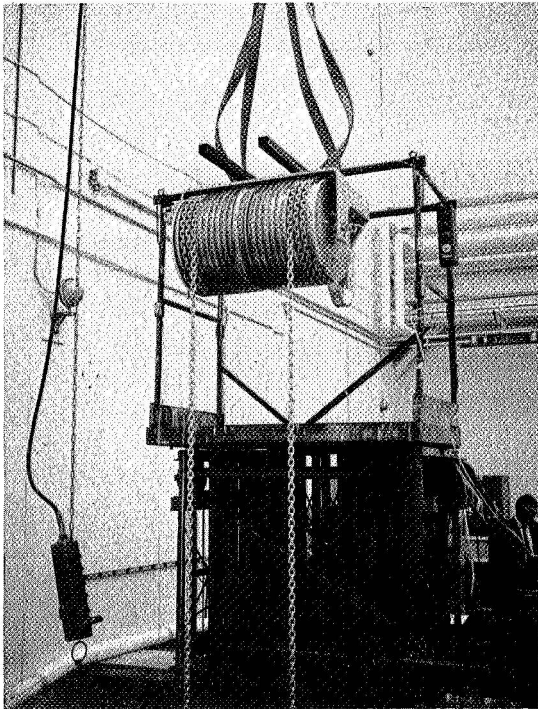


Figure 2.5-3. Upward Deployment Aid

The counterbalancing scheme utilized by this device is a falling chain with a unit weight distribution to exactly counterbalance the solar array blankets plus the Bi-Stem deployable boom. The fixed weights of the leading edge member and the strong back which supports the leading edge member is counterbalanced by fixed weights at the ends of the chains.

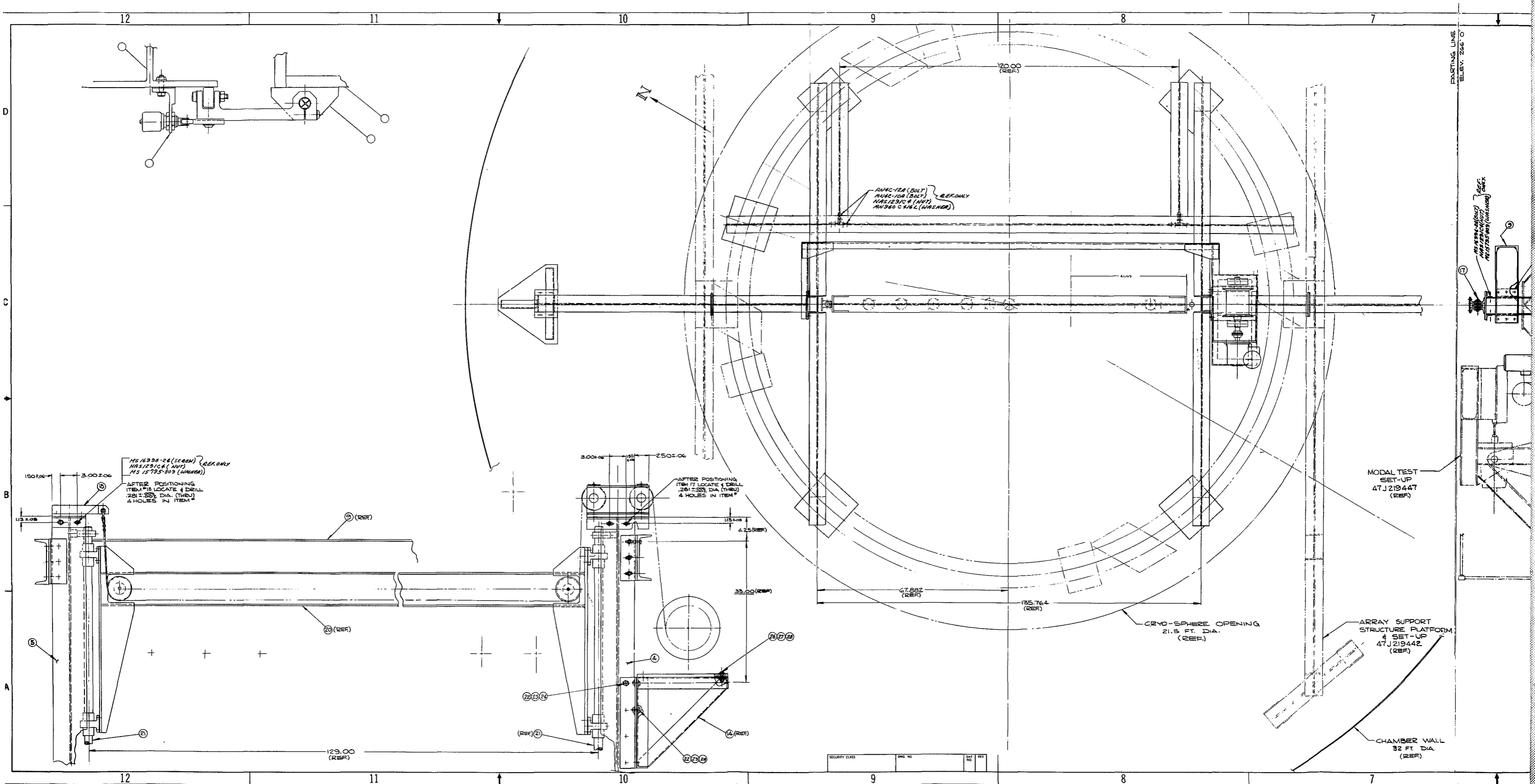
The downward deployment support is used during the deployed modal test to counterbalance the weight of the deployed blankets. This device is in the process of assembly at this time.

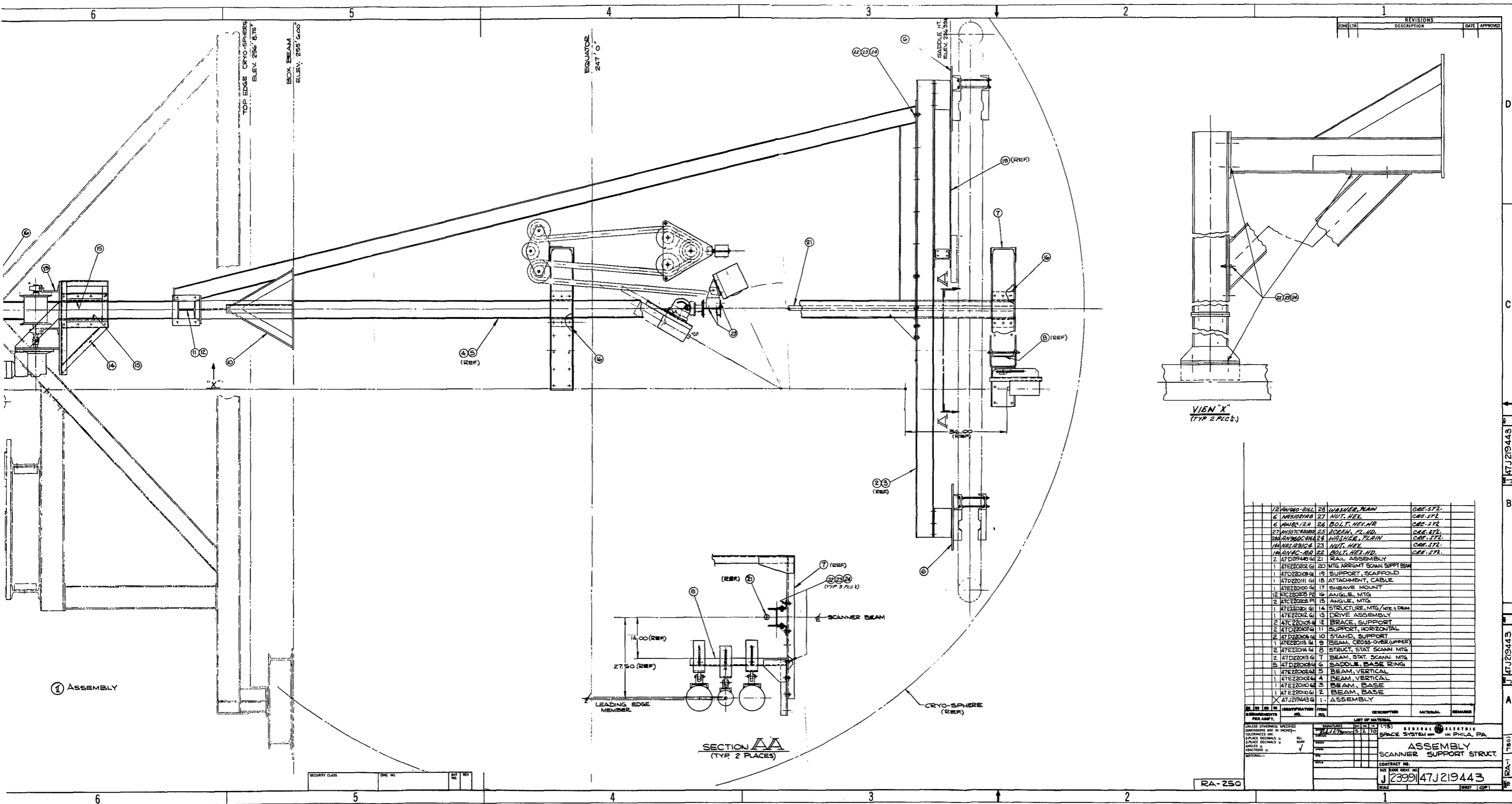
2.5.5 DEPLOYED MODAL TEST EQUIPMENT

The deployed modal test equipment consists of the structure which supports the electro-optical scanners as well as the structure which supports the array and the exciter. This installation in the 54-foot vacuum chamber is shown in Figure 2.5-4. The structure which supports the deployed array and the exciter is mounted from two existing A frames.

Figure 2.5-5 shows this structure in the process of assembly on the floor adjacent to the chamber. The A frames attach to the chamber structure such that the dome can be installed following the checkout of the test setup. The work platform which straddles the A frame supports the exciter at the center with the array mounted on the bearing table shown in Figure 2.5-6. This bearing system allows for translational motion for the out-of-plane bending tests and the in-plane tests, as well as for rotational motion required for the out-of-plane torsional tests.

The scanner support structure consists of two vertical beams which support a movable horizontal carriage which carries six electro-optical scanners. These vertical beams are mounted to the chamber base ring structure and are supported at the catwalk level by brackets. The horizontal carriage beam rides on linear bearings and is driven by a motor drive system for remote positioning at each spanwise station. The optical axis of each scanner makes an angle of 30 degrees to the plane of the blankets. Each target on the blankets is illuminated by a lamp which is associated with each scanner.





QTY	IDENTIFICATION	FROM	DESCRIPTION	MATERIAL	REMARKS
12	AN60-21L	28	WASHER, FLAT	CRS. STL.	
6	AN60-12A	27	NUT, HEL.	CRS. STL.	
6	AN60-12A	26	BOLT, HEX. NR.	CRS. STL.	
27	AN60-21A	25	ROSKN. FL. HD.	CRS. STL.	
24	AN60-21A	24	WASHER, FLAT	CRS. STL.	
14	AN60-21A	23	NUT, HEL.	CRS. STL.	
14	AN60-21A	22	BOLT, HEL. HD.	CRS. STL.	
2	ATD22014 G1	21	RAIL ASSEMBLY		
1	ATE22002 G1	20	MTG. ARRGMT. SCANN. SUPPT. BEAM		
1	ATD22010 G1	19	SUPPORT, SCAFFOLD		
1	ATD22011 G1	18	ATTACHMENT, CABLE		
1	ATE22000 G1	17	SHAVE MOUNT		
12	ATC22005 P2	16	ANGLE, MTG.		
2	ATC22005 P1	15	ANGLE, MTG.		
1	ATE22021 G1	14	STRUCTURE, MTG. W/ITE 4 DRUM		
1	ATE22012 G1	13	DRIVE ASSEMBLY		
2	ATC22015 G1	12	BRACE, SUPPORT		
2	ATD22007 G1	11	SUPPORT, HORIZONTAL		
2	ATD22006 G1	10	STAND, SUPPORT		
1	ATE22015 G1	9	BEAM, CROSS-OVER (UPPER)		
2	ATE22014 G1	8	STRUCT. STAT. SCANN. MTG.		
2	ATD22013 G1	7	BEAM, STAT. SCANN. MTG.		
5	ATD22004 G1	6	SADDLE, BASE RING		
1	ATE22002 G1	5	BEAM, VERTICAL		
1	ATE22002 G1	4	BEAM, VERTICAL		
1	ATE22010 G1	3	BEAM, BASE		
1	ATE22010 G1	2	BEAM, BASE		
1	ATE22010 G1	1	ASSEMBLY		

UNLESS OTHERWISE SPECIFIED DIMENSIONS ARE IN INCHES—
TOLERANCES ON:
SPACE DIMENSIONS ± .005
HOLE DIMENSIONS ± .005
FRACTIONS ± .005
DECIMALS ± .005

DATE: 12/17/75
BY: J. J. [Signature]
CHECKED: [Signature]
DESIGNED: [Signature]
DRAWN: [Signature]

SCALE: 1" = 1'-0"

CONTRACT NO. J23991
SHEET 1 OF 1

GENERAL ELECTRIC SPACE SYSTEM DIV. PHILA., PA.
**ASSEMBLY
SCANNER SUPPORT STRUCT.**

RA-250

Figure 2.5-4. Deployed Model Test Equipment Installation

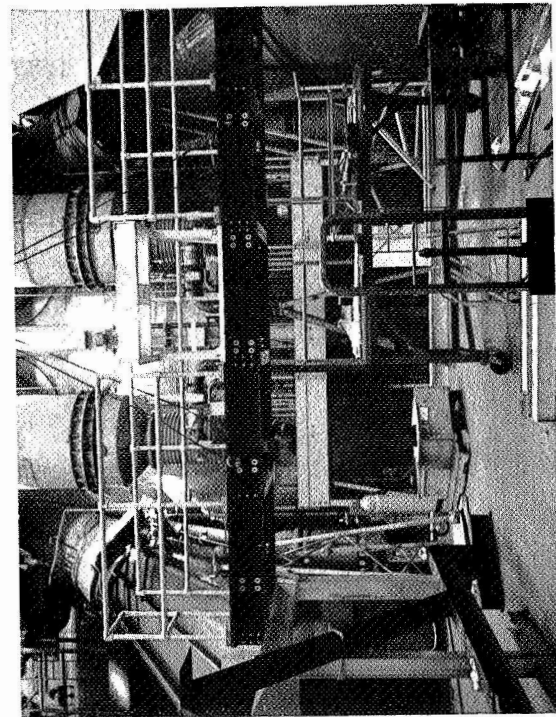
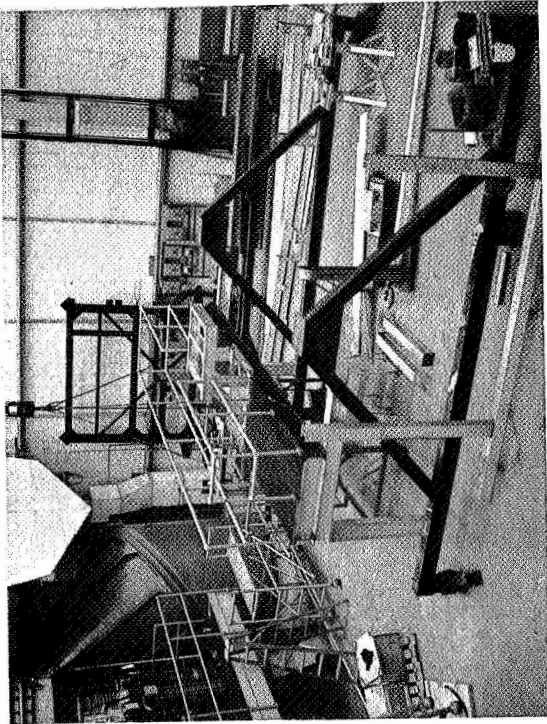


Figure 2.5-5. Modal Support Structure



Figure 2.5-6. Deployed Modal Test Support Fixture

SECTION 3
CONCLUSIONS

The following conclusions have resulted from the fourth quarter effort on the design and development of the 30-watt per pound rollup subsolar array:

1. The weight goal of 30 watts per pound was achieved. All elements of the system were completed and weighed with the total weight of the system being 82.5 pounds compared to the weight goal of 83.3 pounds. Design changes that would decrease the total weight 5.0 pounds have been identified.
2. It was possible to incorporate solar cell modules assembled with conventional interconnects and assembly techniques on the solar array blankets. The blankets have been rolled temporarily on shop aids of the same diameter as the drums in the test unit. No damage was noted.

SECTION 4
RECOMMENDATIONS

There are no specific or pending recommendations at this time. Technical aspects of the program have been discussed in the other sections of this report.

SECTION 5
NEW TECHNOLOGY

No items of new technology have been reported during this period.

SECTION 6
REFERENCES

1. "Quarterly Report No. 2, - Rollup Subsolar Array," GE-SSO Report No. 69SD4351, September 15, 1969.
2. "Quarterly Report No. 3, - Rollup Subsolar Array," GE-SSO Report No. 69SD4373, December 15, 1969.
3. Schmidt, Fox, and Bogner, "The Generation of Inter-element-Compatible Stiffness and Mass Matrices by the use of Interpolation Formulas," AFFDL-TR-66-80, November 1966.
4. "Gravity Gradient Rod Thermal Bending Test Report," GE Document No. 64SD4368, October 23, 1964.
5. "Gravity Gradient Rod Thermal Bending Test Report," GE Document No. 63SD725, July 10, 1963.
6. "Final Report - Feasibility Study of 30 Watts per Pound Rollup Solar Array", GE Document No. 68SD4301, June 21, 1968.
7. Alley, V. L. ; and Leadbetter, S. A. , "Prediction and Measurement of Natural Vibrations of Multistage Launch Vehicles," AIAA, Vol. 1, No. 2, p. 377, February 1963.
8. Stahle, C. V. Jr. , "A Phase Separation Technique for the Experimental Determination of Normal Modes of Vibration of Flight Vehicles," Shock and Vibration Bulletin, No. 40, 1961.

APPENDIX A
DERIVATION OF FLEXIBILITY INFLUENCE COEFFICIENTS
FROM LOAD DEFLECTION TEST DATA

Loadings will be applied separately at the two drum extremities. Both conditions are essential for determining bearing assembly flexibility influence coefficients here (where the drums are substantially stiffer than the bearing assemblies). First, applying loads F_A at the outboard ends of the drums, it follows that (through symmetry):

$$\delta_A = \delta_D; \delta_B = \delta_C; \theta_B = -\theta_C$$

Also, with the drums far stiffer than the bearing assembly (i. e., assumed to be rigid here-in):

$$\theta_B = \frac{\delta_A - \delta_B}{L}$$

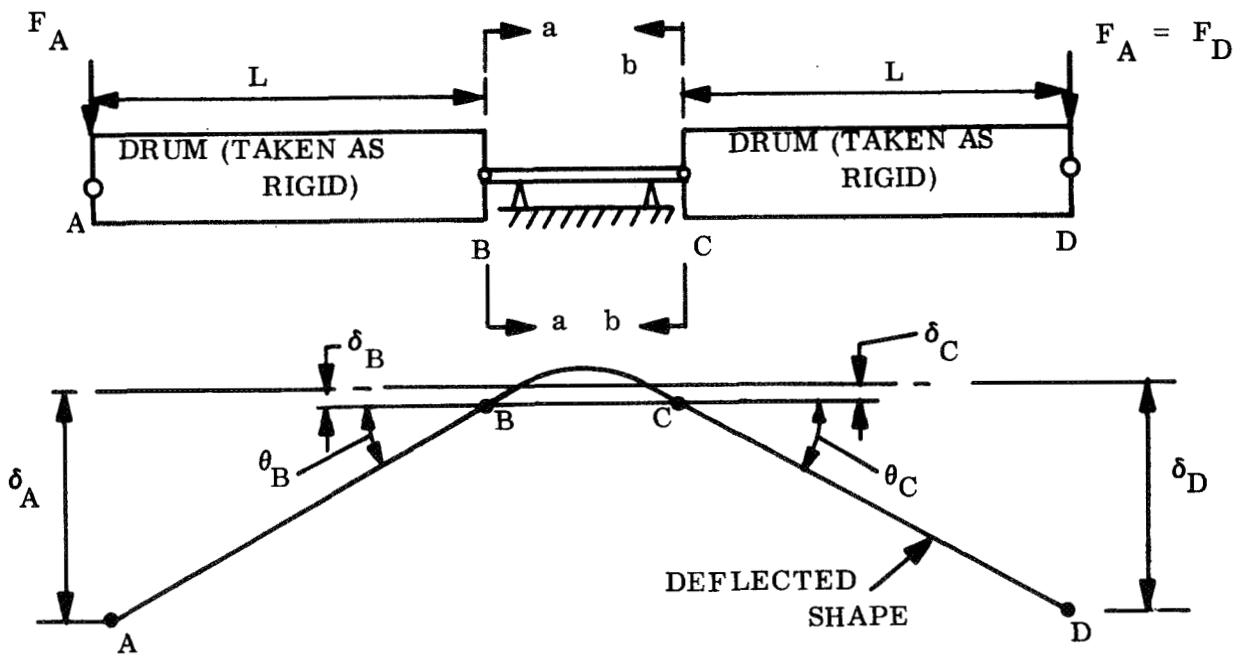


Diagram of Drums, Bearings, and Center Shaft with Symmetric Loading

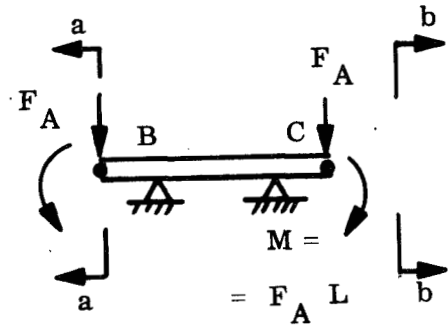
For the flexible element, i. e. , the assembly BC as shown, it follows that

$$\left\{ \begin{array}{l} \delta_B = F_A C_{\delta_B, F} + MC_{\delta_B, M} \\ \theta_B = F_A C_{\theta_B, F} + MC_{\theta_B, M} \end{array} \right.$$

Also, from Betti's theorem,

$$C_{\theta_B, F} = C_{\delta_B, M}$$

$$M = F_A L$$



Free Body Diagram of
of Flexible Element
(Assembly BC)

and from the sketch

$$M = F_A \cdot L$$

This yields, then, the following two simultaneous equations with three unknowns, the flexibility influence coefficients $C_{\delta_B, F}$, $C_{\delta_B, M}$ and $C_{\theta_B, M}$:

$$\delta_B = F_A C_{\delta_B, F} + F_A \cdot L C_{\delta_B, M} \quad (A1)$$

$$\theta_B = F_A C_{\theta_B, M} + F_A \cdot L C_{\theta_B, M} = \frac{\delta_A - \delta_B}{L} \quad (A2)$$

The necessary third equation can be established from data acquired during the second test - applying loads F_B at the inboard drum extremities (Points B and C). The resulting deflection δ_B^* at B is related to the force F_B by:

$$\delta_B^* = C_{\delta_B, F} F_B \quad (A3)$$

Here, F_B , δ_B , δ_A , δ_B^* and F_A are experimentally measured quantities. L is known from the array geometry.

Therefore, equations (A1), (A2) and (A3) can be solved simultaneously to yield:

$$C_{\delta_B, F}; C_{\delta_B, M} = C_{\theta_B, F}; C_{\theta_B, M}$$

APPENDIX B
CALCULATION OF FLEXIBILITY INFLUENCE COEFFICIENTS
FROM LOAD DEFLECTION TEST DATA

B.1 BEARING ASSEMBLY FLEXIBILITY DATA

Evaluation of test data covering both the X-axis and Z-axis symmetric loading tests, show that results of both tests can be well represented (within $\pm 10\%$) by

$$\delta_A \approx \delta_D \approx 0.100 \text{ inch,}$$

for $F_A = F_D = 20 \text{ lb}$

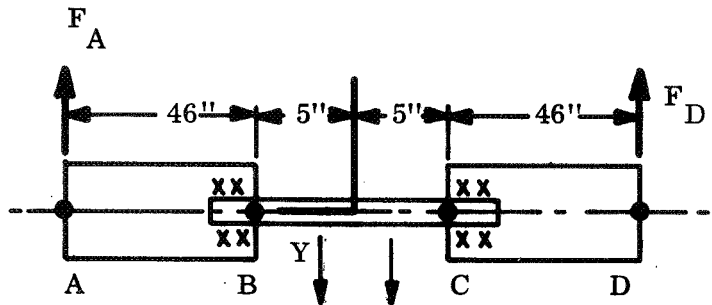
Also,

$$\delta_B = \delta_C = 0, \text{ for } F_A = 20 \text{ lb}$$

$$\text{and } F_D = 20 \text{ lb}$$

$$\delta_B^* = \delta_C^* = 0, \text{ for loadings applied}$$

$$\text{at B and C.}$$



Drums, Bearings, and Center Shaft

From derivations and assumptions in Appendix A,

$$\theta_B = \frac{\delta_A - \delta_B}{L} = \frac{0.1 - 0}{46} = 2.175 (10^{-3}) \text{ radians}$$

$${}^C \delta_{B,F} \approx 0$$

$${}^C \delta_{B,M} = {}^C \theta_{B,F} = \frac{\delta_B}{F_A \cdot L}; \quad {}^C \theta_{B,M} = \frac{\theta_B}{F_A \cdot L} = \frac{{}^C \delta_{B,M}}{L}$$

Thus, for the RA-250 bearing assembly,

$${}^C \delta_{B,F} = 0$$

$$C_{\delta_B, M} = C_{\theta_B, F} = 1.088 (10^{-4}) \text{ rad/lb}$$

$$C_{\theta_B, M} = 2.365 (10^{-6}) \text{ rad/in. -lb}$$

To provide a check, compare $C_{\theta_B, M}$ value with joint rotation constants of Alley and Leadbetter Bearing assembly does not exhibit looseness or "free-play," per test data. Therefore, it must be put in the "moderate joint" category. For an effective 3.75 inch bearing assembly diameter, the joint rotation constant is $\sim 2 \times 10^{-6}$ rad/in. -lb (very good correlation for $C_{\theta_B, M}$).

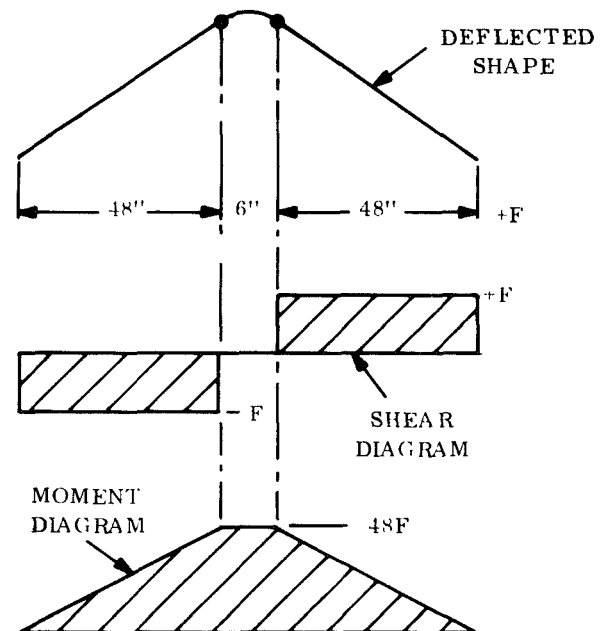
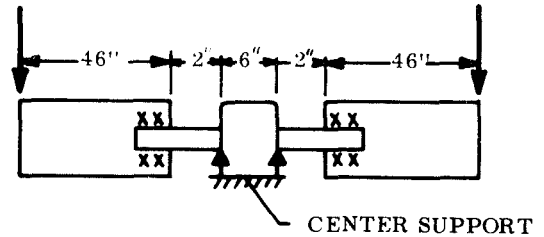
B. 2 CENTER SUPPORT FLEXIBILITY DATA

B. 2. 1 MEANS OF EXTRAPOLATING TEST DATA

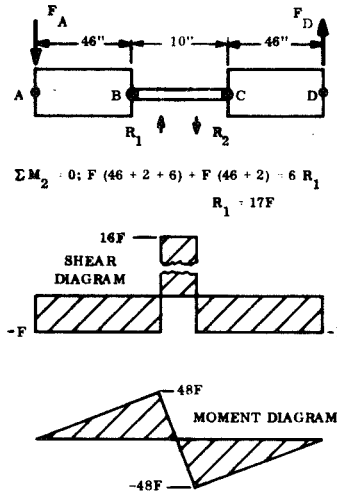
1. Data acquired during the symmetric loading tests reflects bearing assembly flexibility effects alone, i. e., does not include center support flexibility effects.

Per the deflected shape, shear diagram and moment diagram for the symmetric case, moments from either side cancel each other out at center support. The center support, in reacting forces, exhibits an axial load (L/AE) flexibility which is extremely low. Consequently, this negligible effect does not enter into symmetric loading test results.

2. In contrast, data obtained during the antisymmetric loading tests reflects both bearing assembly and center support flexibility effects.



The shear diagram, moment diagram and deflection curve for the anti-symmetric loading case, are as shown.



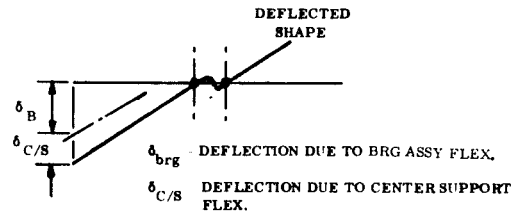
The deflection curve has a point of counterflexure at the center, as a result of center support flexibility effects (under the couple produced by reactive forces R_1 and R_2).

It thus follows (per nomenclature defined in sketch), that

$$\delta_{total} = \delta_{brg} + \delta_{C/S}$$

Also, with very stiff drums,

$$\theta_{total} = \theta_{brg} + \theta_{C/S}$$



Drum, Bearings and Center Shaft

B. 2. 2 APPLICATION OF TEST DATA

Evaluation of test data covering both the X-axis and Z-axis antisymmetric loading tests, show that the results of both tests can be well represented (within $\pm 7.5\%$) by:

$$\delta_A \approx \delta_D \approx 0.148 \text{ inch, for } F_A = 20 \text{ lb, } F_D = -20 \text{ lb}$$

Also,

$$\delta_B = \delta_C = 0, \text{ for } F_A = 20 \text{ lb, } F_D = -20 \text{ lb}$$

$$\delta_B = \delta_C = 0, \text{ for loadings applied at B and C}$$

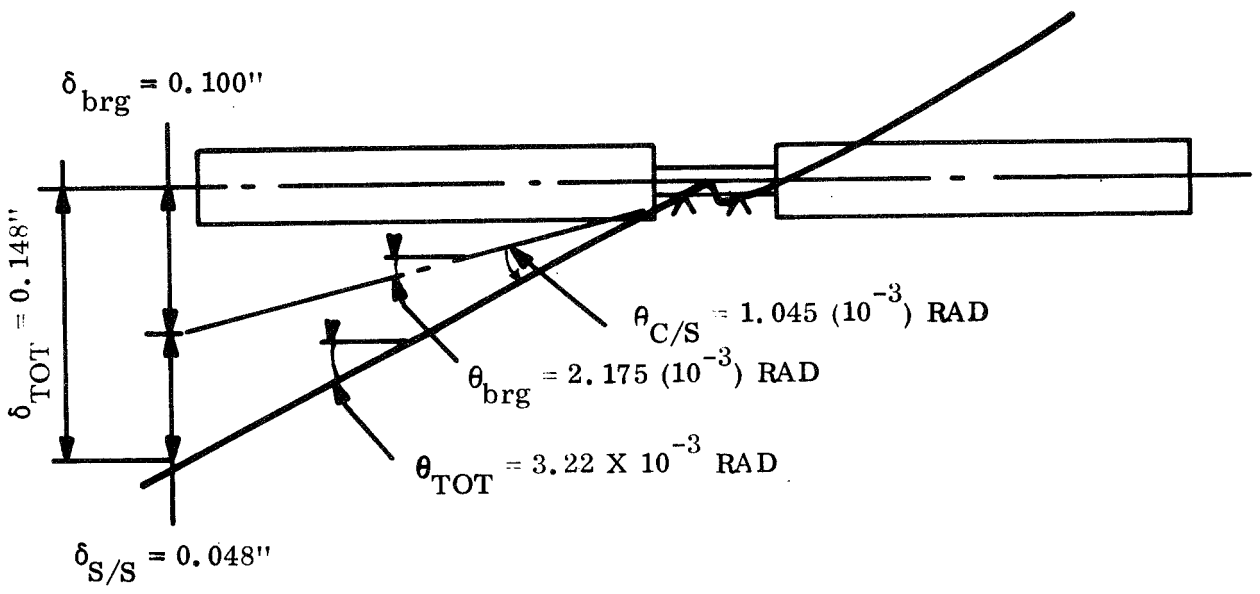
From derivations and assumptions in Appendix A,

$$\theta_B = \frac{\delta_A - \delta_B}{L} = \frac{0.148}{46} = 3.22 (10^{-3}) \text{ rad.}$$

Taking the antisymmetric test results as total values, and the symmetric loading (20 lb forces) test results as the bearing assembly-induced deformations, it follows that

$$\theta_{TOT} = 3.22 (10^{-3}) \text{ rad}; \theta_{brg} = 2.175 (10^{-3}) \text{ rad}$$

$$\delta_{TOT} = 0.148 \text{ in.}; \delta_{brg} = 0.100 \text{ in.}$$



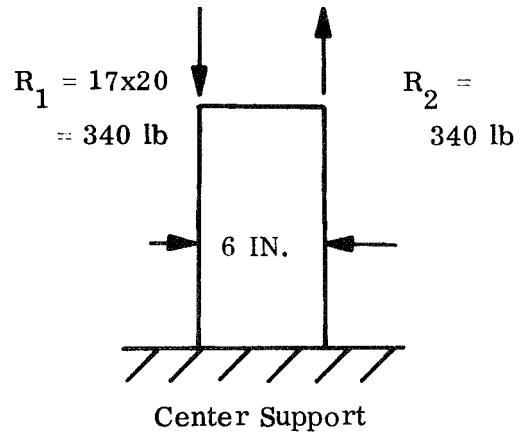
$$\therefore \delta_{C/S} = \delta_{TOT} - \delta_{brg} = 0.048 \text{ inch}$$

$$\theta_{C/S} = \theta_{TOT} - \theta_{brg} = 1.045 (10^{-3}) \text{ rad}$$

The loadings at the center support due to the 20-lb applied antisymmetric forces are as shown. The net moment is

$$M = 340 \text{ lb} \times 6 \text{ inches}$$

$$= 2040 \text{ in. -lb}$$



Now

$$\theta_{C/S} = M (C_{\theta, M})_{C/S}$$

Thus, the bending flexibility coefficient for the center support is

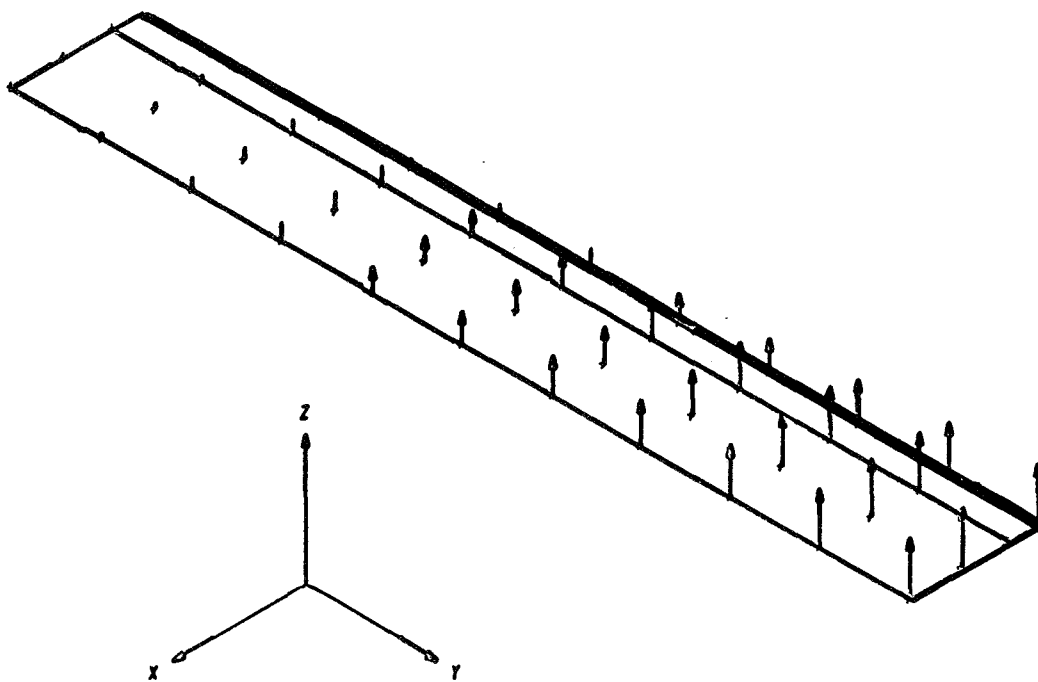
$$(C_{\theta, M})_{C/S} = \frac{1.045 (10^{-3})}{2040} = 5.12 (10^{-7}) \text{ rad/in. lb}$$

APPENDIX C
SYMMETRIC MODE SHAPES
26 FT LENGTH

(NOTE: ONLY HALF OF SYSTEM SHOWN)

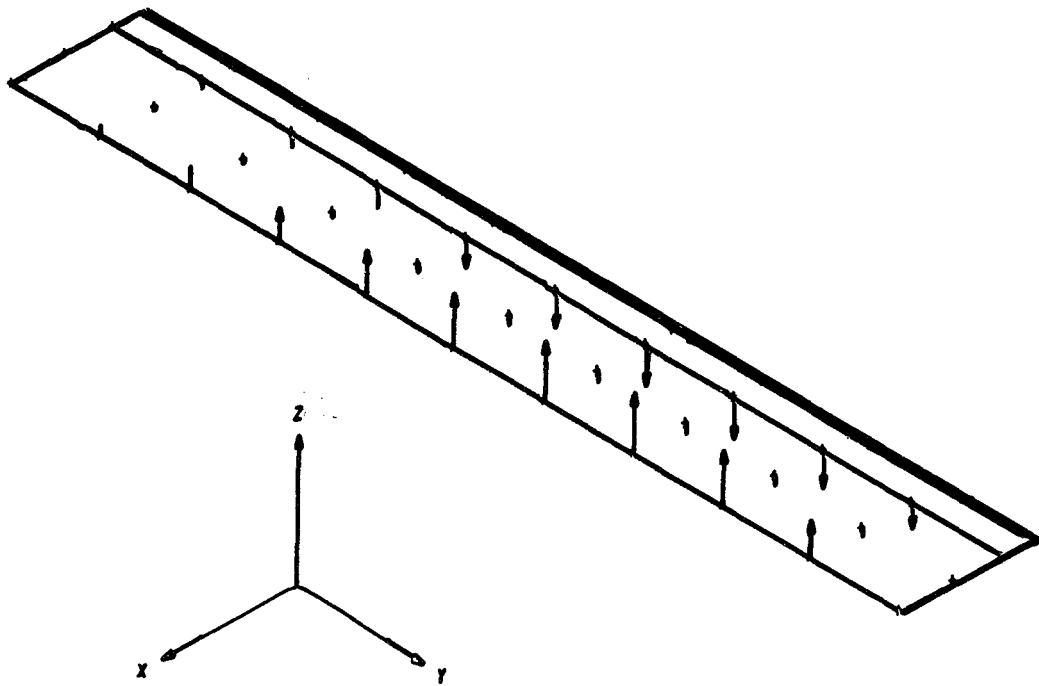
SYMMETRICAL MODE - ONE G - 26 FT.
DISCRETIZATION - 10 LONG BY 2 WIDE

MODE NUMBER 1
FREQUENCY 0.24798 Hz



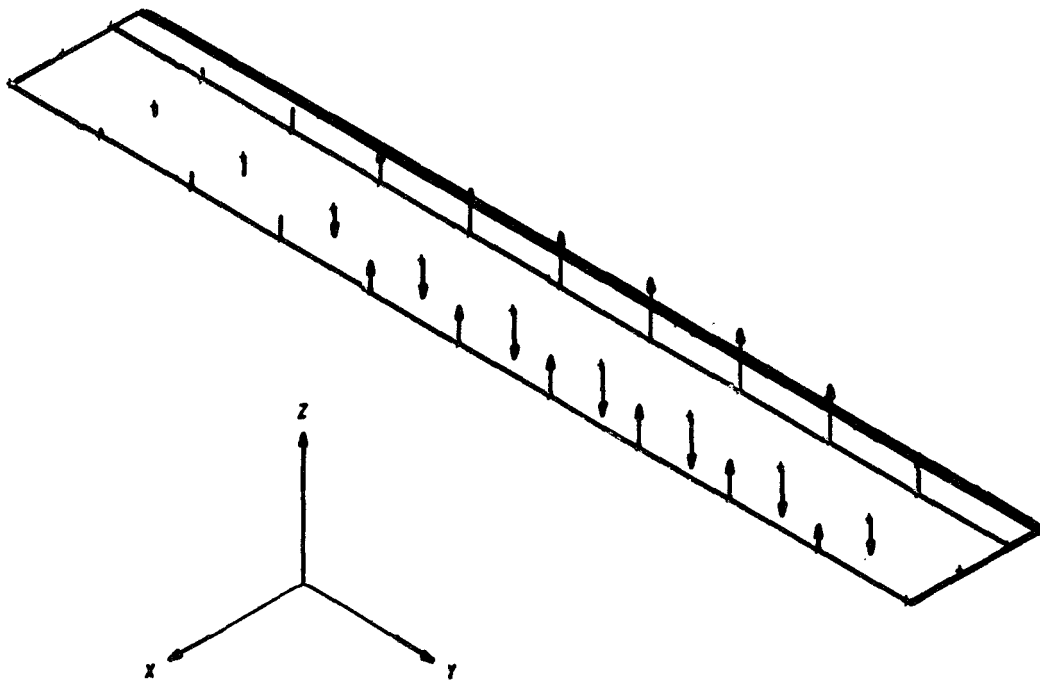
SYMMETRICAL MODE -ONE G-26 FT.
DISCRETIZATION -10 LONG BY 2 WIDE

MODE NUMBER 2
FREQUENCY 0.39211 Hz



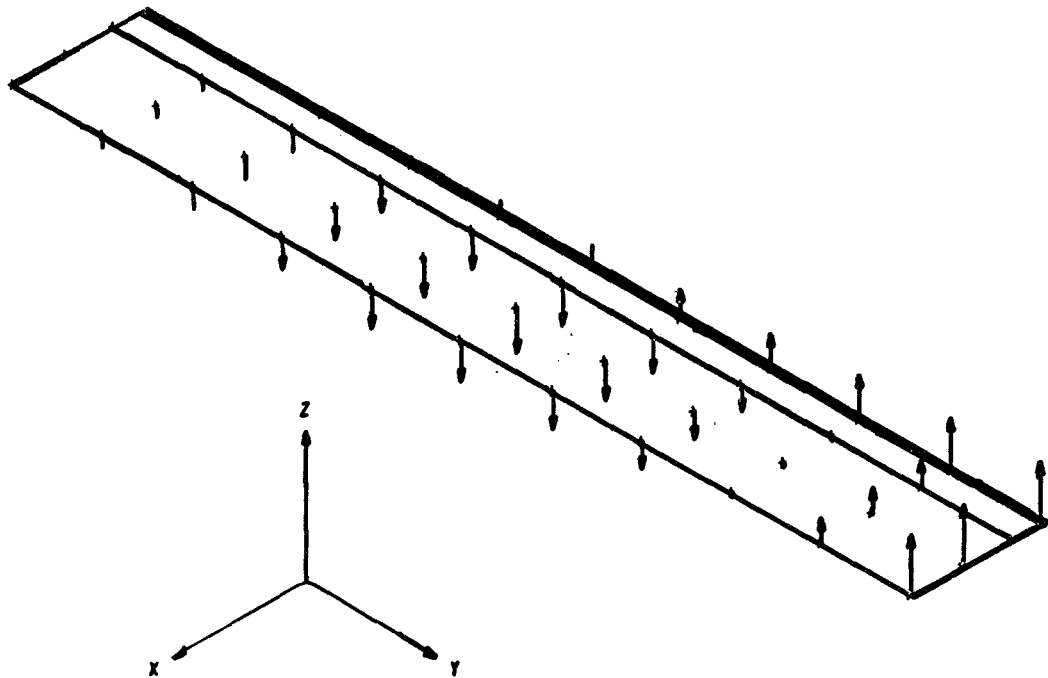
SYMMETRICAL MODE-ONE G-26 FT.
DISCRETIZATION-10 LONG BY 2 WIDE

MODE NUMBER 3
FREQUENCY 0.39215 Hz



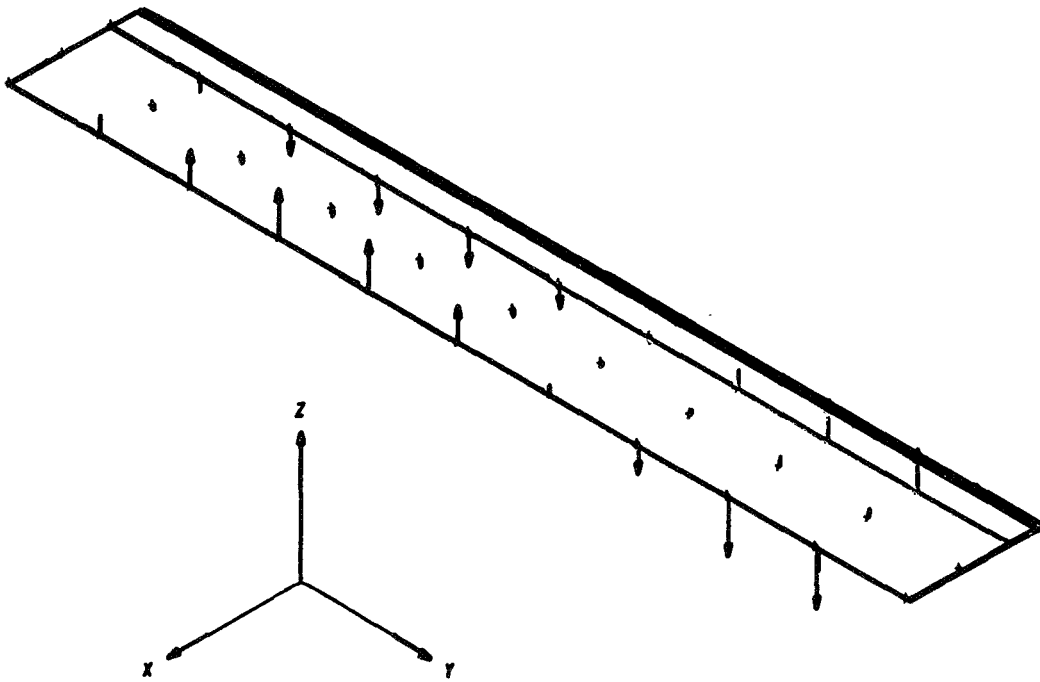
SYMMETRICAL MODE-ONE G-26 FT.
DISCRETIZATION-10 LONG BY 2 WIDE

MODE NUMBER 4
FREQUENCY 0.56119 Hz



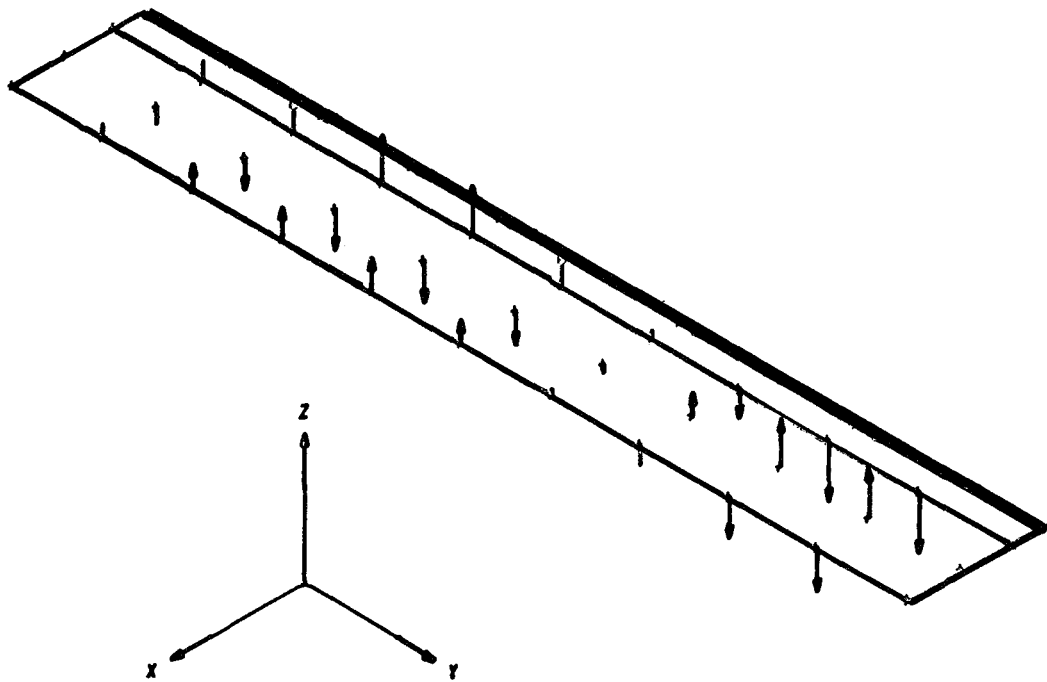
SYMMETRICAL MODE-ONE G-26 FT.
DISCRETIZATION-10 LONG BY 2 WIDE

MODE NUMBER 5
FREQUENCY 0.89652 Hz



SYMMETRICAL MODE-ONE G-26 FT.
DISCRETIZATION-10 LONG BY 2 WIDE

MODE NUMBER 6
FREQUENCY 0.89699 Hz



APPENDIX D

ANTISYMMETRIC MODE SHAPES 26 FT LENGTH

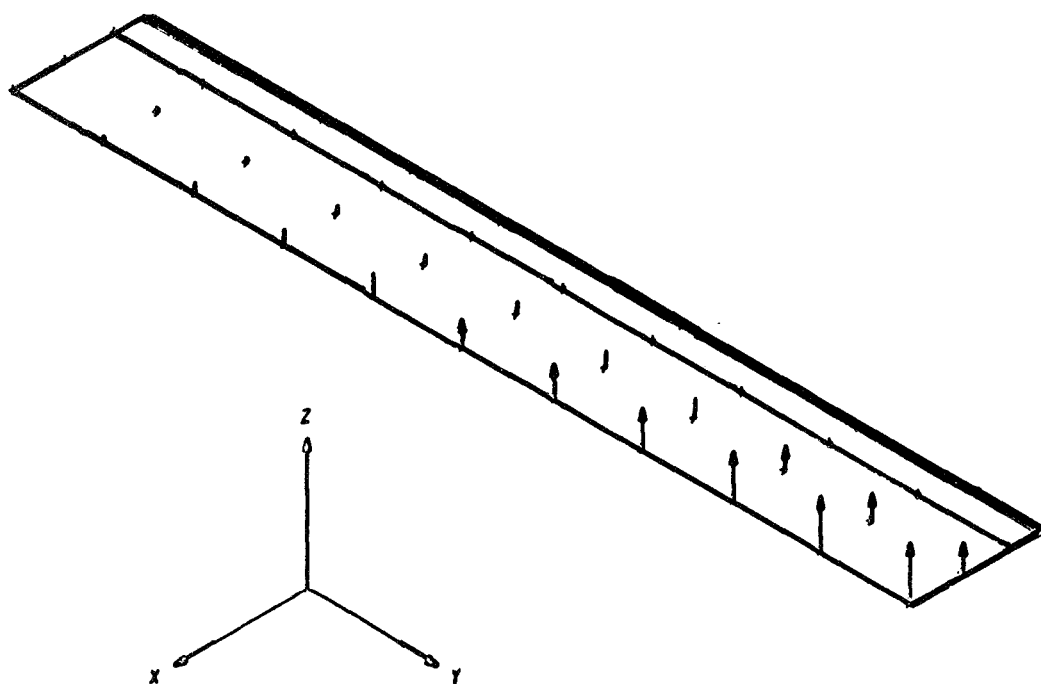
(NOTE: ONLY HALF OF SYSTEM SHOWN)

ANTISYMMETRIC MODE - ONE G- 26 FT.

DISCRETIZATION - 10 LONG BY 2 WIDE

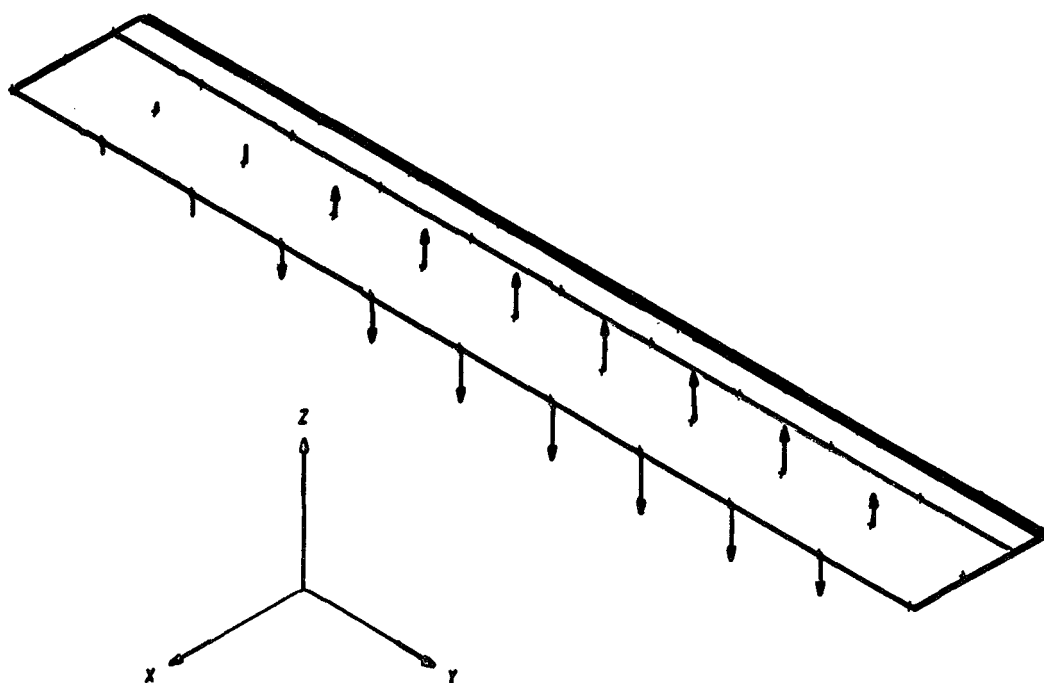
MODE NUMBER 1

FREQUENCY 0.23159 Hz



· ANTISYMMETRIC MODE - ONE G - 26 FT.
DISCRETIZATION 10 LONG BY 2 WIDE

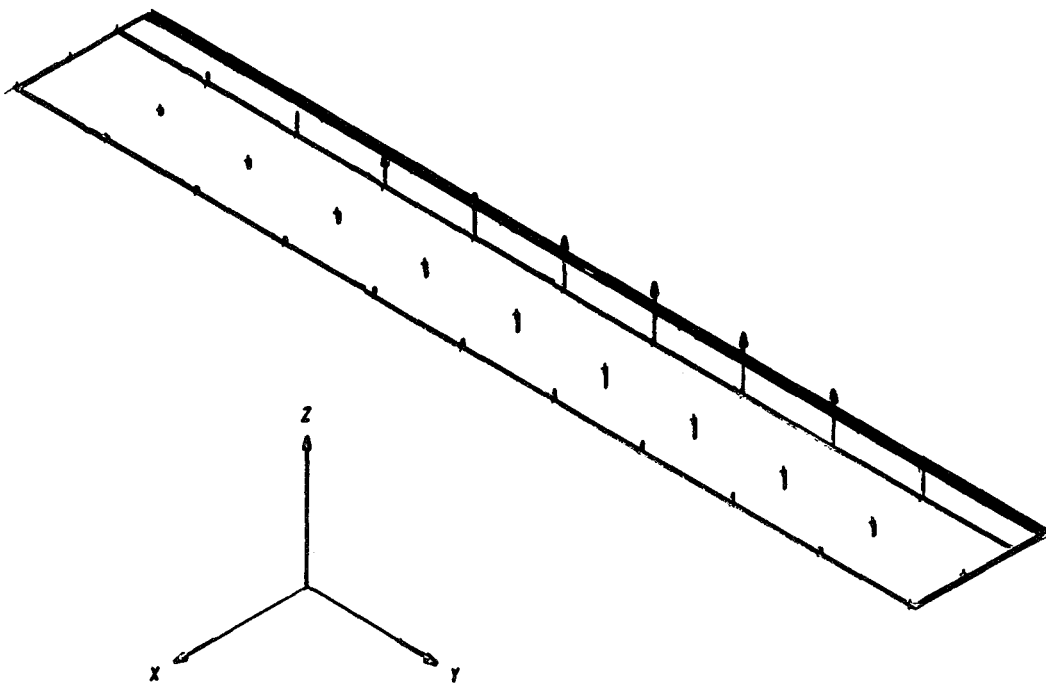
MODE NUMBER 2
FREQUENCY 0.39214 Hz



• ANTISYMMETRIC MODE - ONE G - 26 FT.
DISCRETIZATION 10 LONG BY 2 WIDE

MODE NUMBER 3

FREQUENCY 0.39215 Hz

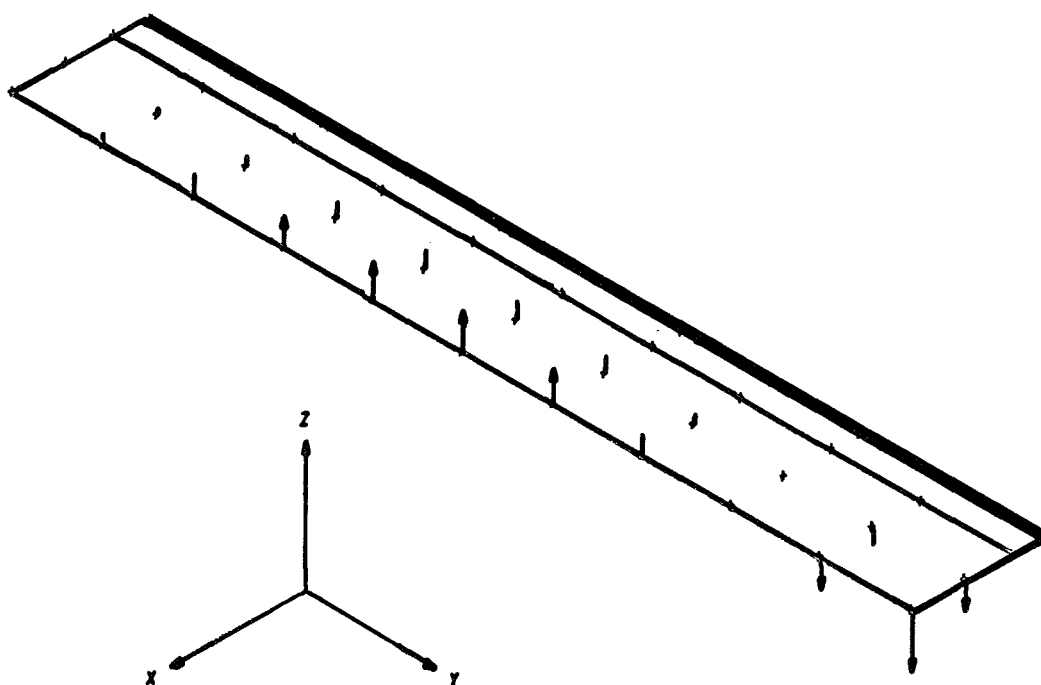


ANTISYMMETRIC MODE - ONE G - 26 FT.

DISCRETIZATION - 10 LONG BY 2 WIDE

MODE NUMBER 4

FREQUENCY 0.57960 Hz

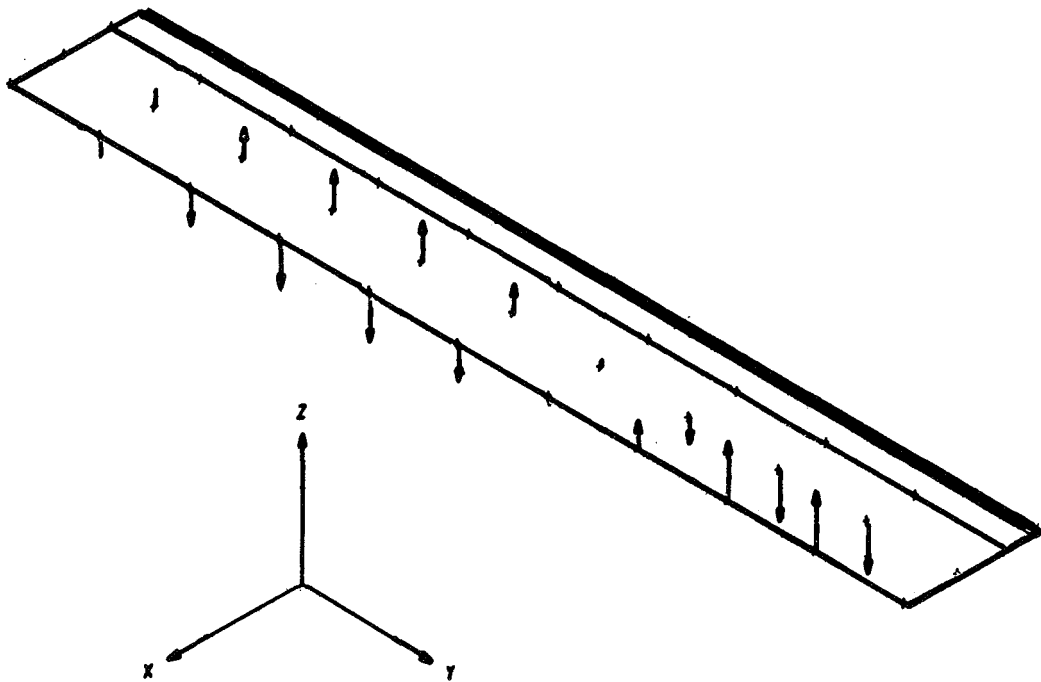


ANTISYMMETRIC MODE - ONE G - 26 FT.

DISCRETIZATION - 10 LONG BY 2 WIDE

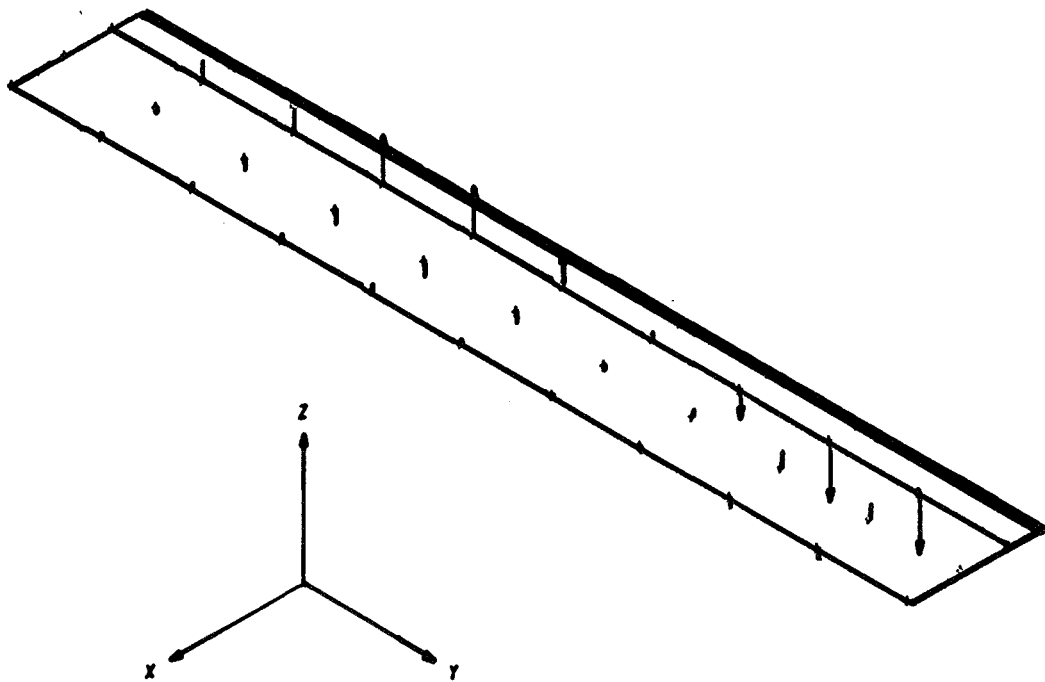
MODE NUMBER 5

FREQUENCY 0.89660 Hz



ANTISYMMETRIC MODE - ONE G - 26 FT.
DISCRETIZATION - 10 LONG BY 2 WIDE

MODE NUMBER 6
FREQUENCY 0.89661 Hz

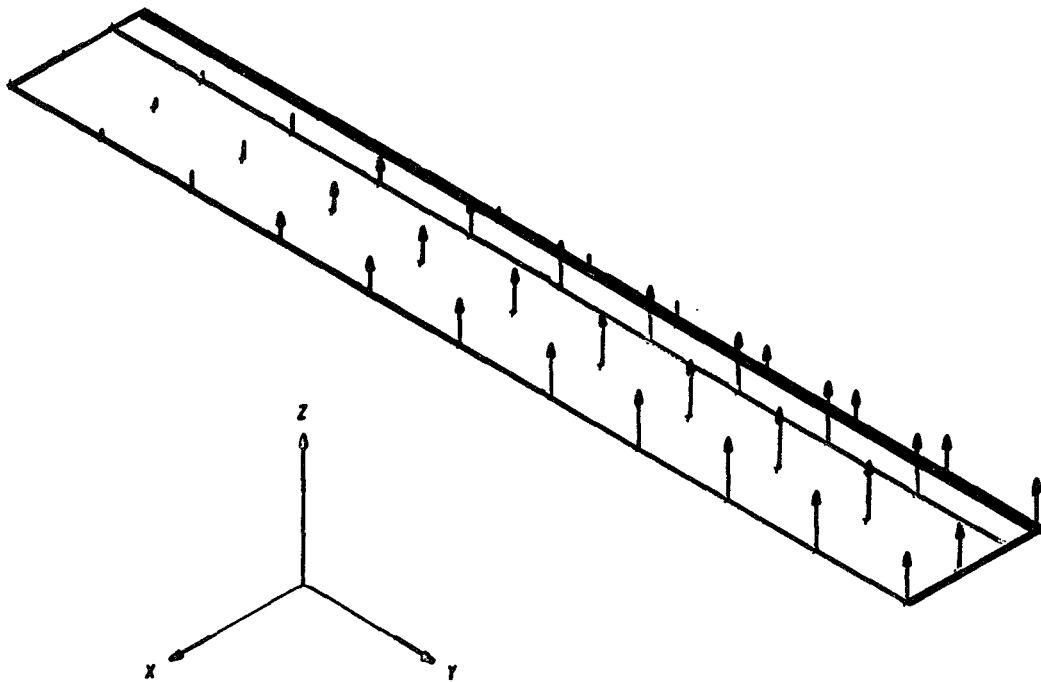


APPENDIX E
SYMMETRIC MODE SHAPES
13 FT LENGTH

(NOTE: ONLY HALF OF SYSTEM SHOWN)

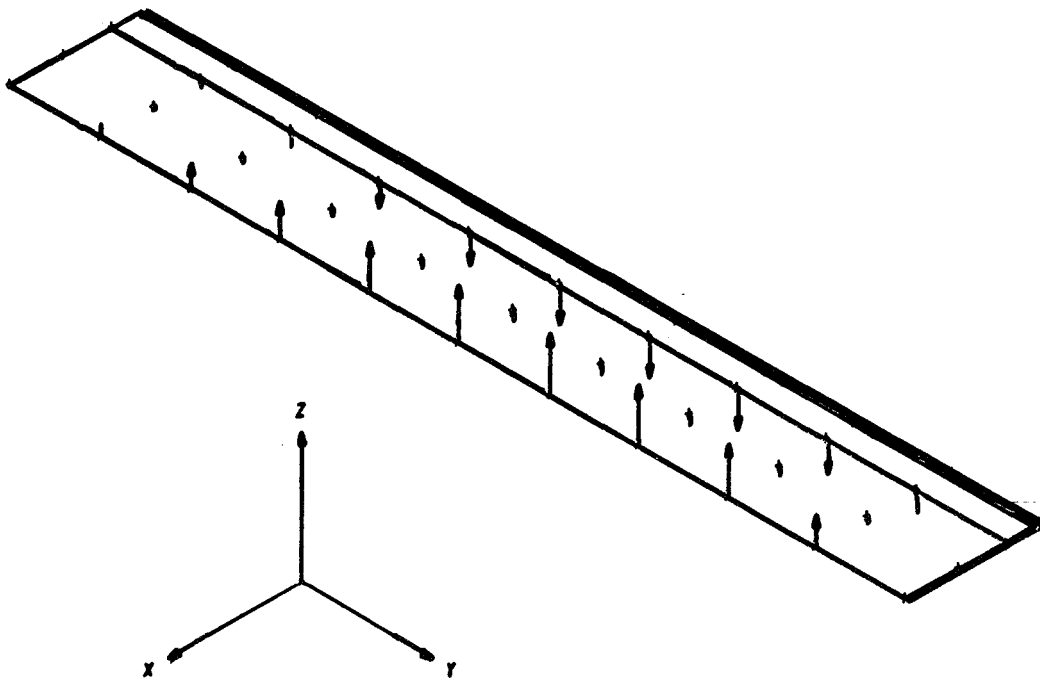
· SYMMETRICAL MODE ONE G - 13 FT.
DISCRETIZATION - 10 LONG BY 2 WIDE

MODE NUMBER 1
FREQUENCY 0.41792 Hz



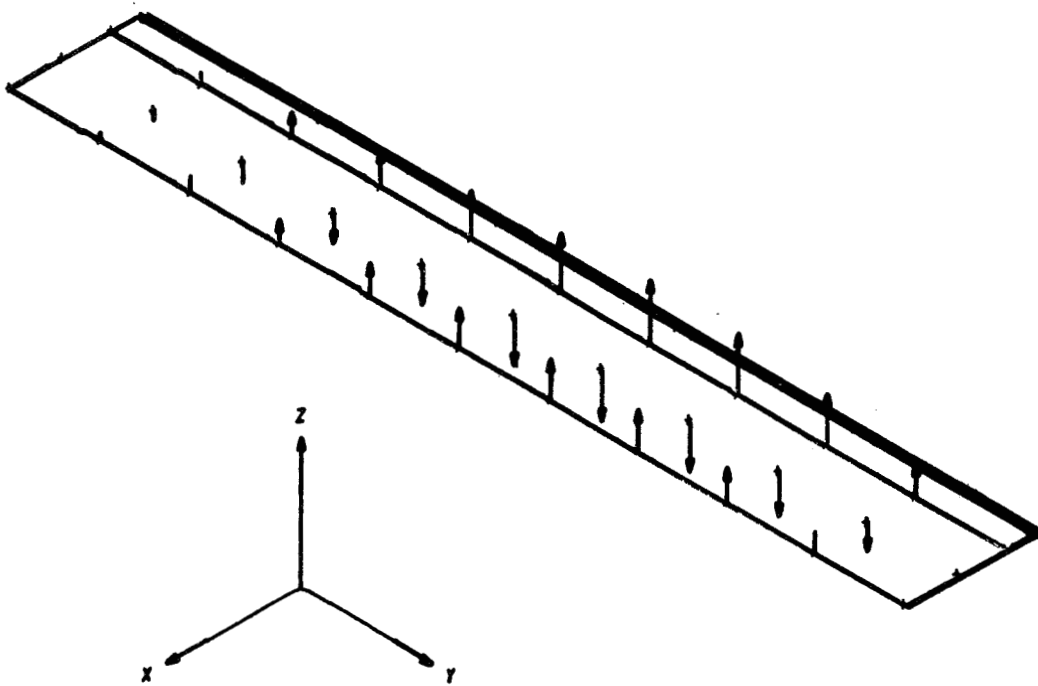
SYMMETRICAL MODE ONE G - 13 FT.
DISCRETIZATION - 10 LONG BY 2 WIDE

MODE NUMBER 2
FREQUENCY 0.55134 Hz



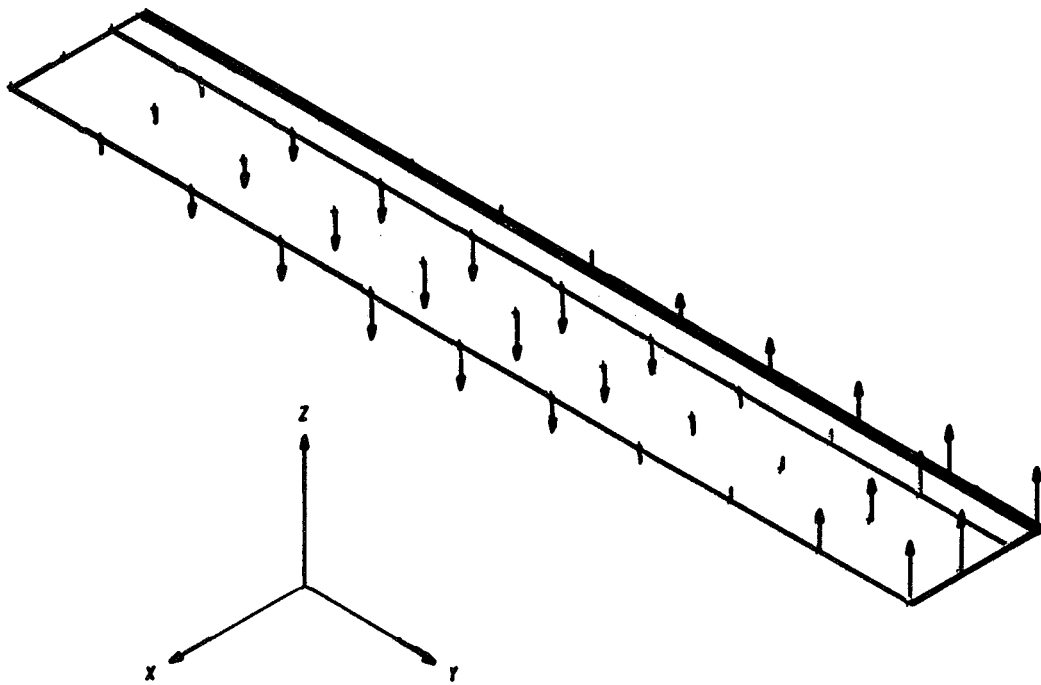
SYMMETRICAL MODE - ONE G - 13 FT.
DISCRETIZATION - 10 LONG BY 2 WIDE

MODE NUMBER 3
FREQUENCY 0.55149 Hz



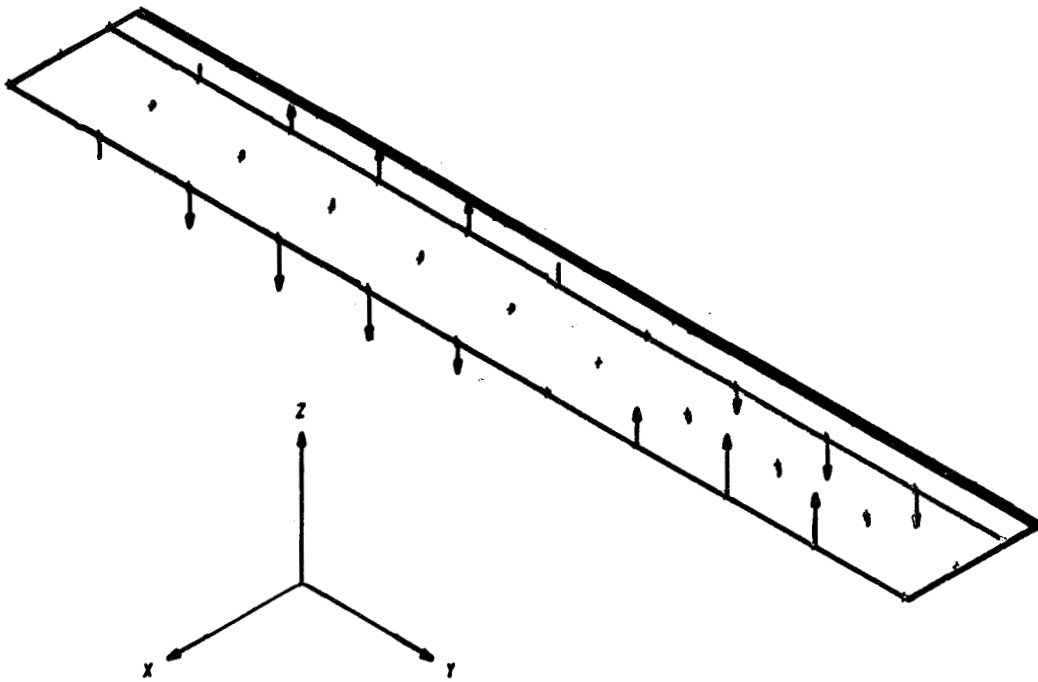
° SYMMETRICAL MODE ONE G - 13 FT.
DISCRETIZATION - 10 LONG BY 2 WIDE

MODE NUMBER 4
FREQUENCY 0.83168 Hz



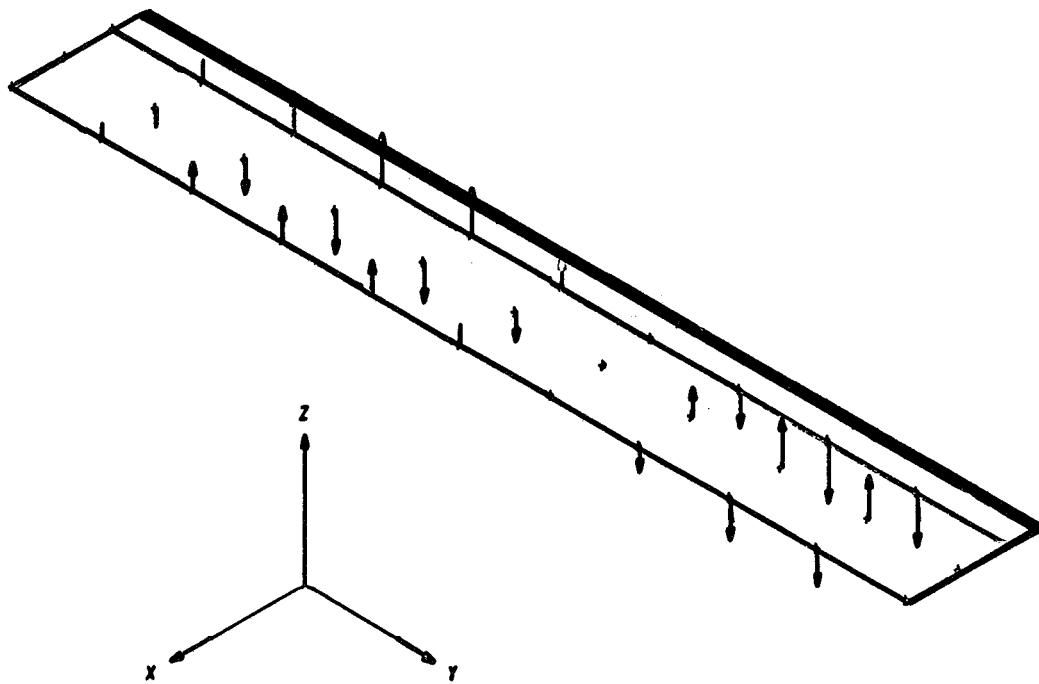
SYMMETRICAL MODE - ONE G - 13 FT.
DISCRETIZATION - 10 LONG BY 2 WIDE

MODE NUMBER 5
FREQUENCY 1.12638 Hz



· SYMMETRICAL MODE - ONE G - 13 FT.
DISCRETIZATION - 10 LONG BY 2 WIDE

MODE NUMBER 6
FREQUENCY 1.12651 Hz



APPENDIX F

ANTISYMMETRIC MODE SHAPES 13 FT LENGTH

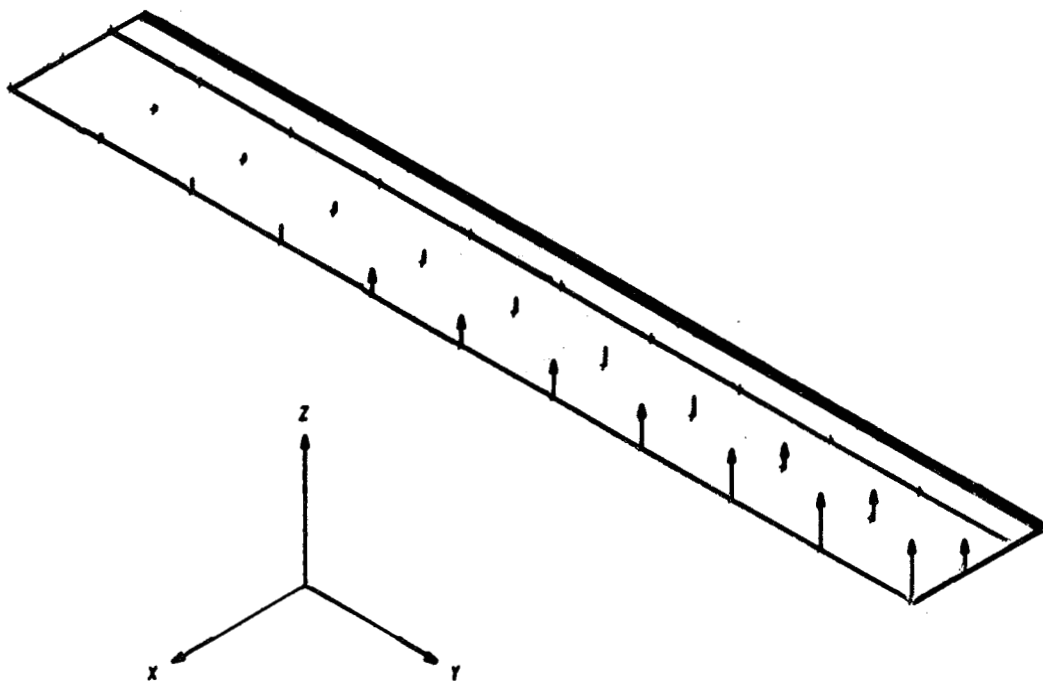
(NOTE: ONLY HALF OF SYSTEM SHOWN)

ANTISYMMETRIC MODE - ONE G - 13 FT.

DISCRETIZATION - 10 LONG BY 2 WIDE

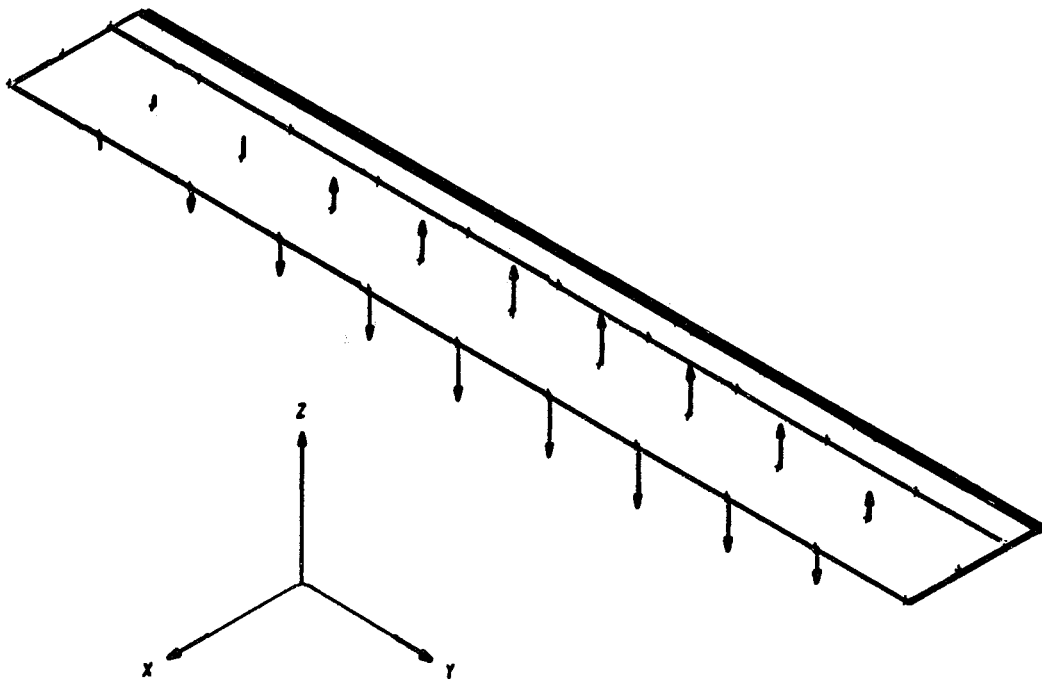
MODE NUMBER 1

FREQUENCY 0.29824 Hz



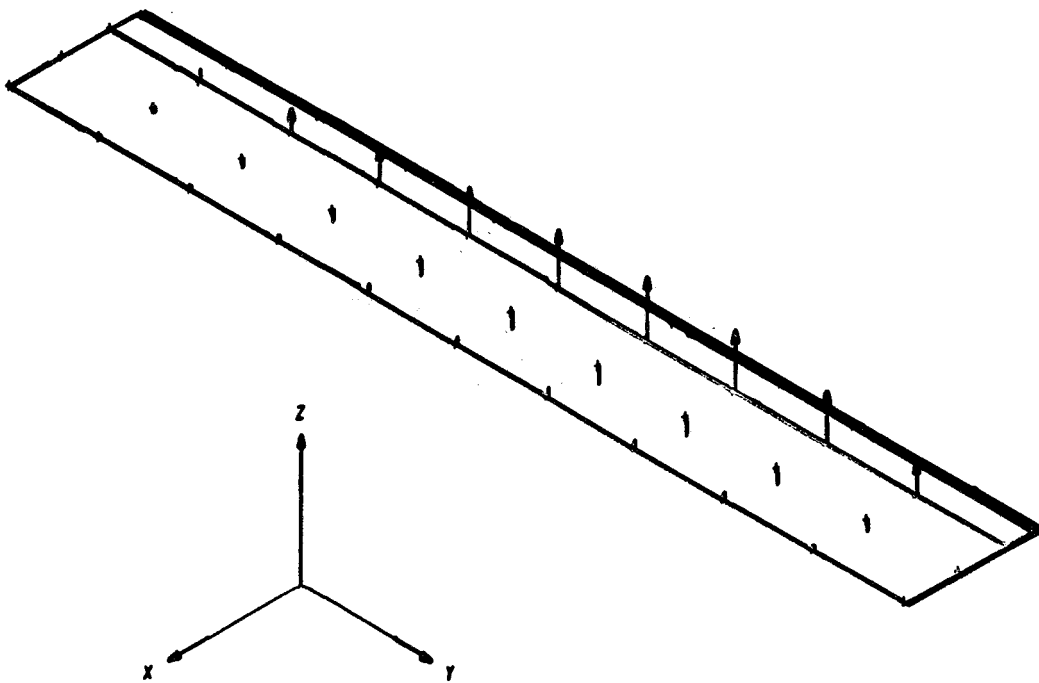
· ANTISYMMETRIC MODE - ONE G - 13 FT.
DISCRETIZATION - 10 LONG BY 2 WIDE

MODE NUMBER 2
FREQUENCY 0.55149 Hz



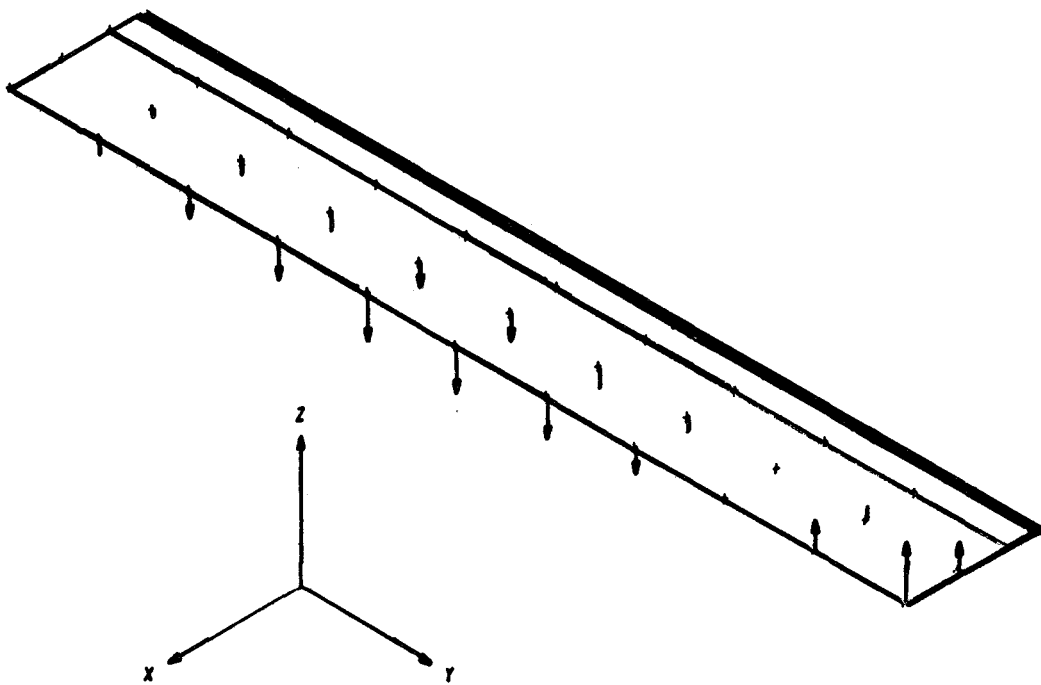
ANTISYMMETRIC MODE - ONE G - 13 FT.
DISCRETIZATION - 10 LONG BY 2 WIDE

MODE NUMBER 3
FREQUENCY 0.55141 Hz



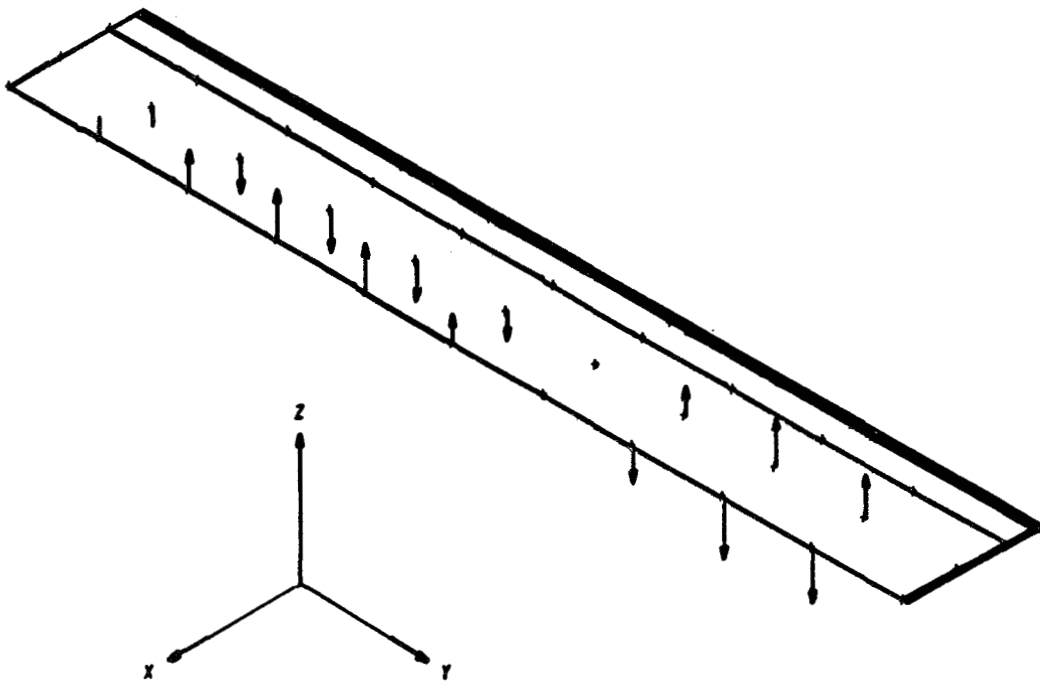
ANTISYMMETRIC MODE - ONE G - 13 FT.
DISCRETIZATION - 10 LONG BY 2 WIDE

MODE NUMBER 4
FREQUENCY 0.77527 Hz



ANTISYMMETRIC MODE - ONE G - 13 FT.
DISCRETIZATION - 10 LONG BY 2 WIDE

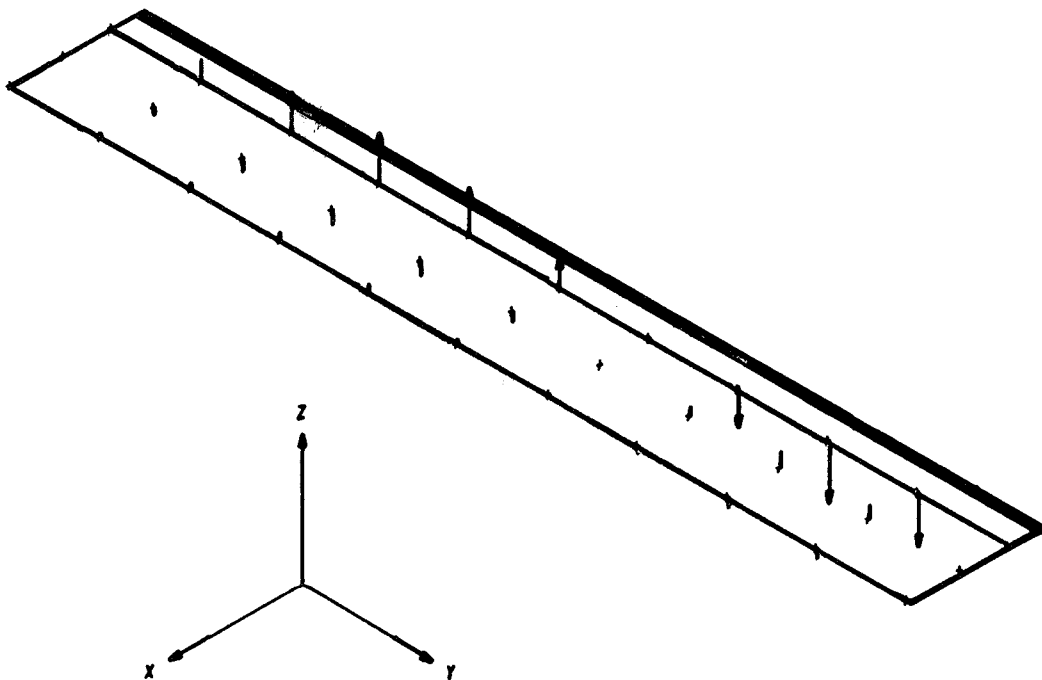
MODE NUMBER 5
FREQUENCY 1.12650 Hz



· ANTISYMMETRIC MODE - ONE G - 13 FT.
DISCRETIZATION - 10 LONG BY 2 WIDE

MODE NUMBER 6

FREQUENCY 1.12652 Hz



APPENDIX G

IN-PLANE MODE SHAPE PLOTS 13 AND 26 FT DEPLOYED LENGTHS

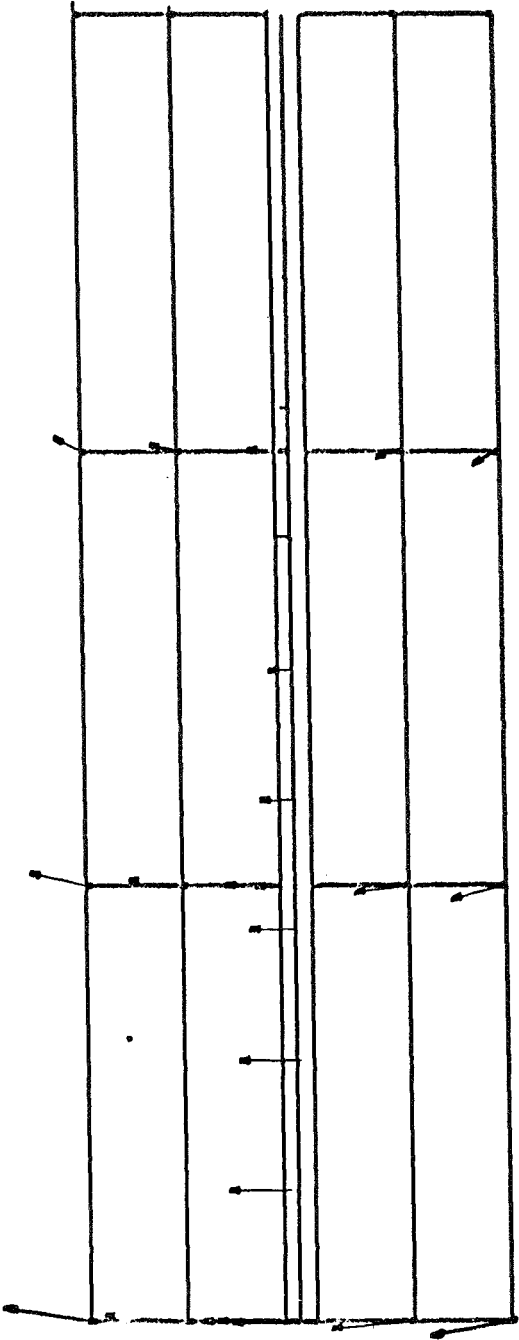
(NOTE: ONLY HALF OF SYSTEM SHOWN)

ROLL-UP SOLAR ARRAY, DEPLOYED 26 FT.

MODE NO. 1

IN-PLANE MODAL DEFLECTION PATTERN

NATURAL FREQUENCY (HERTZ) = 0.37844

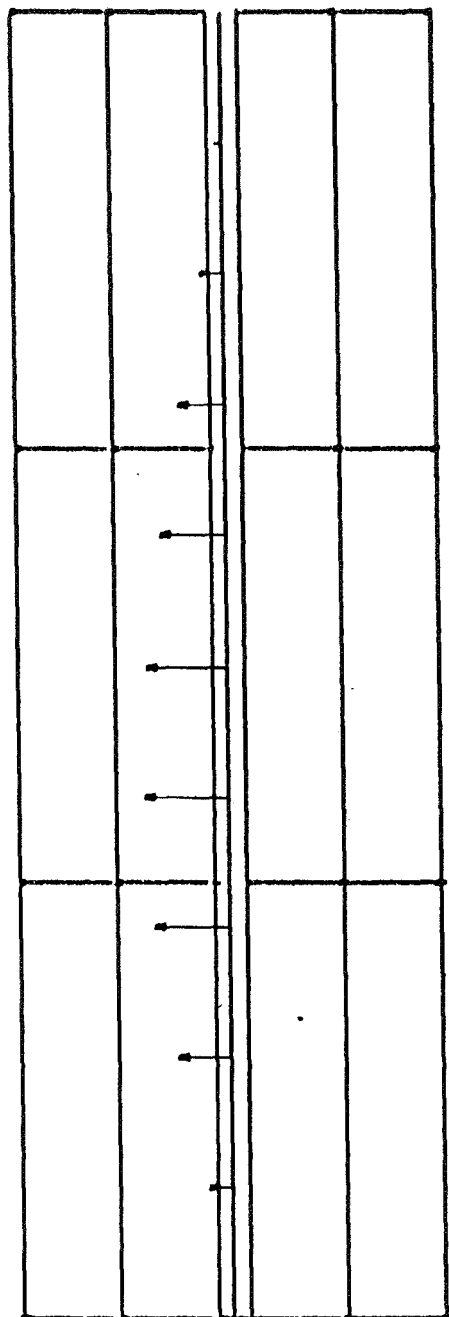


ROLL-UP SOLAR ARRAY, DEPLOYED 26 FT.

MODE NO. 2

IN-PLANE MODAL DEFLECTION PATTERN

NATURAL FREQUENCY (HERTZ) = 2.26335

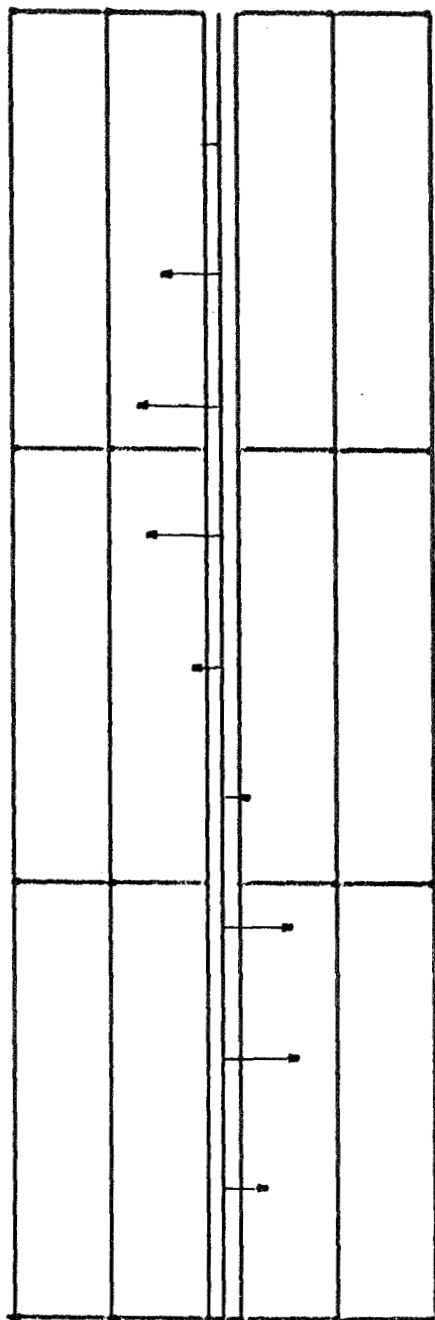


ROLL-UP SOLAR ARRAY, DEPLOYED 26 FT.

MODE NO. 3

IN-PLANE MODAL DEFLECTION PATTERN

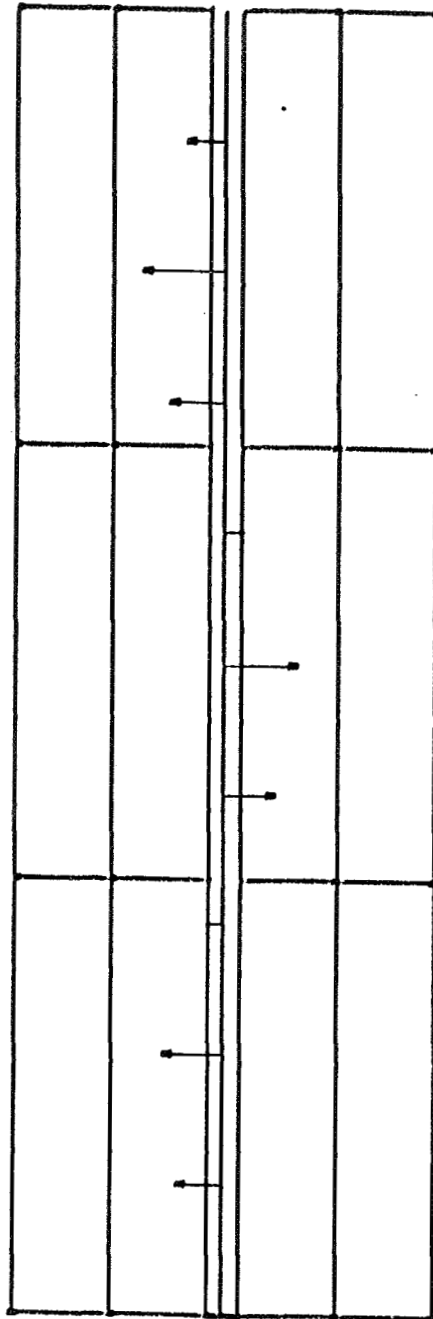
NATURAL FREQUENCY (HERTZ) = 7.32899



ROLL-UP SOLAR ARRAY, DEPLOYED 26 FT.

MODE NO. 4

IN-PLANE MODAL DEFLECTION PATTERN NATURAL FREQUENCY (HERTZ) = 15,4807

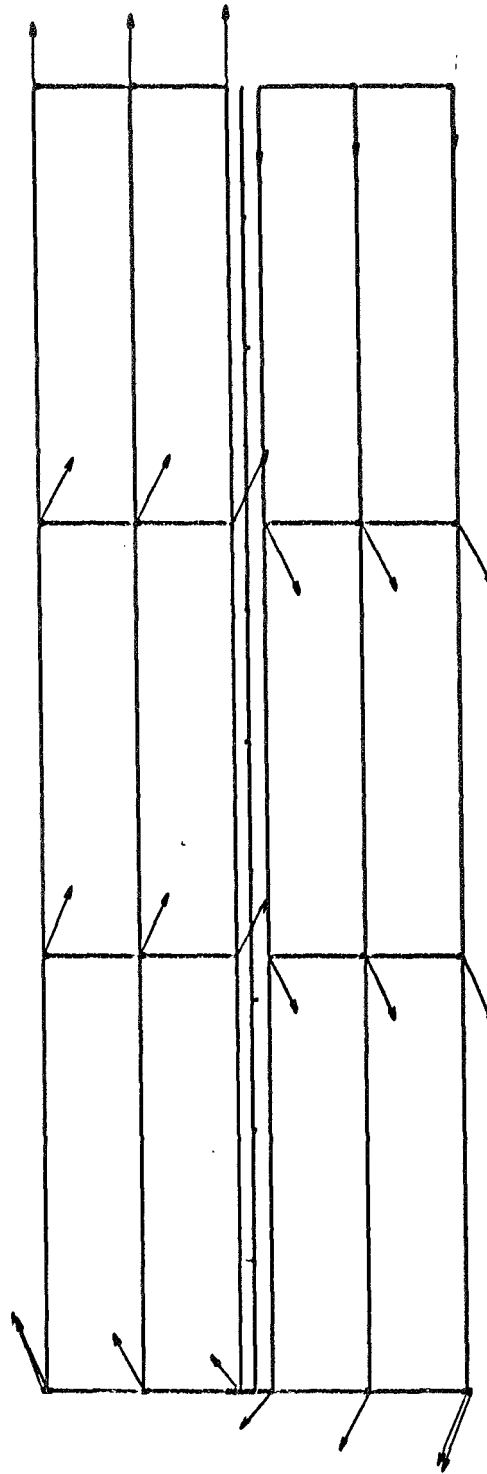


ROLL-UP SOLAR ARRAY, DEPLOYED 26 FT.

MODE NO. 5

IN-PLANE MODAL DEFLECTION PATTERN

NATURAL FREQUENCY (HERTZ) = 30.8678

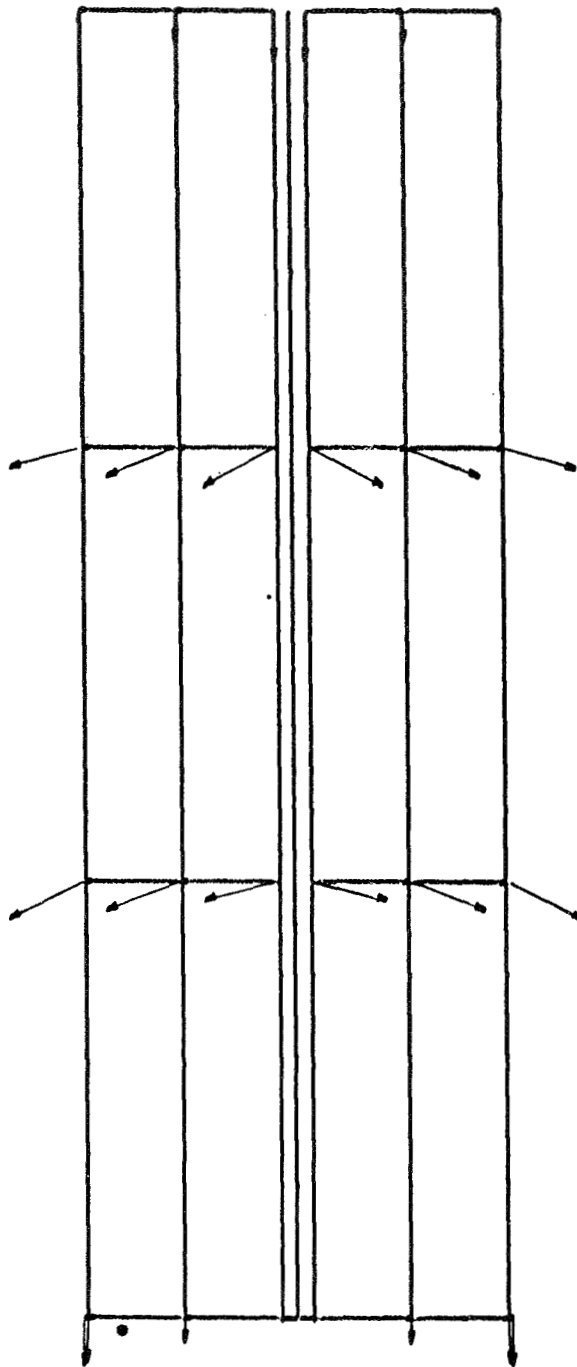


ROLL-UP SOLAR ARRAY, DEPLOYED 26 FT.

MODE NO. 6

IN-PLANE MODAL DEFLECTION PATTERN

NATURAL FREQUENCY (HERTZ) = 32.7268

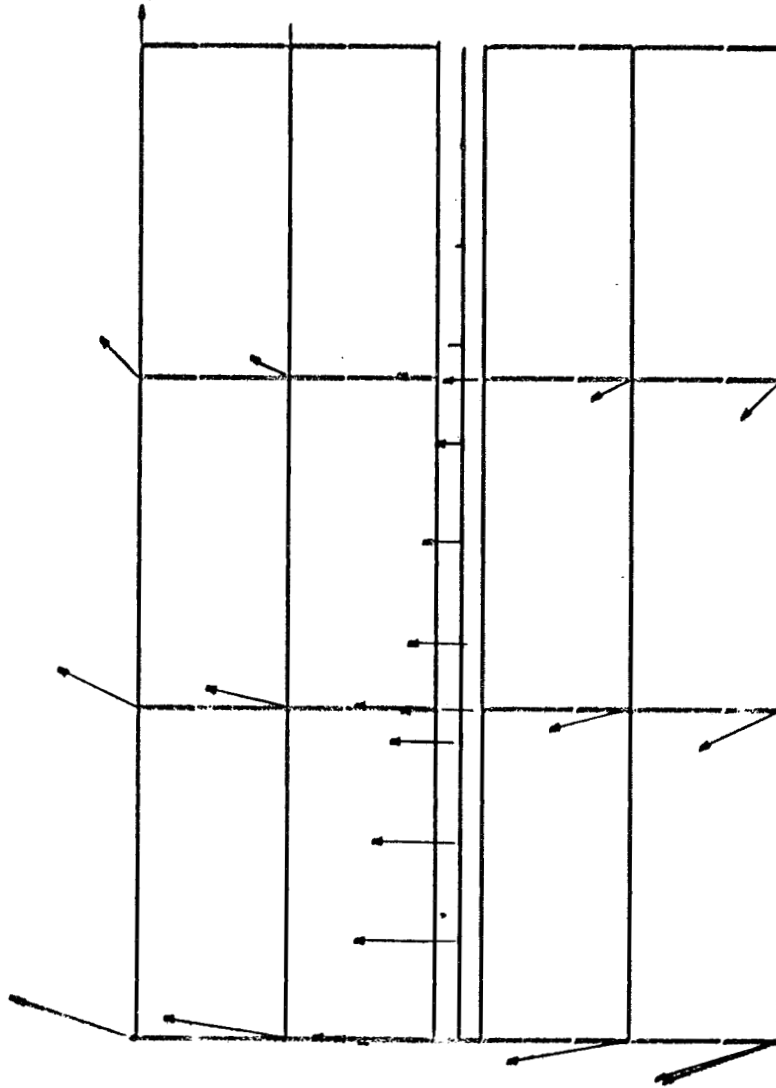


ROLL-UP SOLAR ARRAY, DEPLOYED 13 FT.

MODE NO. 1

IN-PLANE MODAL DEFLECTION PATTERN

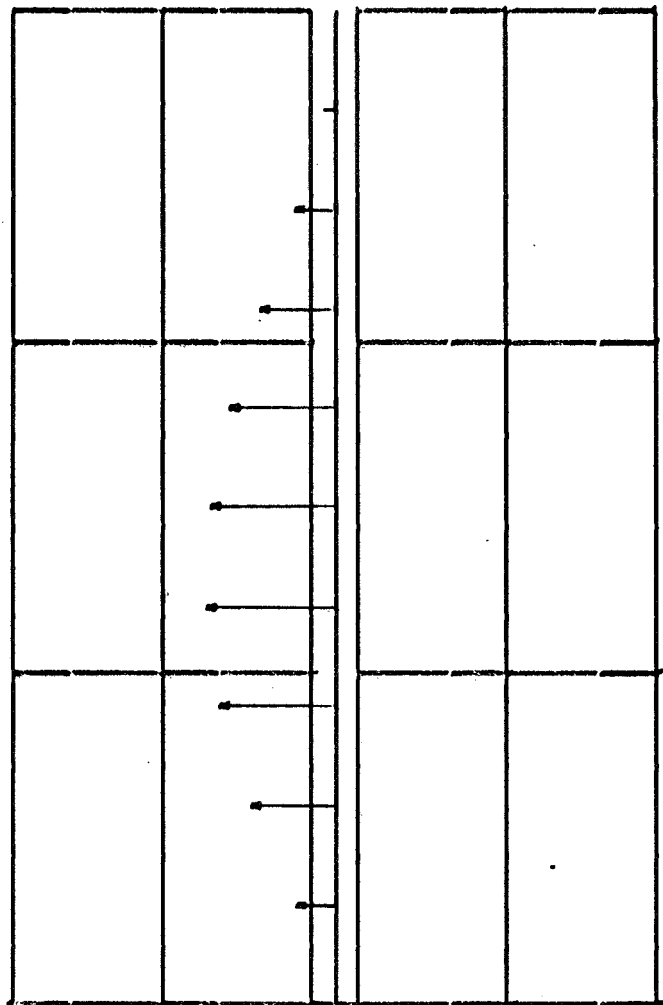
NATURAL FREQUENCY (HERTZ) = 0.81991



ROLL-UP SOLAR ARRAY, DEPLOYED 13 FT.

MODE NO. 2

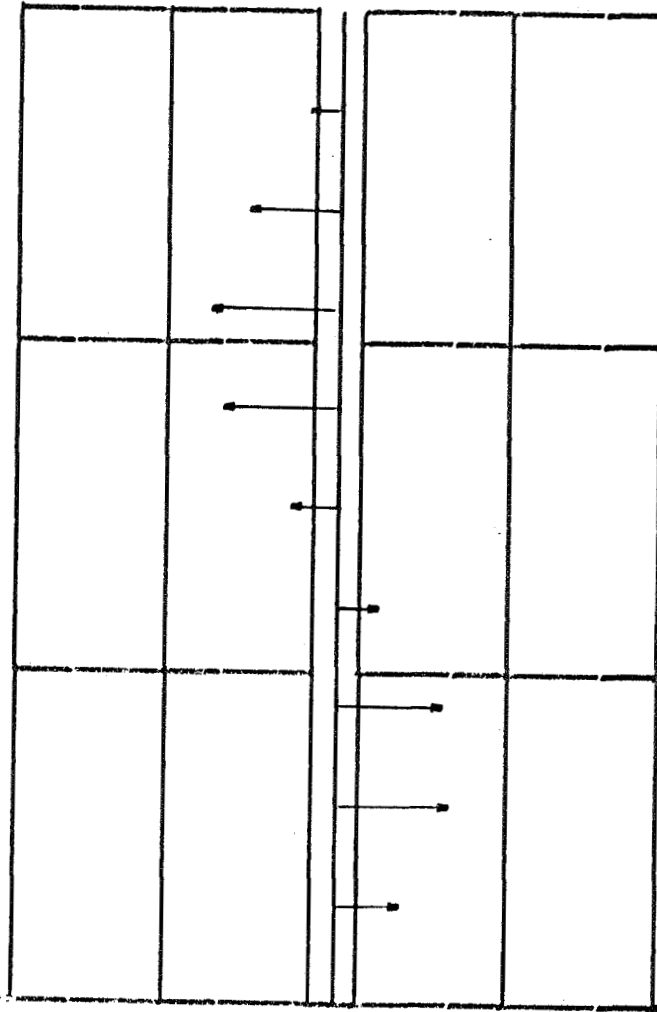
IN-PLANE MODAL DEFLECTION PATTERN NATURAL FREQUENCY (HERTZ) = 9.15350



ROLL-UP SOLAR ARRAY, DEPLOYED 13 FT.

MODE NO. 3

IN-PLANE MODAL DEFLECTION PATTERN NATURAL FREQUENCY (HERTZ) = 29.4519

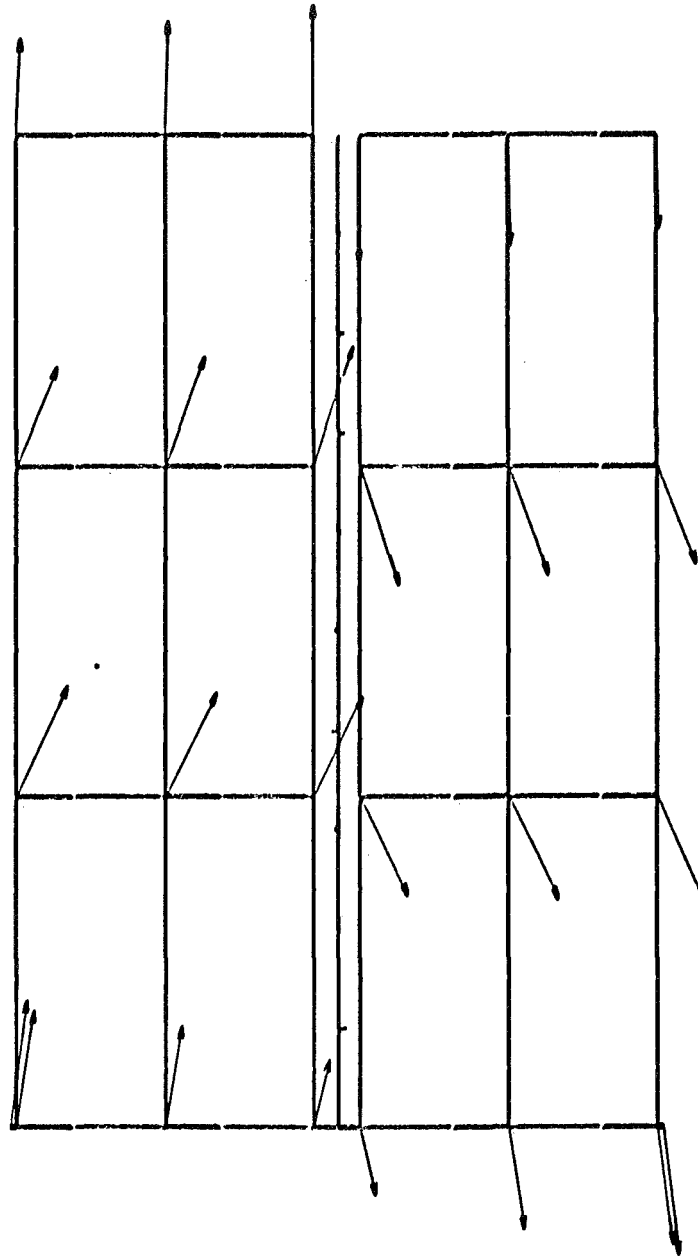


ROLL-UP SOLAR ARRAY, DEPLOYED 13 FT.

MODE NO. 4

IN-PLANE MODAL DEFLECTION PATTERN

NATURAL FREQUENCY (HERTZ) = 47.5327

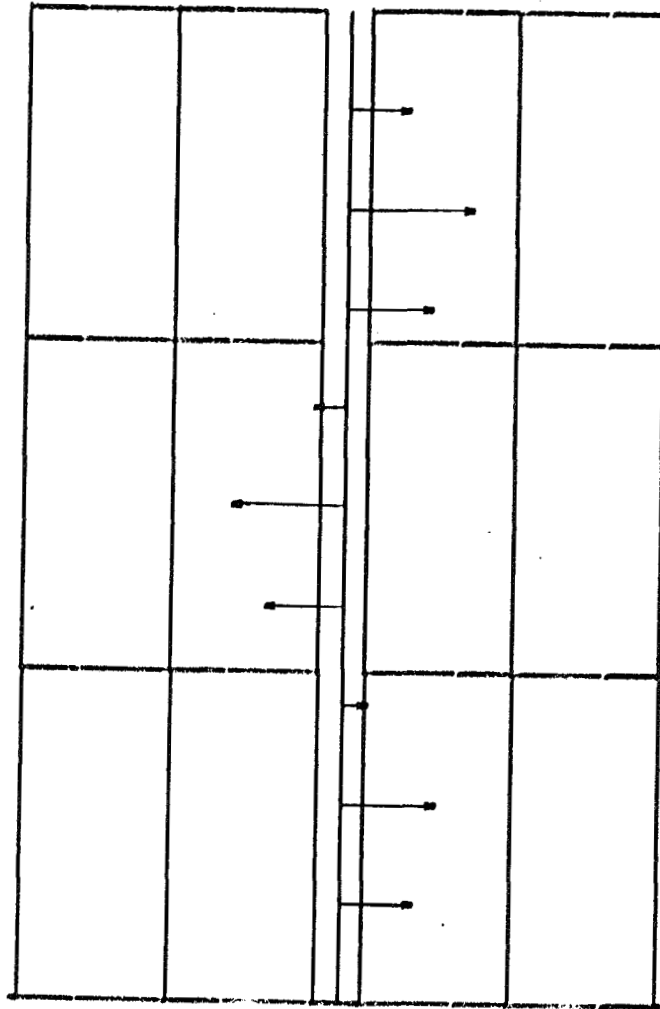


ROLL-UP SOLAR ARRAY, DEPLOYED 13 FT.

MODE NO. 5

IN-PLANE MODAL DEFLECTION PATTERN

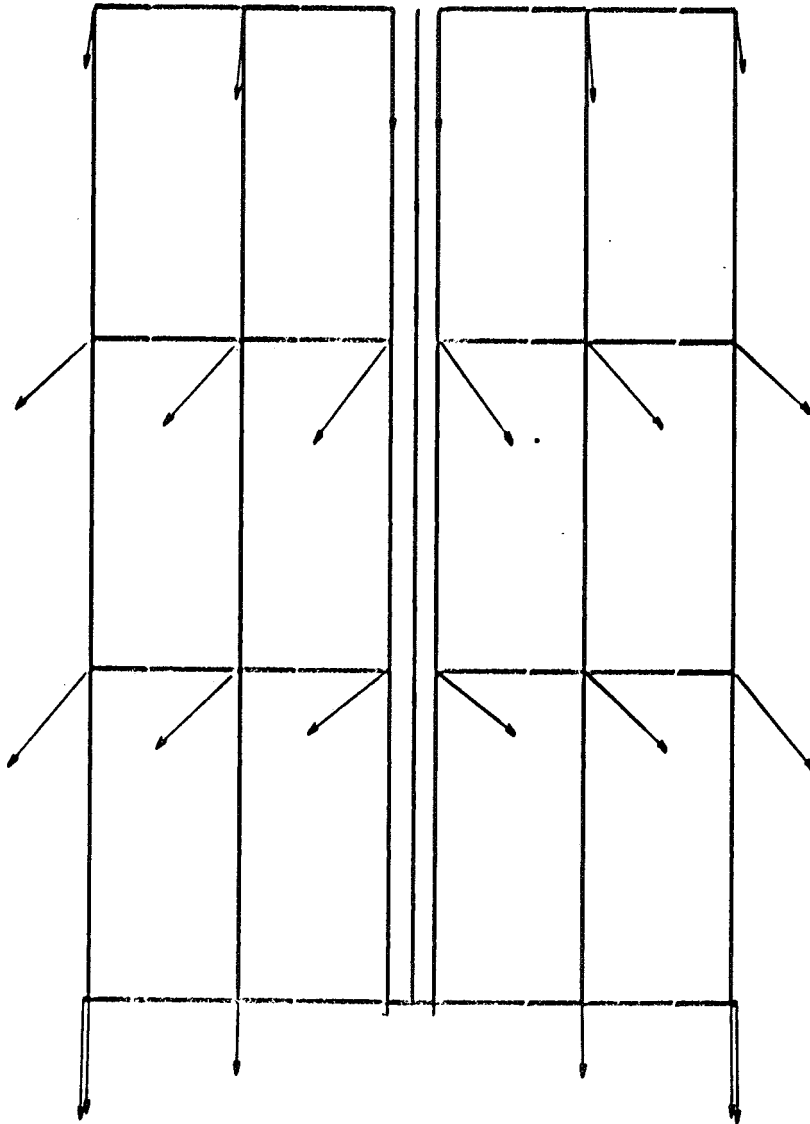
NATURAL FREQUENCY (HERTZ) = 62.0706



ROLL-UP SOLAR ARRAY, DEPLOYED 13 FT.

MODE NO. 6

IN-PLANE MODAL DEFLECTION PATTERN NATURAL FREQUENCY (HERTZ) = 68,1033



GENERAL  ELECTRIC
SPACE DIVISION
SPACE SYSTEMS ORGANIZATION